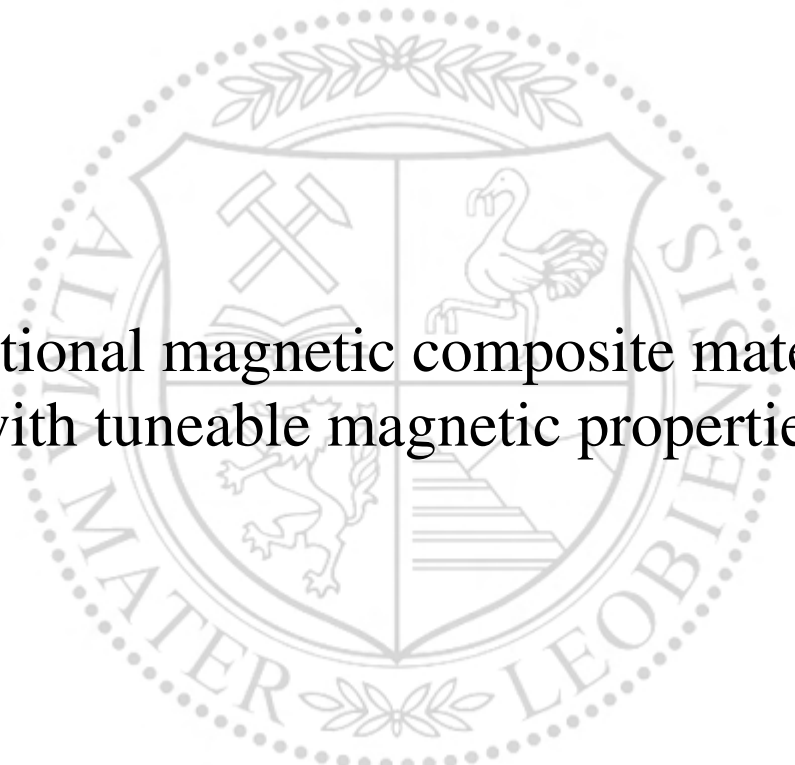Chair of Materials Physics

Master's Thesis

Functional magnetic composite materials with tuneable magnetic properties

Philipp Emanuel Payer, BSc

February 2024

AFFIDAVIT

I declare on oath that I wrote this thesis independently, did not use other than the specified sources and aids, and did not otherwise use any unauthorized aids.

I declare that I have read, understood, and complied with the guidelines of the senate of the Montanuniversität Leoben for "Good Scientific Practice".

Furthermore, I declare that the electronic and printed version of the submitted thesis are identical, both, formally and with regard to content.

Date 06.12.2023

_____

Signature Author
Philipp Emanuel Payer

Abstract

Sustainable electric propulsion systems require sophisticated combination of pole design and magnetic materials to provide the needed torque at a wide range of rotational speeds. One possible way to meet this challenge is the application of tailored magnetic materials. Magnetic composites often act as functional materials with properties tailored to their applications. With microstructural modification, properties like coercivity (H_c), remanence (B_r), saturation magnetization (M_s) and maximum energy product (BH_{max}) can be optimized.

In this thesis, the feasibility of magnetic composite fabrication by high-pressure torsion (HPT) is studied. Magnetic composites are fabricated using the multi-sector disk approach for bulk materials. In addition, the magnetic composites are fabricated by powder mixing and HPT. HPT-deformation experiments of single phase materials are conducted using Polymers (PTFE, PEEK, POM, PVC, PP) and commercial Y35-ferrite ceramics. To study the co-deformation of polymers, copper (Cu) –polymer composites are fabricated by a multi-sector disk approach. In a 2nd step, composites are fabricated using Sr-M-type hexaferrite phase as the hard magnetic component and iron (Fe), copper (Cu), chromium (Cr) and PTFE as a matrix. Furthermore, the effect of HPT deformation on commercial Y35-ferrites and the AlNiCo grades: AlNiCo 3, AlNiCo 5, and AlNiCo 8 are studied. Samples are examined by X-ray difraction (XRD), scanning electron microscopy (SEM), and light microscopy.

The magnetic properties of pristine magnets, deformed Y35-ferrites, powder composites, and deformed AlNiCo alloys are investigated. For magnetic measurements, a hystograph is used. To determine microstructural evolution, commercial Y35-ferrite is annealed at $300\,°C$, $500\,°C$, $700\,°C$, $900\,°C$ and $1100\,°C$, under atmospheric conditions and analyzed by XRD and light microscopy. HPT experiments reveal the deformability of bulk polymers to be limited. Properties of PTFE and POM are considered suitable for composite fabrication. Plastic incompatibility of bulk ferrite ceramic with metals and polymers leads to the fabrication of no structurally stable composites, using the multi-sector disc approach. Polymer-metal composites are successfully fabricated using the multi-sector disk approach. Application of post deformation annealing (PDA)

combined with pressing increases the adherence between layers in polymer-metal and polymer-ceramic composites. Moreover, powder composites are successfully fabricated with ceramic-metal and ceramic-polymer combinations. Despite a homogeneous distribution and sufficient refining no coupling between the magnetic phases is observed. The evolution of magnetic and structural properties shows a dependence on the powder combination used and is in good agreement with the literature. HPT of commercial Y35-ferrites leads to a grinding of sintered grains followed by a re-consolidation by pressing and interlocking of particles. These results are in good agreement with the literature. Annealing experiments show a sufficient stabilized microtructure. In addition, observed substitution effects of calcium (Ca) and aluminum (Al) lead to a shrinkage of the unit cell accompanied by an increase of H_c.

Kurzfassung

Nachhaltige elektrische Antriebssysteme erfordern eine ausgeklügelte Kombination aus Poldesign und magnetischen Werkstoffen, um das benötigte Drehmoment in einem breiten Drehzahlbereich bereitzustellen. Der Einsatz maßgeschneiderter magnetischer Werkstoffe bietet vielversprechende Möglichkeiten. Magnetische Verbundwerkstoffe fungieren oft als Funktionswerkstoffe mit Eigenschaften, die auf die jeweilige Anwendung zugeschnitten sind. Durch mikrostrukturelle Veränderungen können Parameter wie Koerzitivfeldstärke (H_c), Remanenzflussdichte (B_r), Sättigungsmagnetisierung (M_s) und das maximale Energieprodukt (BH_{max}) optimiert werden.

In dieser Arbeit wird die Herstellbarkeit von magnetischen Verbundwerkstoffen durch Hochdrucktorsion (HPT) untersucht. Die magnetischen Verbundwerkstoffe werden mit Hilfe der segmentierten Proben Methode (Tortenstücktechnik) für Bulk-Materialien, sowie mittels Pulvermischen gefolgt von HPT hergestellt. Erste HPT-Experimente mit einphasigen Materialien werden mit Polymeren (PTFE, PEEK, POM, PVC, PP) und handelsüblichen Y35-Ferritkeramiken durchgeführt. Zur Untersuchung der Co-Verformung von Polymeren werden Kupfer (Cu)-Polymer-Verbundwerkstoffe mit Hilfe der segmentierten Proben Methode hergestellt. In einem zweiten Schritt werden Verbundwerkstoffe mit einer Sr-M-Typ Hexaferritphase als hartmagnetische Komponente und Eisen (Fe), Kupfer (Cu), Chrom (Cr) und PTFE als Matrix hergestellt. Darüber hinaus werden die Auswirkungen der HPT-Verformung auf handelsübliche Y35-Ferrite und die AlNiCo-Legierungen: AlNiCo 3, AlNiCo 5, und AlNiCo 8 untersucht. Mikrostrukturanalysen werden mittels Röntgenbeugung, Rasterelektronenmikroskopie und Lichtmikroskopie durchgeführt.

Die magnetischen Eigenschaften von unbehandelten Magneten, verformten Y35-Ferriten, Pulververbundwerkstoffen und verformten AlNiCo-Legierungen werden untersucht. Für magnetische Messungen wird ein Hystograph verwendet. Zur Bestimmung der mikrostrukturellen Entwicklung werden handelsübliche Y35-Ferrit Proben bei 300 °C, 500 °C, 700 °C, 900 °C und 1100 °C unter atmosphärischen Bedingungen geglüht und mittels Röntgenbeugung und Lichtmikroskopie analysiert. HPT-Experimente zeigen eine begrenzte Verformbarkeit von Polymeren. Die Eigenschaften von PTFE

und POM sind geeignet für die Herstellung von Verbundwerkstoffen mittels HPT. Die unterschiedlichen mechanischen Eigenschaften von Ferritkeramik, Metallen und Polymeren behindern eine erfolgreiche Herstellung mittels segmentierter Proben Methode. Polymer-Metall-Verbundwerkstoffe werden erfolgreich mit dieser Methode hergestellt. Die Anwendung von Wärmebehandlung nach der Verformung (PDA) in Kombination mit Pressen erhöht die Haftung zwischen den Schichten in Polymer-Metall- sowie Polymer-Keramik-Verbundwerkstoffen. Des Weiteren werden Pulververbundwerkstoffe mit Keramik-Metall und Polymer-Keramik Materialkombinationen erfolgreich hergestellt. Trotz einer homogenen Verteilung und auftretender Kornfeinung wird keine Kopplung zwischen den magnetischen Phasen beobachtet. Magnetische und strukturelle Eigenschaften zeigen eine Abhängigkeit von der verwendeten Pulverkombination und steht in guter Übereinstimmung mit der Literatur. HPT von handelsüblichen Y35-Ferriten führt zum Brechen von Körnern, gefolgt von erneuter Kompaktierung durch Pressen und Verhaken von Partikeln. Diese Ergebnisse stehen in guter Übereinstimmung mit der Literatur. Glühversuche zeigen ein ausreichend stabilisiertes Gefüge. Zusätzlich beobachtete Substitutionseffekte von Kalzium (Ca) und Aluminium (Al) führen zu einer Schrumpfung der Einheitszelle, begleitet von einem Anstieg von H_c.

Acknowledgment

Contents

List of Figures

List of Tables

Source code

List of material cards

1. Introduction

Magnetic materials are a fundamental basis of our modern lifestyle. Computer, electric-mobility, and medical treatments are only a short list of applications of magnets [1, 2]. With a fast-evolving technology, an rising awareness about limited resources like rare-earth metals and energy efficiency, new challenges are present in this field of research. In this work, the fabrication of tuneable magnetic composites by severe plastic deformation (SPD) is examined. Hereby, the focus lies on hard magnetic materials typically used for electric motors.

Propulsion systems for electrical-mobility should be able to provide a high torque at low rotational speed and maintain an efficient operating state throughout a wide speed range. However, depending on the magnets used, the maximum speed is limited. For the high starting torque, a high coercivity (H_c) is necessary. On the other hand, the same magnets required for the high torque lead to increasing losses at high rotational speed, due to the high resistance against remagnetization [3, 4]. Therefore, modern motors exhibit a special flux design, which allows to vary the magnetic flux density with respect to the rotational speed. Such motor constructions allow the minimization of losses caused by the remagnetization and eddy currents. This motor design combines different magnetic materials and shapes to create a rotor with an optimized net flux. To further optimize this approach required magnets have to be tailored themselves according to the needs of the motor design [5, 6]. The approach studied in this thesis is the fabrication of such tuneable magnets as hard magnetic composites by SPD. The chosen method is high-pressure torsion (HPT). Through the fabrication via HPT, a refinement of the used materials occurs. The aspired structure of the samples is a fine layered sheet system. As different material combinations can display various forms of interactions, five material combinations are studied. As a magnetic material, Y35 strontium hexaferrite is used and combined with a polymer, a ferromagnetic metal, iron (Fe), a diamagnetic metal, copper (Cu) as well as an antiferromagnetic metal, chromium (Cr). In a first step, the pristine materials, such as Polytetrafluorethylene (PTFE), Polyoxymethylene (POM), Polyetheretherketone (PEEK), Polyvinylchloride (PVC), Polypropylene (PP), Y35-ferrite, and the AlNiCo grades AlNiCo 3, AlNiCo 5

as well as AlNiCo 8 are processed by HPT. The microstructural changes are analyzed by X-ray difraction (XRD), light microscopy (LIMI) and scanning electron microscopy (SEM). Furthermore, magnetic characterization is performed for the deformed Y35 ferrite and the AlNiCo alloys.

Composites are fabricated via the multi-sector disk approach for HPT [7], using polymers, metals, and magnetic materials. After initial microscopy analysis, the HPT process is optimized. First, the polymers are combined with Cu. In a second step, the metal is replaced by the Y35-ferrite and optimized once again. To compare the influence of different starting materials, the same composites are produced as powder composites. Magnetic measurement in the axial direction, XRD as well as microscopy are conducted on the powder composites. Additionally, an annealing series of Y35-ferrites at 300 °C, 500 °C, 700 °C, 900 °C and 1100 °C at air is performed. To analyze microstructural and chemical changes, an XRD and microscopy analysis are carried out.

2. Theory

2.1. Theory of Magnetism

Magnetic properties of matter originate in the movement of electrons in their orbitals. Considering the reaction of materials to an external magnetic field (H), one can determine five different types of magnetism. Some materials like Cu, gold (Au), bismuth (Bi) or graphite do not show any spontaneous magnetization, but if an external magnetic field is applied, a repulsive force is detected. These types of materials are diamagnetic (DM). This behavior results from an electron configuration where the orbitals are fully filled, or net spins are compensated by another atom in case of molecules. The repulsion originates from the interaction of the field with the movement of electrons. This mechanism is based on quantum mechanical effects and is present in all types of materials. A schematic illustration of diamagnetism is shown in figure 2.1 (a). Materials showing no magnetization without an external field, but feature a magnetic moment when a magnetic field is applied, are called paramagnetic (PM). Despite having no net magnetic moment, single atoms of these materials show a net magnetic moment due to unpaired electrons. At $H = 0$ field, randomly oriented spins are present, as shown in figure 2.1 (b). When a H-field is applied, the spins align with rising H gradually, until a H-field is reached where all spins point in the same direction of H. An example of a paramagnetic material is aluminum (Al). This alignment rivals thermal disordering and therefore is temperature-dependent. In some materials, spins are able to interact via spin-coupling mechanisms, leading to a defined magnetic order at $H = 0$ field. There are three different types of magnetic ordering, as can be seen in figure 2.1 (c, d and e). In the case of ferromagnetism (FM), figure 2.1 (c) all spins are aligned, showing a net magnetization at $H = 0$ field as well as an amplification of an applied H-field. The alignment in FM materials is accomplished by quantum mechanical interactions and interloking of the spins. The same behavior, but with a weaker net magnetization at $H = 0$ field holds for ferrimagnetic (FiM), figure 2.1 (d) material. Such materials inherent a spin ordering in alternating directions, with the spin in one direction being less pronounced within the material, leaving the observed

net magnetization. Materials like Fe or cobalt (Co) are examples of FM materials while ceramics or minerals like $SrFe_{12}O_{19}$ and Fe_3O_4 are examples of FiM materials. In the latter substances, coupling of the electrons belonging to different ions results in different FiM ordering. If a material shows alternating spin order with equal spins, figure 2.1 (e) they belong to the group of anti-ferromagnetic (AFM) materials. Materials like chromium or manganese oxide do not show any magnetic moment at $H = 0$ field, but behave in a far more complex way under applied magnetic fields [2, 8, 9].
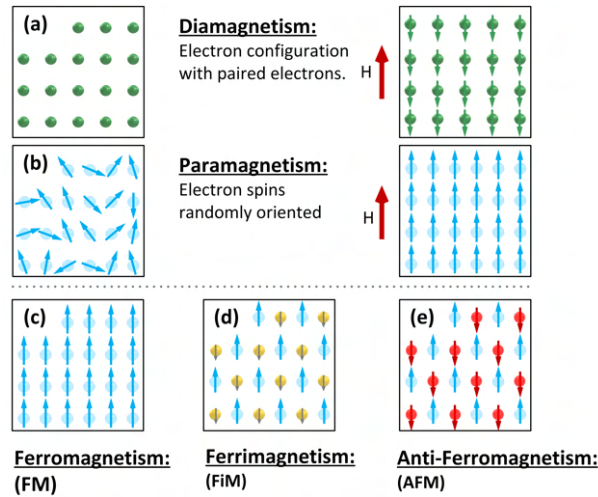
Figure 2.1.: Schematic illustration of magnetic behavior in matter.

2.1.1. Microstructure of Magnetic Materials

Magnetic materials are divided into soft magnetic and hard magnetic materials depending on their magnetization behavior. In figure 2.2, the typical shape of magnetization curves for soft- and hard magnetic materials are shown. Whilst hard magnetic materials exhibit a broad magnetization curve, resulting from a large coercive force. Materials displaying an low intrinsic coercivity (H_{cJ}) of $H_{cJ} \leq 100 \, \text{kA/m}$ are called soft magnetic [10].
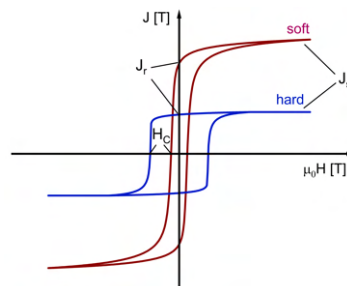
Figure 2.2.: Magnetization curves for soft and hard magnetic materials, showing characteristic parameters as remanence (H_r), saturation polarization (J_s) and coercivity (H_c). Adapted from Weissitsch et al. [11] and Goll et al. [12].

2.1.2. Characterization of Magnets

The measurement of complete hysteresis loops is one of the most used characterization methods for magnetic materials. Besides high-resolution methods like the superconducting quantum interference device (SQUID) or vibrating sample magnetometer (VSM), DC hystograph measurements are a suitable and fast solution for the characterization of permanent magnets. A measurement set-up with the Brockhaus HG200 hystograph is depicted in figure 2.3 [2].

Figure 2.3.: Hystograph Brockhaus HG200 used at the Erich Schmid Institute in Leoben.

In this measurement, the sample is placed between two moveable poles in a closed circuit. The H-field and the magnetic polarization (J) are measured with an integrating flux meter via a J-compensated surrounding coil, using induction. The principal function of the surrounding coils is shown in figure 2.4. For simplicity, the J-compensation is not illustrated in this schematic. J-compensated surrounding coils represent a special sort of sense coils in which $\mu_0 H$ is subtracted from the magnetic flux density (B) coil electrical, creating a direct signal for J. The signals of J and H are then processed in an integrating flux meter. Further mathematical calculations and the determination of magnetic parameters are made within the associated software package [2, 13].
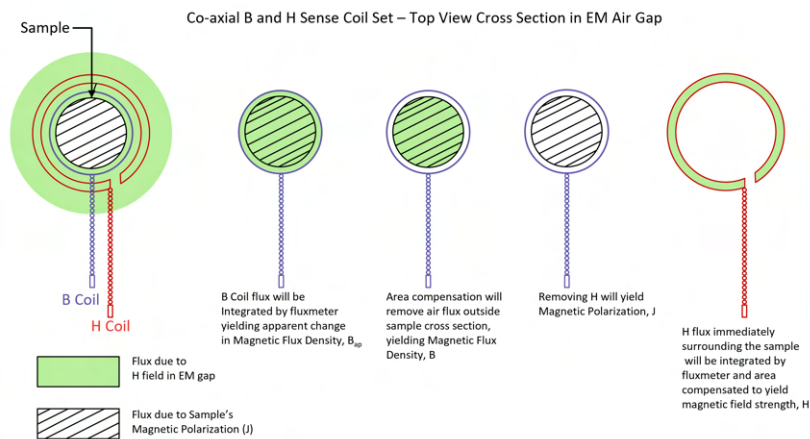
Figure 2.4.: Coaxial surrounding coils inserted in the air gap of the electromagnet redrawn from [13].

One big benefit of this method is the short time needed for the measurements. On the other hand, there are some drawbacks to consider. During long measurements the flux meter drifts, causing an error which is corrected in the software package, but limits the maximum reasonable measuring time and thus the resolution. Also, the field at the contact points is not homogeneous, leading to a small deviation from the behavior of an ideal closed circuit [13]. Besides these limitations, there is also a known magnetic image effect, leading to an apparent decrease in magnetization after saturation. This effect arises out of localized saturation of the poles coupled with a sample geometry dependence of the H field. Especially small L/D ratios (where D is the diameter and L is the length of the sample) combined with high saturation magnetization are prone to show this effect. For samples with $L/D \geq 1.8$ no image-effect occurs. While this effect leads to distorted magnetization curves in the 1st and 3rd quadrant, the 2nd quadrant is not affected. For a sufficient measurement of full hysteresis loops, the electrical current must be set high enough to reach the J_s [2, 14–16].

For hard magnetic materials, especially the properties measured in the 2nd quadrant are important. Besides remanence (B_r), H_{cJ} and coercivity (H_{cB}), maximum energy product (BH_{max}) is an important property. It describes the energy which can be stored by the magnet. Therefore, the BH_{max} is an important parameter in the layout of electric motors and generators. In figure 2.5, the most important parameters, which can be measured by a hystograph are shown.
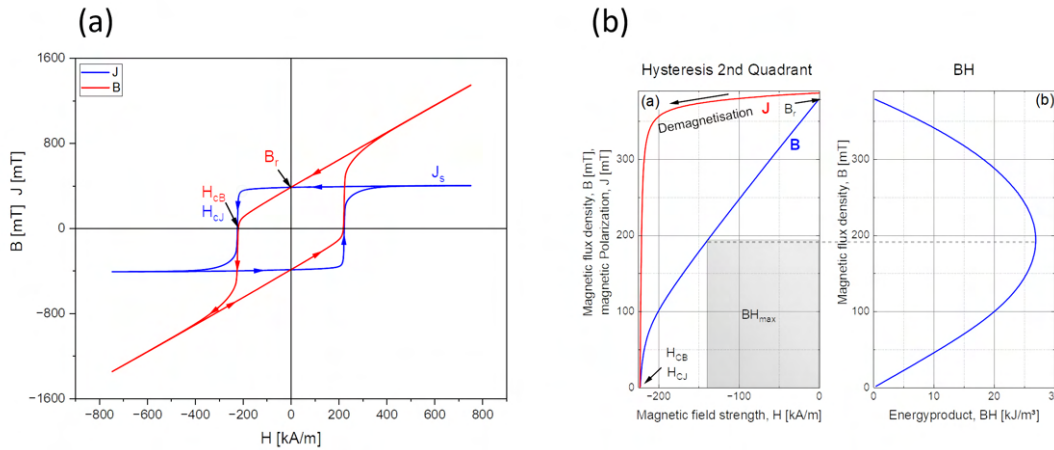
Figure 2.5.: Schematic illustration of a magnetization curve (a) . The magnetic parameters intrinsic coercivity (H_{cJ}), coercivity (H_{cB}), remanence (B_r) and saturation polarization (J_s) are shown at the corresponding pints of the magnetization curve. Also the 2nd quadrant of the magnetization curve, showing the energy product BH_{max} (b).

2.1.3. Hard Magnetic Materials

As described before, BH_{max} and the squareness of a magnetization curve can be used to describe the magnetic hardness of a material. By far more important for hard magnetic materials is the consideration of the magneto crystalline anisotropy, described by the 1st anisotropy constant K_1. This relation can be used to formulate a magnetic hardness parameter κ. Magnets with a $\kappa > 1$ are considered hard permanent magnets, while magnets like AlNiCo with $\kappa < 1$ are considered semi-hard [17, 18].

$$\kappa = \sqrt{\frac{K_1}{\mu_0 M_s^2}} \tag{2.1}$$

2.1.4. Magnetic Composites

As can be seen from modern magnetic materials such as NdFeB or AlNiCo magnets, which inherently consist of two different phases, the structuring of magnetic materials in multiphase materials can lead to outstanding magnetic properties. The tuning trough structuring of the magnetic microstructure is a complex process not only depending on the magnetic properties of the single phases but also on the shape, size, and orientation of single phase regions. The influence of coupling phases with different magnetic behaviors like AFM and FM on the magnetization curve of the resulting composite is described by Weissitsch et al. in [11]. Figure 2.6 shows the influence of phase combinations on the magnetization curves. In NdFeB magnets often the type

I microstructure is implemented. Every grain represents a small permanent magnet, decoupled from other grains by a thin layer of DM material. As a result the type I microstructure shows a high H_c. Reducing the grain size towards the size of single domain particles increase this effect even further. If only a single hardmagnetic phase is present, the grains show exchange interactions leading to an increase in B_r. Such a single phase microstructure is represented by a type II microstructure. For composites of hard and soft magnetic materials with a sufficient small grain or particle size, exchange coupling is possible. An exchange coupled hard-soft magnetic microstructure is discribed by type III. Stabilization of the magnetization of the soft magnetic phase by the coupling with the hard magnetic phase, leads to an increase in B_r. By mixing of a AFM material with a FM material it is possible to achieve a type IV microstructure, where the spins of the AFM and FM material are locked in the same direction at the interface resulting in an exchange bias [11, 12, 19].
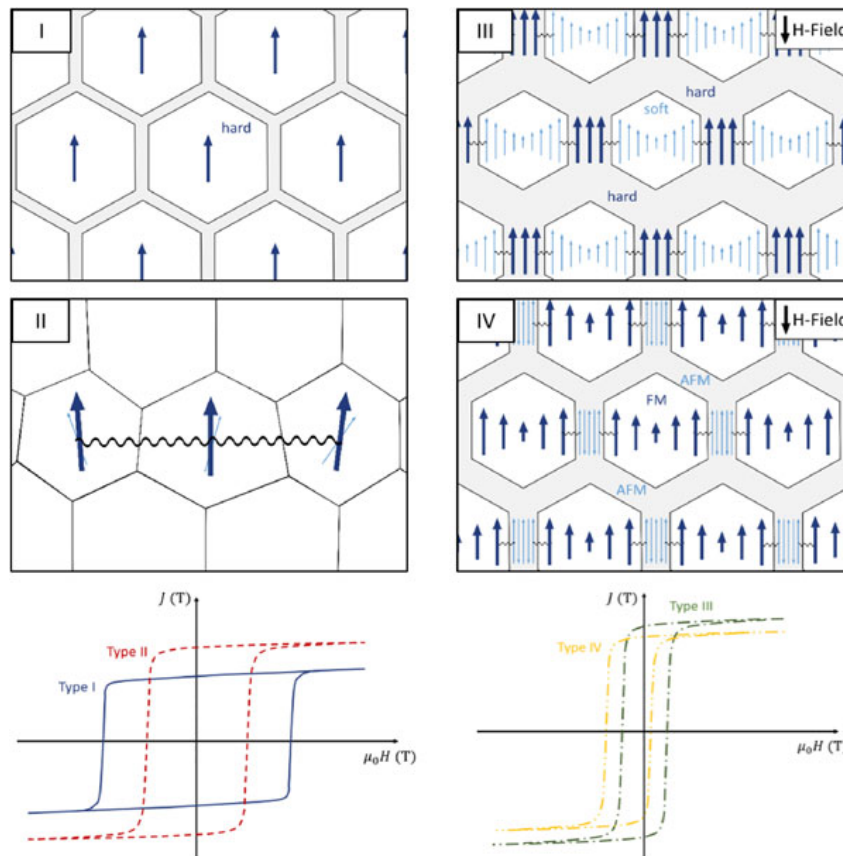
Figure 2.6.: Coupling mechanisms and magnetization curves of soft and hard magnetic composite materials. Type I: hard magnetic phase decoupled by a DM material at the grain boundaries, like in NdFeB–magnets. Type II: exchange interaction between domains in multiple grains within a single phase FM material. Type III: exchange coupling between a soft magnetic and a hard magnetic phase. Type IV: coupling of an AFM and a FM material leading to exchange coupling. Reprinted from Weissitsch et al. [11].

According to Skomski [17] aligned layered structures of hard- and soft-magnetic materials can result in an improved BH_{max} up to $1000\,\mathrm{kJ/m^3}$, by the combination of the

high magnetization of soft-magnetic materials with the high H_c of the hard magnetic material. The thickness of the soft-magnetic material is crucial for sufficient coupling, and should not be larger than twice the Bloch wall width δ_h of the hard magnetic phase [17].

2.2. Materials

2.2.1. Deformation Mechanisms in Materials

The deformation mechanisms of metals are well understood and described in numerous scientific papers and textbooks [20–32]. For ceramics and polymers, deformation is a far more complex process. A comparison of deformation maps can help for a better understanding of deformation mechanisms present in metals and ceramics at certain parameters. In figure 2.7 deformation maps of nickel (Ni) (a) and Fe (b) are depicted. Clearly visible is the region between the ideal stress and the tensile stress. In this region, dislocations can move, if the activation stress is reached and more than five glide systems are active. At lower stress, several creep mechanisms can be thermally activated [20, 21].
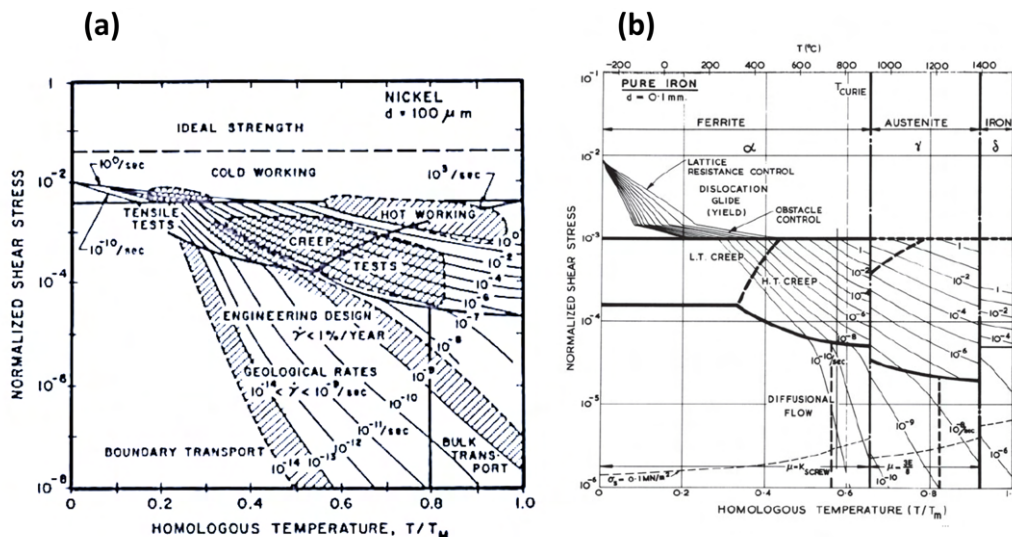
Figure 2.7.: Deformation map of pure nickel according to Notis et al. [20] (a) and pure iron according to Frost et al. [21].

Compared to the deformation map of an oxide ceramic, like NiO in figure 2.8, it can be seen that dislocation activity is far more restricted in this curve and at a homologous temperature of 0 no dislocation activity is possible. It is also worth noting

that the velocity of dislocations in ceramics is by orders of magnitude slower. At elevated temperature like in metals, diffusion and creep comes into play. In metals, the velocity of diffusion-controlled processes is set by the mean free path, the amount of impurities, and lattice defects. For ceramics, diffusion is more complex, due to the ionic bond character. In ceramics, depending on the specific diffusing substance, diffusion can be anion or cation-controlled [20]. Dislocation activities in ceramics have been reported around crack tips and at elevated temperatures in the form of twining or slipping [33, 34]. According to Langdon et al. [35], the sliding of grain boundaries plays an important role in the deformation of ceramics, especially at elevated temperatures. Hodge et al. [36] describes the deformation processes in Sr and Ba ferrite materials. At temperatures around 1200 °C, also strain hardening effects are observed.
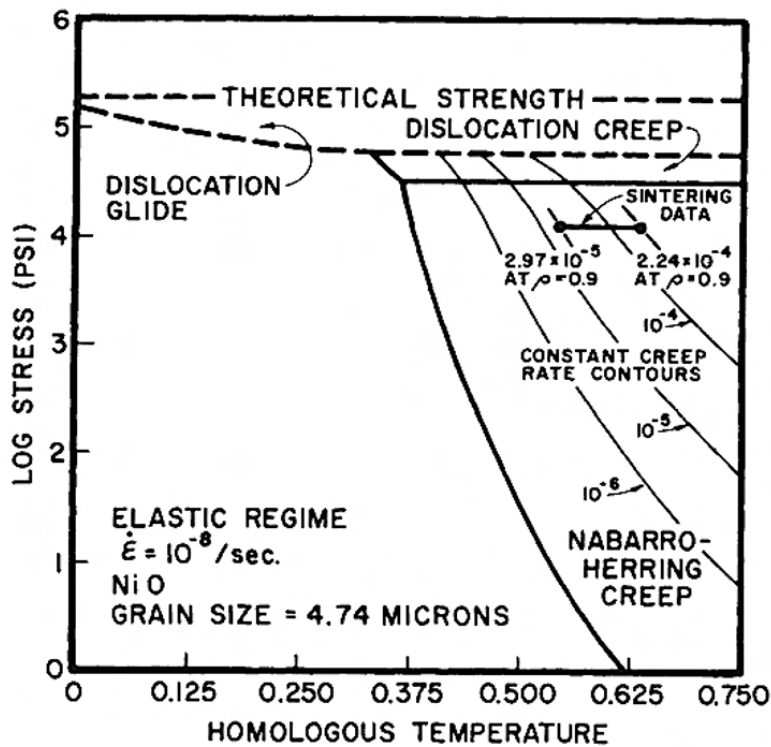
Figure 2.8.: Deformation map for NiO [20].

Polymers show a viscoelastic and viscoplastic behavior. Therefore, deformation is stress and time-dependent. The molecular model, as depicted in figure 2.9, describes the stages of deformation in semi-crystalline polymers. At first, the deformation is restricted to amorphous regions since the close arrangement of chains in the crystalline regions leads to additional binding forces and a higher youngs-modulus. In the second stage also the crystalline regions are elastically stretched and bent. After this stage, the elastic deformation reaches its maximum and the lamellar-arranged chain segments begin to tilt, followed by the separation of blocks in the crystalline regions. In the last

stage, the separated crystalline blocks align in the direction of the tensile stress [22, 37]. More advanced models describing the interaction between molecules in the amorphous regions are described by Argon [38, 39], Lin et al. [40], Boyce et al. [41, 42], and Bartczak et al. [43–45]. Today it is well known that simple rearrangement of molecular chains can not fully describe the complex process of deformation in polymers. Properties like chain entanglement, free volume, chain length, and branching are determining factors for deformation behavior. Since thermal treatment has a significant impact on these variables, the thermal history must be taken into account. Despite the existence of many different models, describing the deformation of unordered solids in their glass state, there is one specific mechanism controlling plastic deformation. Deformation takes place through shear transformation zones (STZ), localized rearrangement of molecular clusters accompanied by yielding. This is also the case for amorphous polymers at temperatures beneath the glass-transition temperature (T_g) [46, 47]. For semi-crystalline polymers, the configuration of intercrystalline tie chains also plays an important role [48]. Bowden et al. [49] and Bartczack et al. [50] describes further mechanisms present in the deformation of crystalline regions in polymers. In addition to the slip of molecular chains over each other and crystal fragmentation, the presence and influence of dislocation activity are described. The response of polymers to stress in the dependence of applied strain and temperature can be described by constitutive modeling [51–53].
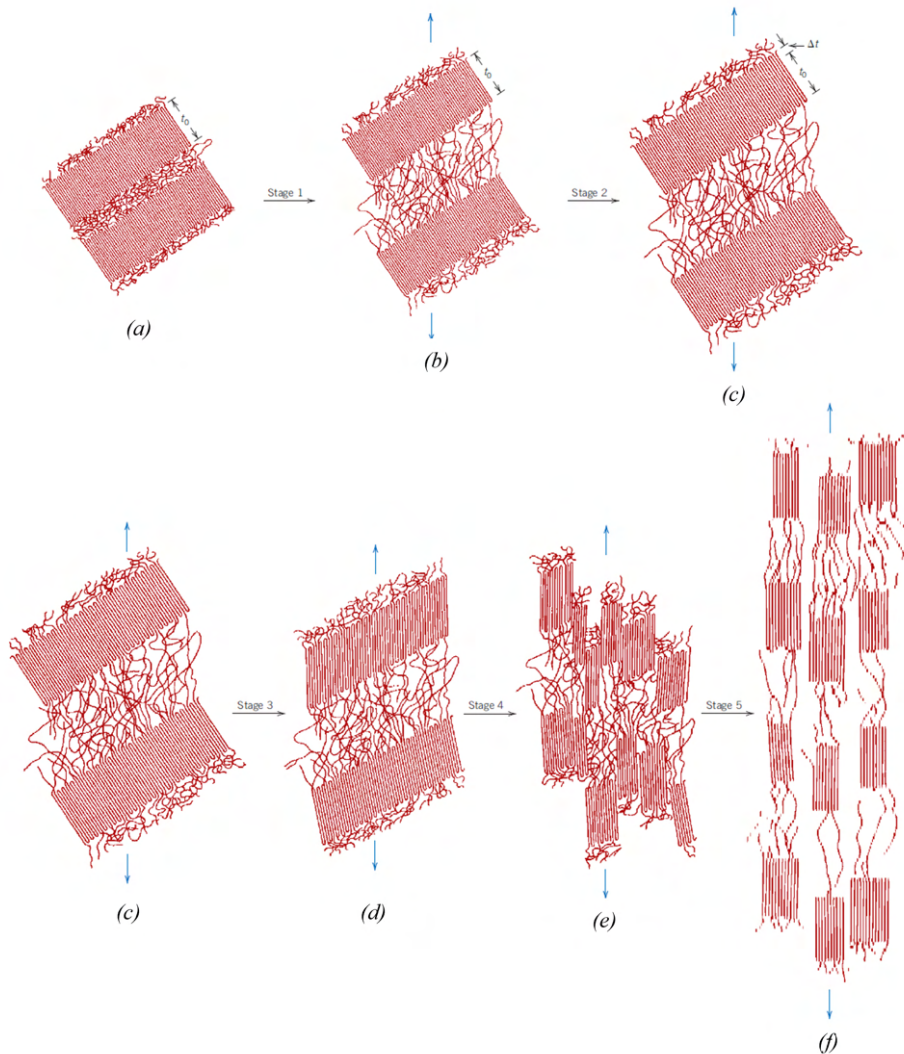
Figure 2.9.: Deformation mechanism of crystalline polymers, described by the molecular model: unde-formed polymer (a), elongation of amorphous regions (b), increase in lamellar crystallite size due to bending and stretching of chains in crystalline regions (c), onset of the plastic deformation, tilt of crystalline chain segments (d), separation of crystalline regions (e) and orientation of crystalline segments along the tensile stress axis (f). Reprinted from Callister et al. [22].

The two most common damage mechanisms in polymers are crazing and shear band damage. A craze is formed when multiple microvoids build up, leading to a crack-like structure with fibrils connecting the edges. Crazes occur preferably in tensile conditions where voids can build up easily. Shear band damage mainly occurs in deformation processes with constant volume [22, 37]. An example of these damage mechanisms is shown in figure 2.10
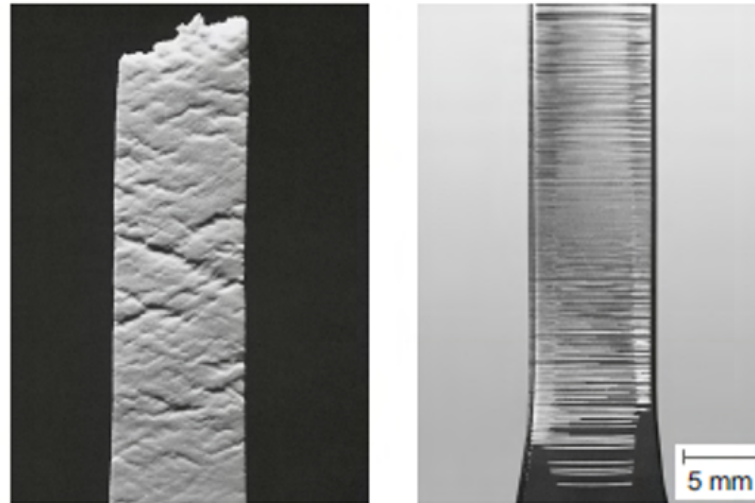
Figure 2.10.: Shear bands in acrylonitrile butadiene styrene copolymerisate (a) and crazes in polystyrene (b), reprinted from Ehrenstein et al. [37]. © CARL HANSER VERLAG GMBH & CO. KG.

2.2.2. Structure and Properties of Polymers

Polypropylene (PP)

The chemical structure and a schematic illustration of an isotactic polypropylene (PP) chain is shown in figure 2.11.
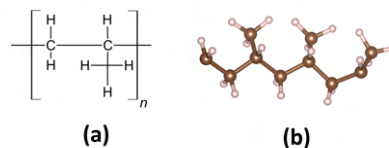
Figure 2.11.: Chemical structure of polypropylene (a), chain of isotactic polypropylene visualized using VESTA [54] (b).

PP is a polyolefin belonging to the standard polymers. It is widely used in technical applications, due to its versatility. In technical applications, the isotactic configuration (iPP) is a determinant for the crystallinity and plays a major role in adjusting mechanical properties. Furthermore, PP often is customized by either controlling the tacticity, copolymerization or by the formation of polymer blends [55]. The differences in thermo-mechanical behavior can be described by the dynamic shear modulus, as shown by Osswald et al. [56] in figure 2.12.
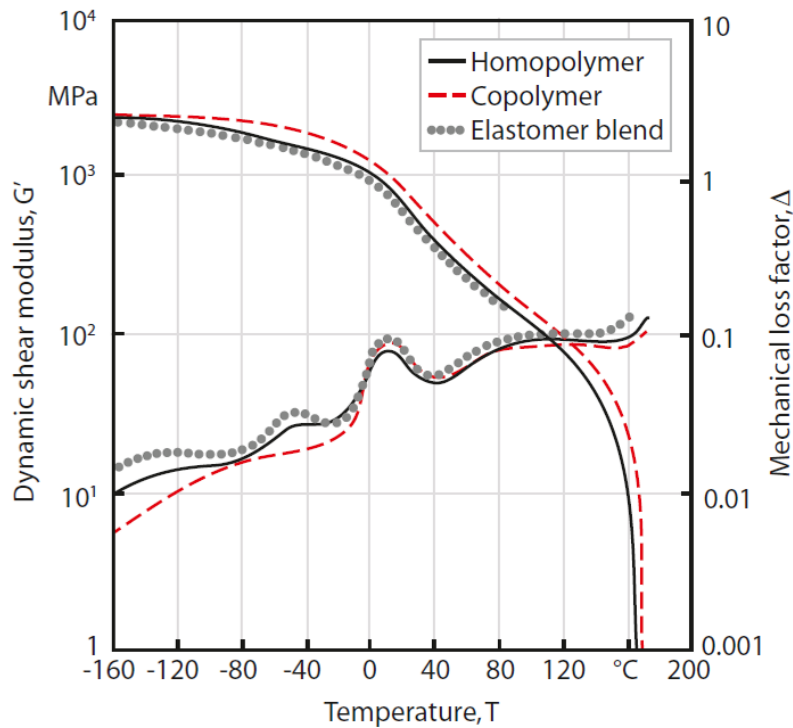
Figure 2.12.: Shear modulus and mechanical loss factor of PP, reprinted from Osswald et al. [56] .

Typical forming methods like vacuum forming, blow forming, rolling, stamping, or stretching are performed around the crystallite melting temperature (T_m) [55, 57]. According to Geier et al. [55] cold-forming like rolling and cold stamping represent suitable forming processes for PP in addition to thermoforming. In table 2.1 an excerpt of technical properties is shown. A more detailed overview of properties is presented in Appendix B.

Table 2.1.: Technical properties of PP [37, 57–59].

Property	Value
Density [g/cm³]	0.895–0.92
Copolymer	0.89–0.905
Glass transition temperature [°C]	-10– +20
Maximum service temperature [°C]	110
Crystallite melting temperature [°C]	158–168
Elastic modulus [MPa]	1100–1800
Copolymer	900—1200
Tensile strength [MPa]	21–40
Copolymer	28–40

Polyvinyl Chloride (PVC)

The chemical structure of polyvinyl chloride (PVC) is shown in figure 2.13.
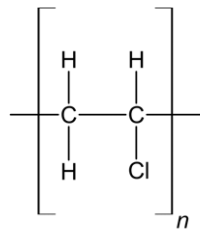
Figure 2.13.: Chemical structure of PVC.

PVC is an amorphous thermoplast belonging to the standard polymers. PVC can be customized with the use of different fillers and additives as plasticizers. One common filler for PVC is $CaCO_3$. For not plasticized PVC (PVC-U), mass fractions between 5 % to 10 % are common as processing agents [55, 57].

Forming processes are performed in a temperature range from 110 °C up to 140 °C or in a second process window at 160 °C to 180 °C. The latter is especially useful to maximize dimensional stability at elevated temperatures. The temperature of the tools plays an important role in the forming process [57]. In table 2.2 an excerpt of technical properties is shown. A more detailed overview of properties is presented in Appendix B.

Table 2.2.: Technical properties of polyvinyl chloride without plasticizers (PVC-U) [57–59].

Property	Value
Density [g/cm³]	1.32–1.58
Glass transition temperature [°C]	70–80
Maximum service temperature [°C]	60
Elastic modulus [MPa]	1000–3500
Tensile strength [MPa]	40-75

Polyoxymethylene (POM)

The chemical structure of polyoxymethylene (POM)) is shown in figure 2.14.
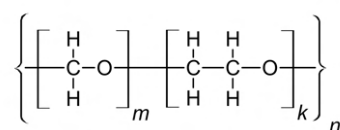
Figure 2.14.: Chemical structure of POM-C.

POM is a polymer with a wide range of applications. Since it shows highly linear chains, crystalline fractions of 70 %, and even higher are possible. For stabilization against UV-radiation aging, carbon black is used as an additive. In this thesis, POM is used as a copolymer (POM-C). Trioxane and 2-3-Dioxalane* react to form a copolymer [55, 57]. Such copolymers can display different arrangements of the chain blocks, as described by Osswald et al. [56] and displayed in figure 2.15.
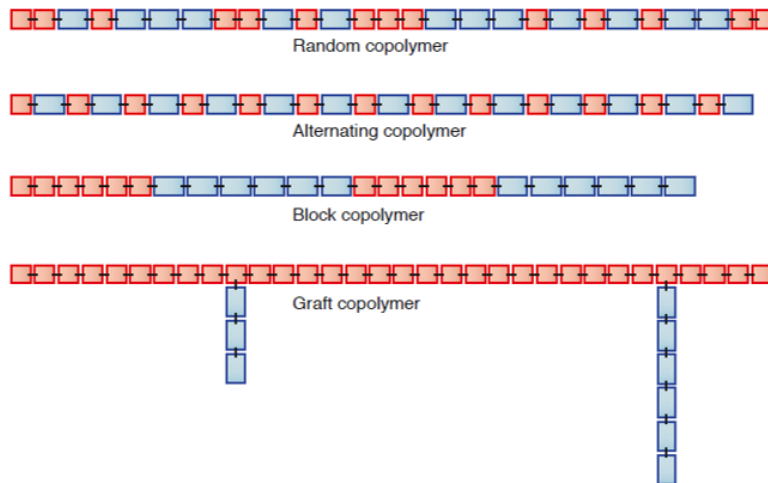
Figure 2.15.: Schematic illustration of different chain arrangements in copolymers reprinted from Owald et al. [56].

Usually, POM is processed using powders in a sintering process [60] or using a viscous mold state for blow molding, extrusion, or injection molding [55]. For special applications hot forming is possible in a process window between 160 °C and 170 °C [57]. At high temperatures POM is prone to decay releasing toxic formaldehyde [57]. An overview of the properties of POM is given in table 2.3 and appendix B

Table 2.3.: Technical properties of POM-C [37, 57–59].

Property	Value
Density [g/cm³]	1.39–1.43
Glass transition temperature [°C]	-70
Maximum service temperature [°C]	90–110
Crystallite melting temperature [°C]	164–172
Elastic modulus [MPa]	2600–3200
Tensile strength [MPa]	60–75

*Also different species, mainly ether or formalene can be used as co-monomer

Polyetheretherketone (PEEK)

The chemical structure of polyetheretherketone (PEEK) is shown in figure 2.16.
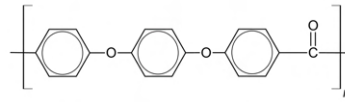
Figure 2.16.: Chemical structure of PEEK.

PEEK is considered a high-performance polymer and is well known for its high service temperature. It can exist in an amorphous and semi-crystalline state, by controlling the cooling rate from the melt, as described by Kemmish et al. [61]. Semi-crystalline PEEK is mostly processed by injection molding with heated tools. The tool temperature between 150 °C and 180 °C. Also, extruding is possible. For surface coatings and special applications, PEEK is also processed as powder utilizing sintering mechanisms [57]. An overview of the properties of PEEK is given in table 2.4 and appendix B.

Forming processing in the solid state is rather uncommon for PEEK. Nevertheless, the deformation of PEEK is a popular field of research for medical applications where PEEK implants are used as bone joints and membranes as described by Papia et al. [62].

Table 2.4.: Technical properties of PEEK[37, 57–59].

Property	Value
Density [g/cm^3]	1.265 amorphous 1.32 crystalline
Glass transition temperature [°C]	143– +145
Maximum service temperature [°C]	250
Crystallite melting temperature [°C]	334–381
Elastic modulus [MPa]	3600–3650
Tensile strength [MPa]	90–200

Polytetrafluorethylene (PTFE)

The chemical structure and a schematic illustration of a polytetrafluorethylene (PTFE) chain in the $^{15}/_7$ configuration, is shown in figure 2.17.

(a) **(b)**
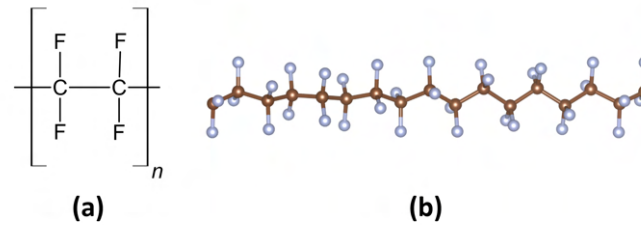
Figure 2.17.: Chemical structure of PTFE (a) and a polymer chain in the $^{15}/_7$ helical configuration visualized using VESTA [54] (b).

PTFE is considered a thermoelast since a gelatinous mass is formed instead of melting at the crystallite melting temperature. This is the result of the high binding forces between fluor (F) and carbon (C). Therefore, the primary processing operations are rather comparable with sintering processes. Typical forming processes are extrusion, hot stamping (250 °C to 320 °C) or impact molding after sintering at temperatures $\geq$ 327 °C. An overview of the properties of PTFE is given in table 2.5 and appendix B.

Table 2.5.: Technical properties of PTFE[37, 57–59].

Property	Value
Density [g/cm^3]	2.15–2.20
Glass transition temperature [°C]	125– 130
Maximum service temperature [°C]	250
Crystallite melting temperature [°C]	325–330
Elastic modulus [MPa]	400–750
Tensile strength [MPa]	7–30

PTFE is somewhat special as it displays four different arrangements of the crystalline microstructure. A schematic phase diagram, created from the work of E. Clark [63, 64], G. Fatti [65] and E.N. Brown [66] is given in figure 2.18. The transition from PTFE II to PTFE IV at ambient pressure is worth mentioning, as it is accompanied by a change in volume of the crystalline fraction of $\sim 1\,\%$.
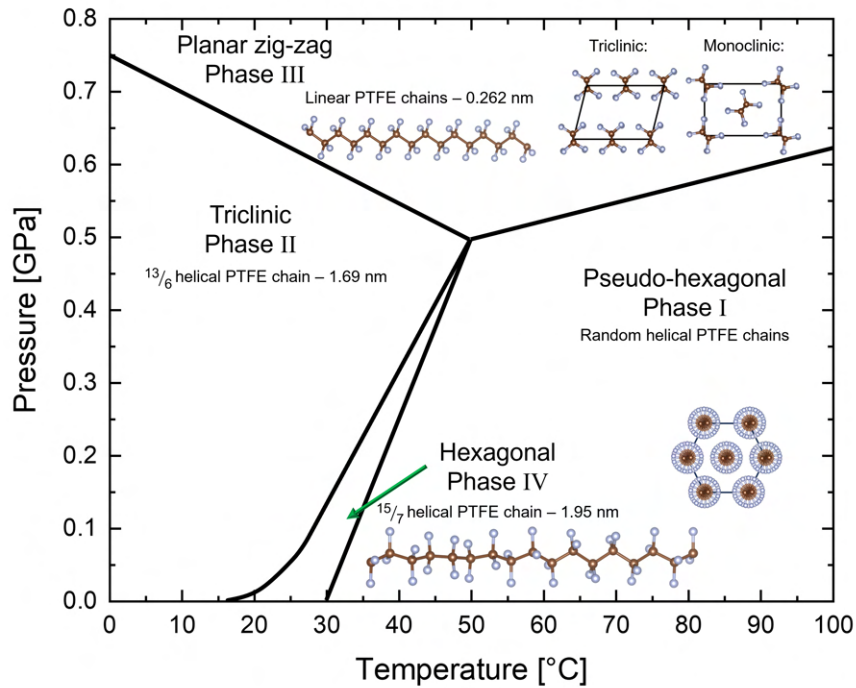
Figure 2.18.: Phase diagram PTFE, according to the work of E. Clark [63, 64], G. Fatti [65] and E.N. Brown [66]. Structures visualized using VESTA [54].

2.2.3. Structure and Properties of Metals

As metal phases in the composites, Cu, Cr, and Fe are chosen. Essential for the experiment is the use of one AFM, one DM, and one FM material in a composite with FiM material. The deformation behavior also differs forchosen metals as they have different crystallographic structures and exhibit different dislocation mobilities as well, as different work hardening behavior [67]. The general properties of these metals are depicted in table 2.6, body-centered cubic and face-centered cubic are abbreviated with bcc and fcc.

Table 2.6.: General properties of used metals.

Material	Crystal structure	Magnetic behavior	Yield Strength [MPa]	Elastic modulus [GPa]
Cu	fcc (Fm̄3m)	DM	144 [68]	117 [69]
Cr	bcc (Im̄3m)	AFM	280 -300 [70]	161 [71]
Fe (Armco iron)	bcc (Im̄3m)	FM	110 [72]	206 - 214 [73]

2.2.4. Structure of Magnetic Materials

$SrFe_{12}O_{19}$ M-Type Hexaferrites

M-type hexaferrites are magnetic oxide ceramics. Their structure is hexagonal belonging to the space group $^{P6_3}/_{mmc}$ with a chemical composition like $MFe_{12}O_{19}$ where M is barium (Ba), strontium (Sr) or lead (Pb). Through indirect exchange mechanisms, a ferrimagnetic spin ordering is established [74–76]. Figure 2.19 shows the crystal structure of $SrFe_{12}O_{19}$, where the Fe atoms marked with f_1 and f_2 exhibit-spin down whilst a, b and k have a spin-up orientation [74, 75].
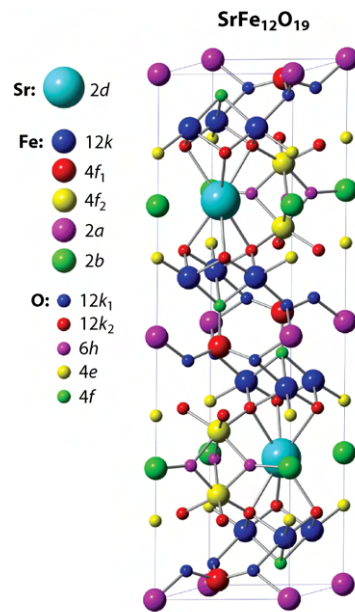
Figure 2.19.: Crystal structure of $SrFe_{12}O_{19}$, reprinted from MC Callum et al. [74].

Through substitution of the primary element Sr with atoms like Ba, calcium (Ca), or similar cations, the magnetic properties can be tuned as the dimensions of the unit cell slightly vary [77]. Commercial ferrite magnets are usually produced using pressing of powders followed by sintering and magnetization processes. $SrFe_{12}O_{19}$ powder particles exhibit a hexagonal platelet form, which can be influenced during the calcination process [75, 78, 79]. $SrFe_{12}O_{19}$ ferrites show a rather high magneto crystalline anisotropy ($3.5 \times 10^5\,J/m^3$ [80]) along the c-axis. This leads to high values of H_c and rather low B_r, compared with AlNiCo magnets [79].

AlNiCo Alloys

AlNiCo magnets were discovered in the 1930s and are based on the spinodal precipitation of ferromagnetic α_1 particles in a paramagnetic α_2 matrix [81, 82]. According to Mc Currie [81], the precipitation reaction in Fe_2NiAl follows

$$3.25\,Fe_{50}Ni_{25}Al_{25} \rightleftharpoons Fe_{95}Ni_{25}Al_{25} + 2.25\,Fe_{30}Ni_{35}Al_{35} \cdot \qquad (2.2)$$
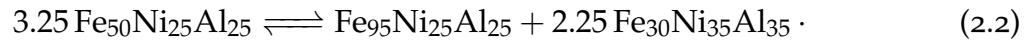
In this early $Al-Ni-Fe$ System a third γ phase is also existent. Whilst both α phases are bbc structured, the γ phase is fcc structured and exhibits a DM behavior. Thus, the γ phase is unwanted and harmful to the magnetic properties. In modern magnets, the γ phase is suppressed by sophisticated cooling processes or alloying elements, which narrow down the γ region in the phase diagram [81, 83]. Optimization efforts resulted in new alloys, in the AlNiCo 3 alloy Cu increases the BH_{max}. In AlNiCo 5, and AlNiCo 8 alloys, the introduction of Co not only resulted in higher H_c and BH_{max} but also a critical change in microstructure. The α_1 phase now is a ferromagnetic FeCo-rich phase while the α_2 phase is a paramagnetic AlNi-rich phase [81, 83]. Mc Callum et al. [74] describes the occurring lattice ordering in AlNiCo as bcc or B2 structure for AlNiCo grades without Titanium (Ti) and as a combination of B2 and $L2_1$ structure for AlNiCo grades with Ti, as depicted in figure 2.20. In all cases, the precipitates form in a bcc or B2 structure. Furthermore, Rehmann et al [84] showed in their work that additives in AlNiCo 8 alloys, like silicon (Si), zirconium (Zr), and niobium (Nb) can form additional ferromagnetic phases at the grain boundaries. In table 2.7 the chemical composition of the AlNiCo grades AlNiCo 3, AlNiCo 5 and AlNiCo 8 are described.
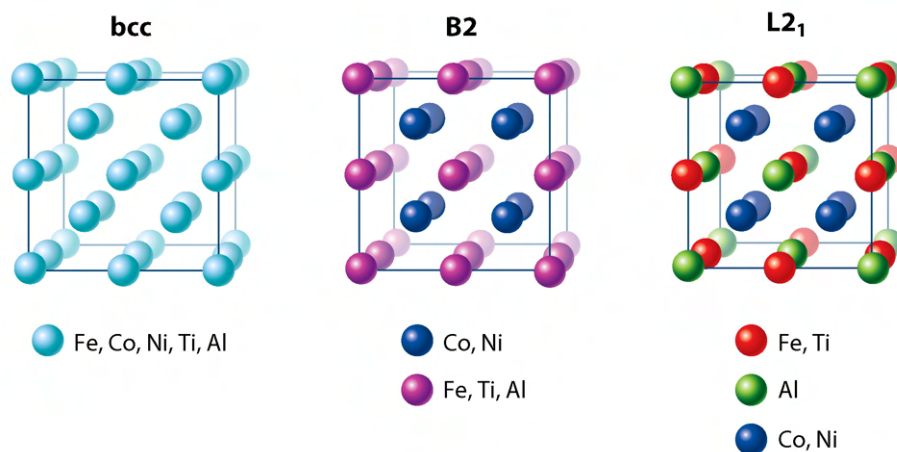
Figure 2.20.: Crystal structures in AlNiCo alloys, reprinted from MC Callum et al. [74].

Table 2.7.: Chemical composition of AlNiCo alloys according to MMPA standard
No. 0100-00. [85]

Alnico	Al [%]	Ni[%]	Co [%]	Cu [%]	Ti [%]
3	12	25	-	3	-
5	8	14	24	3	-
8	7	15	35	4	5

2.3. Severe Plastic Deformation (SPD)

The tuning of materials by deformation is a long and well-known method to achieve material grades with exceptional properties. Classical methods utilizing phenomena like work hardening or recrystallization to produce new materials are thermo-mechanical treatments. SPD takes it one step further, using deformation parameters like high pressures to hinder crack formation. Therefore, not only the creation of ultrafine-grained (UFG) and nano-crystalline materials are possible, but new alloys by supersaturation or hybrid materials can be created [86]. The first historical SPD-like methods are the forging of damascus steel and the japanese mokume-gane technique. In both methods, the sheets of two different metals are stacked in an alternating order and were then deformed. Whilst damascus steel is produced by forging and folding and the mokume-gane sheet is processed by rolling and folding, repeated folding and deformation have a similar effect in both techniques. A huge amount of strain is imposed on each layer, with each deformation leading to a layered microstructure, multiplying the number of layers with every folding. These two examples are also the first ones using such a method for composites. In the late 20th century, new possibilities and technologies emerged. With an increasing amount of studies and understanding of deformation and damage mechanisms in materials, the deformation methods evolved. Modern SPD techniques are a feasible way to produce UFG and nano-crystalline materials without complicated heat treatments and precipitation building elements [86]. Today, there are a variety of SPD methods:

- Accumulative roll bonding (ARB)
- High-pressure torsion (HPT)
- Twist extrusion (TE)
- Equal channel angular pressing (ECAP)

to mention only a few. Especially in the last two decades, SPD became more popular with rising demand for materials with unique properties or functional nano-materials for nuclear applications, the energy sector, aerospace, or medical applications [86, 87].

2.3.1. High-Pressure Torsion (HPT)

HPT is a SPD technique, applying uni-axial pressure on a disk-shaped sample between two anvils. After the pressure loading, one anvil rotates against the second fixed anvil, leading to a plastic deformation within the sample. This deformation is usually accompanied by a microstructural refinement, depending on the material used [88]. For an idealized HPT process, the applied strain can be calculated using:

$$\gamma = \frac{2\,\pi\,n}{t}\,r \tag{2.3}$$

or using the von Mises strain

$$\varepsilon_{vM} = \frac{2\,\pi\,n}{\sqrt{3}\,t}\,r \tag{2.4}$$

where γ is the strain, n is the number of revolutions, r is the radial position from the center of the rotational axis, and t is the thickness of the sample [89]. In consequence of this relation, idealized HPT, figure 2.21 (b), leads to a linear strain gradient, rising from 0 at the rotation axis and ending in a maximum at the outer edge of the sample instead of a uniform strain and microstructure.

Moreover, the geometry of the sample has an influence on the evolving microstructure. For a homogeneous microstructure in the axial direction, it is critical to maintain a t/d ratio. Where d is the sample diameter. This aspect ratio of the sample is dependent on the ductility and deformation mechanisms present in the sample. For metals, an aspect ratio of ⅒ to ⅛ usually leads to a uniform microstructure, whilst for ceramics much thinner samples are needed [89, 90]. In normal torsion testing, ductile materials exhibit failure by void formation followed by coalescence and crack initiation, and shear damage mechanisms as mathematically described in the shear-modified Gurson–Tvergaard–Needleman model. In the HPT process, these mechanisms can be partly suppressed by the pressure imposed on the sample. Therefore, cracks mainly form along shear bands and propagate under a Mode III loading [91, 92]. Suppression of these damage mechanisms leads to much higher possible strains, in some cases also to superplasticity. One more important parameter is the friction between the sample and the anvil surface. To ensure a uniform and well-defined deformation, slipping

of the sample is not allowed. A sufficient high friction between sample and anvil is required. This can be ensured by sandblasting of the anvils and implementing a defined surface roughness. Furthermore, the sandblasting accompanied by cleaning with ethanol ensures that the surface is clean and free from any lubricating substances [92].

Experimental Implementation

Today three different HPT set-ups are used. In the idealized unconstrained HPT, depicted in figure 2.21 (a), the sample is deformed between two flat anvils without any change in volume or thickness. Since in a real experiment, the material used can unhinderedly flow out between the edges of the anvils. This often is considered as a major drawback of this set-up, hence the sample gets thinner during compression and with a rising amount of revolutions, eventually leading to contact between the anvils. To avoid this drawback, especially for ductile and soft materials the constrained HPT, figure 2.21 (b), can be used. The idealized constrained HPT ensures a constant volume of the sample as well as a uniform shear deformation by placing the two anvils in a frictionless outer cylinder. This also changes the loading conditions from uniaxial pressure to a hydrostatic pressure. Whilst these changes theoretically bring huge improvements, the realization is difficult. Since a frictionless assembly is impossible and the anvils must be slightly smaller than the outer cylinder, the real process holds some challenges. Hence, there is a small slit between the anvils and the outer cylinder sample material will flow into the slit, causing an increasing additional friction, which could lead to cold welding of the set-up. Another drawback is the limitation of the loading force. This limitation is caused by the fact that the anvils and sample are equal in diameter, and the pressure is limited to the compressive strength of the anvils. The third set-up shown in figure 2.21 (c) is the quasi-constrained HPT. With this set-up the advantages of the idealized constrained HPT are implemented in a controllable real process. Here, the sample is placed in a cylindrical cavity in the rotational center of the anvils. While the surface of the cavity is sandblasted, the cavity walls and the anvil surface are smooth and should posess a low friction coefficient. While the sandblasted cavity ensures deformation without slip, the cavity walls impede material flow and provide some guidance. When pressure is applied to the sample it is compressed accompanied by a change in the thickness of 5 % to 10 %. This excess material flows in the slit between the anvils, forming a burr, resulting in a slight back pressure. Thus, this bur is much thinner than the sample it gets much more deformed. In metals, this leads to work hardening, and further material is hindered from flowing out of the

cavity, resulting in quasi hydrostatic conditions in the sample processing zone [89, 92].
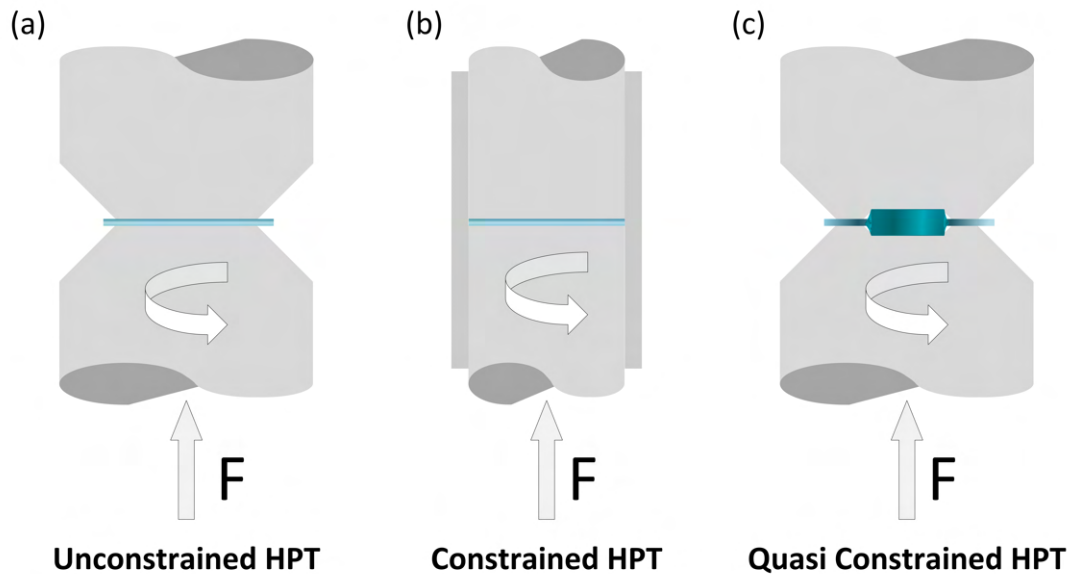
Figure 2.21.: Schematic illustration of possible HPT set-ups: a) unconstrained HPT b) constrained HPT and c) Quasi-constrained HPT.

For metals and ductile materials, the quasi-constrained HPT is the favorable process. But specimens that need a far lower aspect ratio and a less pronounced flow, like ceramics and minerals, may perform better in the unconstrained process [90, 92]. This thesis is focused on the quasi-constrained HPT.

Microstructural Evolution during HPT

Whilst the microstructural evolution is subject to many experimental studies, the mechanisms leading to the refinement are still under debate. During the deformation, a grain refinement and eventual mixing of phases occurs. Also, amorphization can occur in some cases. The main mechanism responsible for grain refinement is an accumulation of dislocations in the grain, leading to the generation of new grains out of subgrains. This refinement results in a nano-crystalline microstructure. Figure 2.22 shows this process of subgrain formation. At first, the dislocation density rises because of extensive straining (a), when dislocations pile up at grain boundaries or defects they begin to rearrange and form small angle subgrain boundaries (b). With ongoing deformation, the orientation mismatch of these subgrain boundaries increases (c), resulting in the formation of new smaller grains (d). In addition to this concept of grain refinement twining, and phase transformation can also contribute to the grain refinement [88].
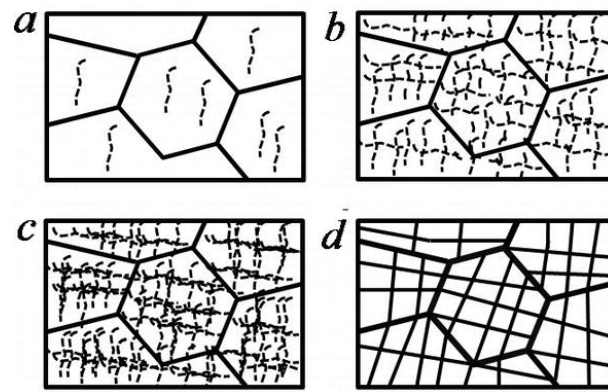
Figure 2.22.: Shematic of the grain refinement in ductile materials via (a) accumulation of dislocations (b) generation of small angle subgrain boundaries (c) increase of the misorientation (d) formation of new grain boundaries out of the subgrains [88].

In ceramics, the deformation mechanisms are different (cf. chapter: 2.1.3). For, in ceramics, a deformation based on dislocation gliding is far less pronounced than in metals. Often additional to the activation of twinning mechanisms and glide systems by a critical strain, temperature-activated diffusion mechanisms must be activated. Thus, high temperatures are needed for deformation. As a consequence, the main effect of the HPT is the breaking of existing grains along slip planes. this grinding effect is accompanied by the geometrical interlocking of the debris [36, 90].

It is important to recognize that Polymers exhibit a completely different behavior in the HPT process. One reason is the difference in constitution of metals and polymers. Materials like metals and ceramics display a long-range order between single atoms, which occupy places in a lattice structure depending on the chemical bonds between the atoms. However, polymers form complex structures by arranging their macro-molecules, as described in chapter 2.2.2. These structures are not uniform over the whole material, which leads to regions with different deformation properties. In semi-crystalline thermoplastic polymers, for example, crystalline lamellae are embedded in an amorphous matrix. In amorphous regions, polymer chains coil up to entangled structures. Deformation properties depend on the crystallinity, form, and orientation of crystalline sections and the present crosslinking density in the case of thermosets and elastomers. In general, polymers react much more sensitively to pressure and the occurring deformation. While in the case of metals, the interesting range of de-formation can easily reach up to 100 or more revolutions, the maximum achievable deformation in polymers lies between 5° and 400° or even below. The reason for this is the mechano-chemical destruction induced by pressure and or the deformation itself. Especially homopolymers are prone to fast degradation in HPT. Adverse to this, the properties of copolymers and polymer blends can be optimized and even new phases

can be formed. For that reason, HPT processing during the polymerization process of copolymers and polymer blends, resulting in a bimodal molar mass distribution, can be used to create polymers with new properties. Depending on the Polymer used, chemical and structural altering, amorphization, or new phases are observed [93].

2.3.2. Composite Materials by HPT

As mentioned before, HPT is capable of producing metastable materials utilizing the change of thermodynamic behavior of the materials under high pressure accompanied by excessive straining. Also, nanocomposites can be produced in a variety of possible processes. A. Bachmaier and R. Pippan [94] described how metal–metal and metal–ceramic composites are obtained by HPT. As starting materials powders, pre-deformed sheets or bulk materials are suitable. Qi et al. 2018 [95] also describes the combination of ceramic powder and metallic bulk materials. Depending on possible supersaturated solutions, the form and arrangement of the starting materials and different microstructures can be found in the processed samples.

The difference in mechanical properties should also be considered given the deformation processes present in HPT. Depending on the difference in yield strength and strain hardening the material displaying a lower yield strength is deformed first. During deformation, the necessary stress for further plastic deformation of this material increases due to strain hardening. Eventually, the yield strength of the stronger material is reached and co-deformation sets in. If the difference in yield strength is too big, fracture of the strain hardened material is more likely to occur than co-deformation. In addition, the size of material regions implies the deformation behavior, since deformation mechanisms are different in nanostructures and single crystals than in bulk materials. This factor can be influenced by ball-milling and sufficient mixing methods, as well as by the size and amount of segments in the multi-sector disc approach [7, 96–99].

The multi-sector disc approach is especially useful in the processing of layered metal composites. Since metal powders are prone to oxidation and therefore powder handling can be challenging, bulk material samples are an suitable alternative. Important parameters of this method are the amount of segments in the sample and the difference in mechanical properties [7]. If other materials than metals are used in this approach it also is important to ensure the adherence between those materials. Since with ongoing deformation new surface areas are created, which can not be surface

treated in advance and cold welding is not possible between some materials, a certain level ov adherence is necessary to form stable, layered composites [7, 97, 99].

3. Experimental

3.1. High-Pressure Torsion of Polymers

For the initial experiments, two routes of sample preparation for the HPT experiments are chosen. The samples of PP (supplied by RS-online) and PTFE (unknown grade), for preliminary experiments, are prepared by turning rods 8 mm in diameter out of a sheet material. In a further step, discs with 1 mm thickness are cut from the rods using a Struers Secotom cutting machine. All other polymers are cut into disk-shaped samples, with the same geometry, from extruded rods. Thereupon, the sample surfaces are roughened with sanding paper, whilst the cavity surface of the HPT anvils is sandblasted. An anvil cavity of 0.2 mm in depth and 8 mm in diameter is selected for the HPT process. For each polymer, the deformation is carried out at room temperature (RT) and an elevated temperature between the glass transition temperature and the crystallite melting temperature [57]. Preliminary experiments are performed on PTFE with 1 GPa, and 5 revolutions at room temperature and 270 °C. All following experiments are limited to 1 revolution. Table 3.1 shows the selected process parameters. A rotational speed during deformation 0.6 rpm is used for all experiments. During all HPT experiments the applied pressure and torque are measured continuously.

Table 3.1.: Polymer HPT Samples.

Sample	Diameter [mm]	Pressure [GPa]	Revolutions	Temperature [°C]
PP_001	8	1	1	21
PP_002	8	1	1	100
PP_003	8	1	1	100
PVC_001	8	1	1	21
PVC_002	8	1	1	120
POM_001	8	1	1	21
POM_002	8	1	1	21
POM_003	8	1	1	160
PEEK_001	8	1	1	21
PEEK_002	8	1	1	21
PEEK_003	8	1	1	200
PEEK_004	8	1	1	200
PTFE_001	8	1	1	21
PTFE_002	8	1	1	200
PTFE_003	8	1	1	200
PTFE _t_001	8	1	5	21
PTFE _t_002	8	1	5	200

For the experiments at elevated temperatures, a hot air gun was used for temperatures $\leq 160\,°C$ and an inductive heating device for temperatures higher than $160\,°C$. Figure 3.1 shows these set-ups for the hot forming experiments. To characterize microstructural changes, all samples are examined with XRD.
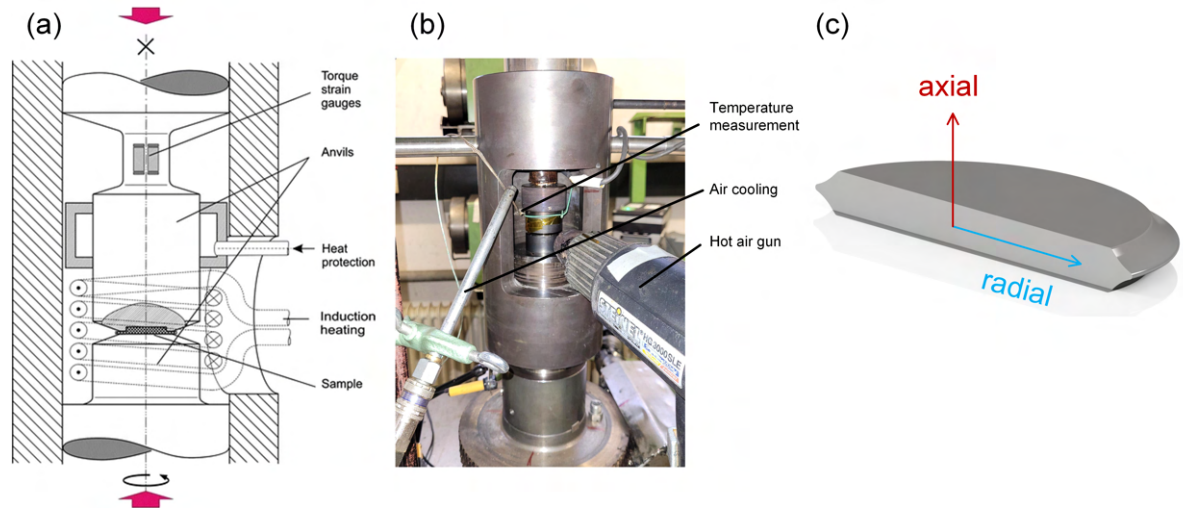
Figure 3.1.: Schematic setup of the HPT for the processing of polymers at elevated temperatures: (a) the heat is applied by inductive heating coils reprinted from Vorhauer et al. [100], (b) for samples with a low melting point, a hot air gun is applied to adjust the temperature and allow processing temperature $\leq 160\,°C$. (c) shows the orientations of the sample.

3.2. High-Pressure Torsion of Y35-Ferrite

Y35-ferrite magnets with a diameter of 10.3 mm in height are purchased from super-magnete.com. Purchased magnets boast a high porosity. To find the optimal parameters for the HPT processing, a series of experiments, starting with the axial pressing of Y35 ferrites at different pressures followed by deformation with 0.25, 0.5, 1 and 5 revolutions are conducted. The rotational speed is set to 0.6 rpm and the cavity depth of the anvil is 0.2 mm for all experiments. Table 3.2 and table 3.3 show the detailed parameters used for the Y35-ferrite samples.

Table 3.2.: Y35-ferrite HPT deformed samples.

Sample	Diameter [mm]	Pressure [GPa]	Revolutions	Temperature [°C]
Y35_001	10	2.5	1	21
Y35_002	10	5	1	21
Y35_003	10	5	5	21
Y35_004	10	5	5	500
Y35_005	10	5	1	500
Y35_007	10	5	0.25	21
Y35_008	10	5	0.25	21
Y35_009	10	5	0.25	21
Y35_010	10	5	1	21
Y35_011	10	5	1	21
Y35_012	10	5	0.5	21
Y35_013	10	5	0.5	21
Y35_015	10	5	0.25	21
Y35_016	10	5	1	21

Table 3.3.: Y35-ferrite HPT compressed samples.

Sample	Diameter [mm]	Pressure [GPa]	Temperature [°C]
Y35_comp_001	10	5	21
Y35_comp_002	10	5	500
Y35_comp_003	10	2.5	21
Y35_comp_004	10	2.5	21
Y35_comp_005	10	5	21
Y35_comp_006	10	5	21
Y35_comp_007	10	5	21

3.3. High-Pressure Torsion of AlNiCo Magnets

Commercially used AlNiCo magnet grades of cast AlNiCo 3, AlNiCo 5 and AlNiCo 8 are purchased from Bunting magnets. Each AlNiCo grade is sandblasted and deformed for 1 revolution afterwards. For the HPT process, a pressure of 7.5 GPa, and a rotational speed of 0.6 rpm is used. After the deformation, optical microscopy, SEM, and XRD are used to characterize microstructural evolution. In table 3.4 the AlNiCo with associated parameters are shown.

Table 3.4.: AlNiCo HPT Samples.

Sample	Diameter [mm]	Height [mm]	Pressure [GPa]	Revolutions	Temperature [°C]
AlNiCo 3_001	8	3	7.5	1	21
AlNiCo 3_002	8	3	7.5	1	21
AlNiCo 5_001	8	3	7.5	1	21
AlNiCo 5_002	8	3	7.5	1	21
AlNiCo 8_001	8	3	7.5	1	21
AlNiCo 8_002	8	3	7.5	1	21

3.4. Fabrication & Optimization of Magnetic Composite Materials

For the fabrication of composite materials, the multi-sector disc approach proposed by A. Hohenwarter is used [7]. In contrast to the experiments performed by A. Hohenwarter, single pieces were arranged in an alternating pattern without any bonding and then processed via quasi-constrained HPT. The expected result is a composite with a fine layered structure. In figure 3.2 a schematic illustration of the multi-sector disc approach is shown. In the first proof of concept, a composite consisting of Cu and Armco 617 is fabricated. The sample consists of ¼ pieces with a thickness of 1 mm, manufactured by electrical discharge machining. All pieces and the anvil's cavities are sandblasted and cleaned before assembling. For all composites anvils with a cavity of 0.2 mm is used. The multisector stock is consolidated at a pressure of 5 GPa prior HPT deformation applying 5 revolutions at a rotational speed of 0.6 rpm. Bulk metals are provided by the Erich Schmid Institute Leoben (ESI).
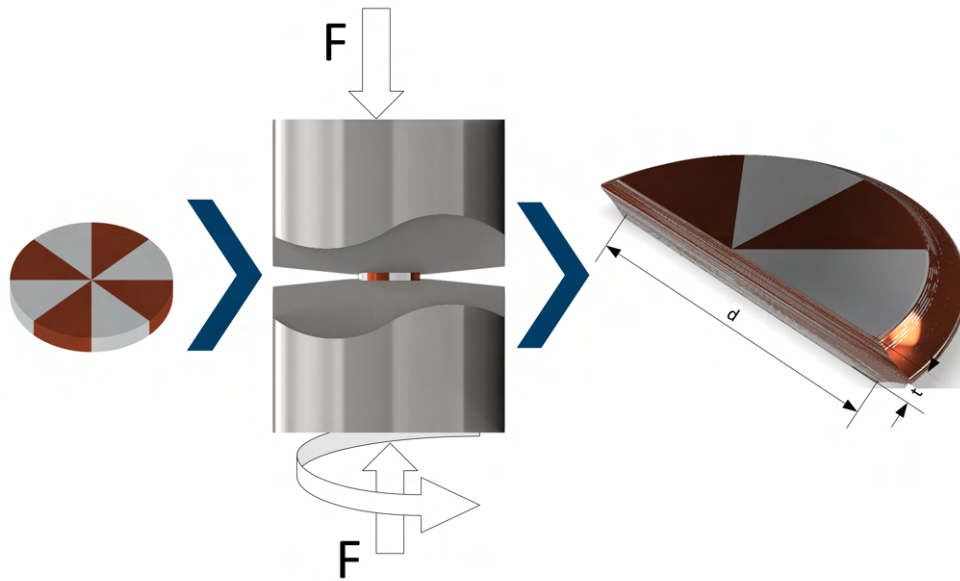
Figure 3.2.: Schematic setup of the HPT for the multi-sector disc approach: the segments are assembled in a disc and then deformed by HPT. The resulting sample shows a thin-layered architecture of the two alternating phases.

3.4.1. Fabrication & Optimization of Polymer-Metal Composites

To assess the co-formability of the different polymers, composites are fabricated by combining PVC, POM and PEEK with Cu in the multi-sector disk approach. To optimize the resulting structure and compensate for the huge difference in yield strength of the metal and the polymers several optimization steps are conducted. It is shown in Figure 3.3 the first composite is fabricated using the standard constrained HPT set-up, using anvil cavities of 0.2 mm in depth. In the first optimization the loss of polymer material is minimized by inserting a ring in the cavity, which can be seen in figure 3.3 b). To increase the homogeneity of the composite and further mitigate the difference in the mechanical properties, the anvil is modified. A larger plane surface around the cavity increases the present outlet resistance caused by higher friction. Thus, leading to an increase of lateral pressure on the sample. In addition, the axial pressure is also increased to 5 GPa. One final optimization is implemented figure 3.3 c) by using 8 segments and increasing the number of revolutions to 3. To simplify the assembling process the diameter of the Cu-ring is increased. The latter set-up is shown in figure 3.3 d).
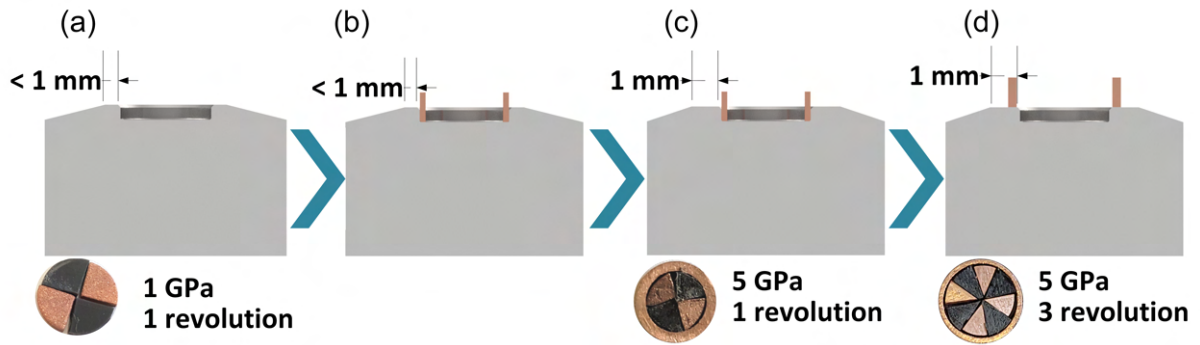
Figure 3.3.: Schematic illustration of the optimization steps in the fabrication of polymer-metal composites: a) deformation with ¼ pieces and standard quasi-constrained HPT and the process parameters previously used for polymers. b) an inserted copper ring provides additional pressure and mitigates vast differences in mechanical properties. c) the enlargement of the flat surface around the cavity provides a higher lateral pressure on the sample and minimizes the material loss through the slit. Also, the pressure is increased to 5 GPa. d). The ring is now located outside the cavity and the amount of deformation is increased to 3 revolutions with a sample consisting of ⅛ pieces.

One important factor in the fabrication of polymer-metal composites is the adhesion between the polymer and the metal. To improve the adhesion and minimize degradation, experiments are also conducted at elevated temperatures. The parameters used for each sample are summarized in table: 3.5.

Table 3.5.: Polymer-metal composite multi-sector disc HPT samples.

Sample	Diameter [mm]	Pressure [GPa]	Revolutions	Sectors	Temperature [°C]
PVC-Cu_001	8	1	1	4	120
PVC-Cu-R_001	8	1	1	4	120
PEEK-Cu_001	8	1	1	4	200
PEEK-Cu_R_001	8	1	1	4	200
POM-Cu_R_001	8	5	1	4	160
POM-Cu_R_002	8	5	3	8	21

3.4.2. Fabrication & Optimization of Y35 Composites

Composite fabrication is performed by cutting commercial Y35-ferrites using a wire saw and deformed with metals and polymers. Cr 625, Fe, and Cu-bulk metals are prepared in ¼ sectors by electro-discharge machining. To ensure a high friction between the sample and the anvils, and also clean surfaces, the metal sectors are sandblasted. All ferrite sectors are sanded by abrasive paper to roughen the surface. Then the ferrite and metal sectors are assembled in the anvil cavity in an alternating pattern. As process parameters, 5 GPa pressure and 5 revolutions are chosen. The rotational speed for all Y35 composites is set to 0.6 rpm. After the deformation all samples are cut in half

using a wire saw, and the phase distribution is evaluated by light microscopy. Table 3.6 shows the process parameters for the Y35-metal composites processed using 4 sectors.

Table 3.6.: Ferrite-metal composite multi-sector disc HPT samples.

Sample	Diameter [mm]	Pressure [GPa]	Revolutions	Sectors	Temperature [°C]
Y35-Cu	10	5	5	4	21
Y35-Fe	10	5	5	4	21
Y35-Cr	10	5	5	4	21

To achieve an enhancement in the phase distribution, the samples are processed by decreasing the volumetric fraction of the metal sectors. Thus, 8 sectors of Y35 are separated by assembling 8 Y35-sectors separated by metal sheets. Figure 3.4 shows the following optimizations in the process. In addition, the thickness of the metal sheets is modified [101]. In Table 3.7 the process parameters of the samples, using sheets, are presented.
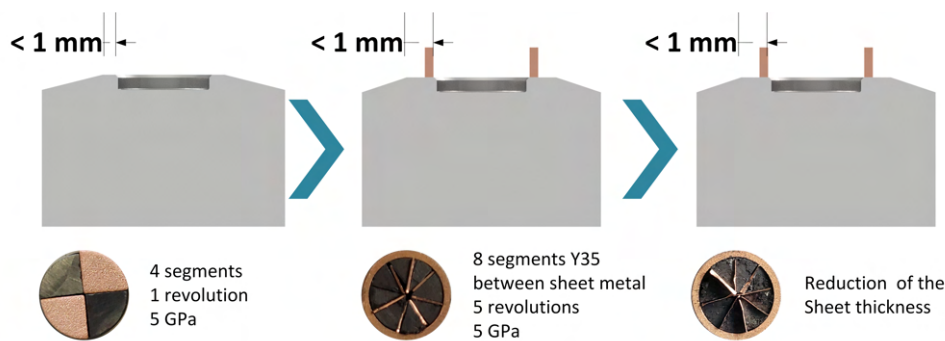
Figure 3.4.: Optimization of the fabrication process of magnetic Y35-metal composites using the multi-sector disc approach: the ¼ sectors used at the beginning are subsequently replaced by sheet metal.

Table 3.7.: Ferrite-metal composite multi-sector disc with sheet inlay, HPT samples.

Sample	Diameter [mm]	Pressure [GPa]	Revolutions	Sectors	Sheet thickness [mm]	Temperature [°C]
Y35-Cu_s_001	10	5	5	8	0.3	21
Y35-Cu_s_002	10	5	5	8	0.1	21
Y35-Fe_s_001	10	5	5	8	0.15	21
Y35-Fe_s_002	10	5	5	8	0.54	21

For the Y35-polymer composites, a similar approach is used. As samples surrounded by a copper ring exhibit far better deformation behavior in the case of metal-polymer composites, this set-up was initially used for the Y35-polymer composites. In the preparation process, ⅛ sectors are cut from Y35 and polymer disks using a wire saw and sanded for assembly. The sectors are cleaned with ethanol and then assembled alternating inside a copper ring. In a final preparation step, the surface is roughened with sandpaper to ensure high friction between the sample and the anvil.

After the assembly, the samples, shown in table 3.8 are deformed at a pressure of 5 GPa for 2 revolutions. To assess the influence of post-deformation annealing (PDA) on the bonding and the adhesion at the interfaces between phases one identical sample is annealed after the deformation. The composites are bisected and the microstructure is evaluated.

As shown in table 3.8 POM was examined in this set-up. The PDA is conducted under atmospheric pressure at 160 °C for 15 min. This temperature is used for hot forming of POM in the industry [57]. Therefore, the polymer is able to flow and fill out pores and cavities leading to a better cohesion of the composite.

Table 3.8.: Ferrite-polymer composite multi-sector disc HPT samples.

Sample	Diameter [mm]	Pressure [GPa]	Revolutions	Sectors	Temperature [°C]
Y35-POM_R001	10	5	2	8	21
Y35-POM_R002	10	5	2	8	21 °C and annealed 160 °C 15 min

Further, POM and PTFE are processed using a slightly modified sample assembly. The ⅛ sectors are replaced by polymer sheets and the remaining Y35 are sanded to fit in the now smaller spaces, as depicted in figure 3.5. Deformation parameters are changed to 2 revolutions at 5 GPa. The PDA process now is conducted under pressure, using the hot air gun. All process parameters are shown in table 3.9
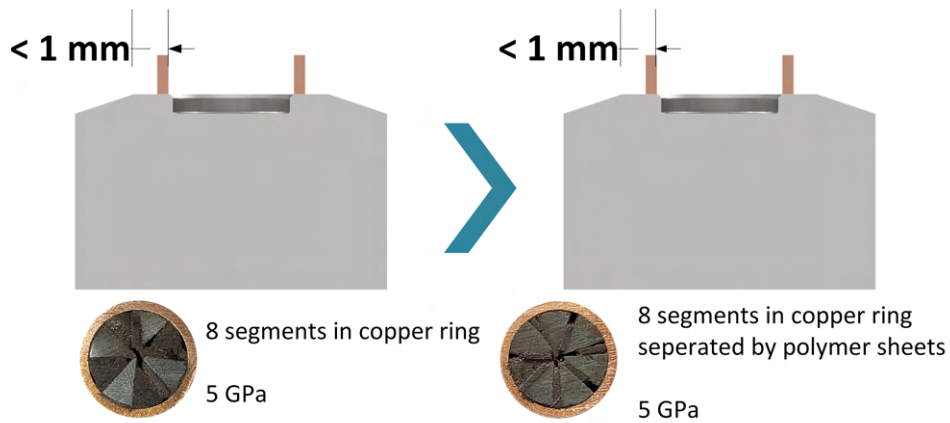
Figure 3.5.: Optimization of the fabrication process of magnetic Y35-polymer composites using the multi-sector disc approach: the ⅛ sectors pressed in a Cu ring used at the beginning are replaced by polymer sheets.

Table 3.9.: Ferrite-Polymer composite multi-sector disc with sheet inlay, HPT samples.

Sample	Diameter [mm]	Pressure [GPa]	Revolutions	Sectors	Sheet thickness [mm]	Temperature [°C]
Y35-PTFE_s_001	10	5	5	8	0.85	21
Y35-POM_s_001	10	5	2	8	0.5	21 °C +annealed 160 °C 15 min
Y35-POM_s_002	10	5	2	8	0.5	21

3.4.3. Fabrication of SrFe$_{12}$O$_{19}$ Powder-Composites

For the fabrication of composite materials by HPT using powders as starting materials, SrFe$_{12}$O$_{19}$ is mixed with a second species in a volume ratio of $\varphi_i = 50\%$. The starting materials are listed in table 3.10.

Table 3.10.: Starting powder.

Manufacturer	Chemistry	Purity	Specification
Hauner gmbH	Cu	99.70 %	100 µm
Alfa Aesar	Cr	99%	-325 mesh
Matek	Fe	99.90 %	-100+200 mesh
SigmaAldrich	PTFE		$\geq$ 40 µm
SigmaAldrich	SrFe$_{12}$O$_{19}$	99.50 %	-325 mesh

After the mixing by shaking, the powder was processed by HPT as shown in figure 3.6. All process steps including loose powder are performed in a glovebox under an inert atmosphere. In a first step a copper ring is glued on the lower anvil, with a cavity of 0.25 mm, and filled with powder, and an enclosure is placed around the anvil. After the second anvil is placed on top of the lower anvil and aligned, the enclosure is sealed to ensure an inert atmosphere during compaction. Billets with a diameter of $\varnothing$ 8 mm and an average height of 1.5 mm are pressed with 2.5 GPa and ¼ revolution. For the compaction and deformation the same rotational speed of 0.6 rpm is used. The Billets are later cleaned and deformed. For the deformation the anvils with a cavity of 0.2 mm are prepared by sandblasting. Then the deformation is conducted at 5 GPa for 5 revolutions with the same rotational speed as used for compaction. The samples and parameters are summarized in table 3.11. After the HPT process, a microstructural analysis using SEM and XRD is conducted. Additionally, magnetic hysteresis loops are measured in the compressed and deformed state.
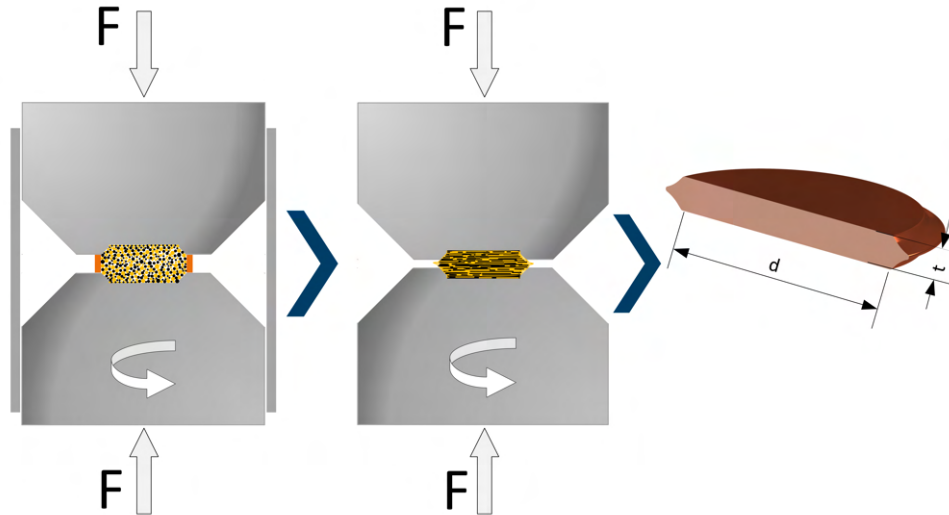
Figure 3.6.: Schematic setup of the HPT for the powder processing: the powder is filled in a copper ring. Then pressed as the anvil moves for 90°, in an enclosure. In a further step, the pressed disc is deformed via HPT. During deformation, the particles get stretched and refined.

Table 3.11.: SrFe12O19-powder composite HPT samples.

Sample	Diameter [mm]	Pressure [GPa]	Revolutions	Powder	Temperature [°C]
PC001_SrFeO-PTFE_P004	8	5	5	P004	21
PC002_SrFeO-PTFE_P004	8	5	5	P004	21
PC003_SrFeO-Cr_P002	8	5	5	P002	21
PC004_SrFeO-Cr_P002	8	5	5	P002	21
PC005_SrFeO-Fe_P003	8	5	5	P003	21
PC006_SrFeO-Fe_P003	8	5	5	P003	21
PC007_SrFeO-Cu_P001	8	5	5	P001	21
PC008_SrFeO-Cu_P001	8	5	5	P001	21
PC009_SrFeO-Cu_P001	8	5	5	P001	21
PC010_SrFeO-Cr_P002	8	5	5	P002	21
PC011_SrFeO-Fe_P003	8	5	5	P003	21
PC012_SrFeO-PTFE_P004	8	5	5	P004	21
PC013_SrFeO-PTFE_P004	8	5	5	P004	21
PC014_SrFeO-PTFE_P004	8	5	5	P004	21
PC015_SrFeO-Cr_P002	8	5	5	P002	21
PC016_SrFeO-PTFE_P004	8	5	5	P004	21

3.5. Annealing of Y35-Ferrites

To study the influence of thermal treatment on commercial Y35-ferrites, a series of annealing experiments are conducted. Commercial ferrites are annealed under atmospheric conditions at 300 °C, 500 °C, 700 °C, 900 °C and 1100 °C. After the annealing, the ferrites are air cooled. A schematic profile is given in figure 3.7.
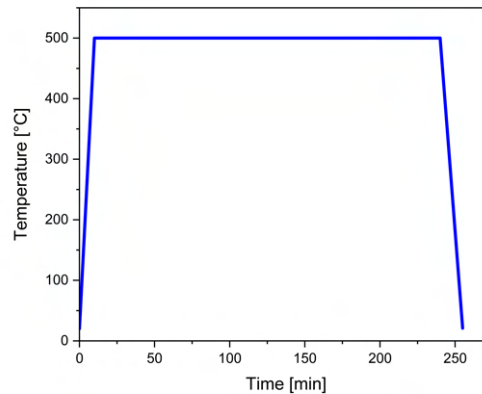
Figure 3.7.: Schematic temperature profile of the annealing process.

Analysis of the microstructure and occurring changes in chemistry or crystallography are conducted with light microscopy (Olympus BX51) and XRD like described in chapter 3.6. Changes in porosity are evaluated using the ImageJ software. A detailed description of the method used is provided in appendix A.1. The influence on the magnetic properties is evaluated via measurements of full hysteresis loops using a Brockhaus hystograph HG 200.

Table 3.12.: Annealed Y35-ferrite.

Sample	Temperature [°C]	Time [h]
Y35_006	500	4
Y35_014	300	4
Y35_018	500	4
Y35_019	700	4
Y35_020	900	4
Y35_021	1100	4

3.6. X-Ray Diffraction

For the XRD experiments, a Bruker D2 Phaser table-top instrument is used. All experiments are conducted with Co K_α radiation with a mean wavelength of 0.179 026 nm. To collimate the incident beam, a 2.5° soller slit and a 0.6 mm divergence slit are used. A 1 mm scatter screen above the sample reduces the signal coming from the sample holder, by reducing the irradiated area. In the secondary beam path, an Fe–filter is used to reduce the K_β peaks in front of a soller slit and the 1D Lynxey line detector as shown in figure 3.8.
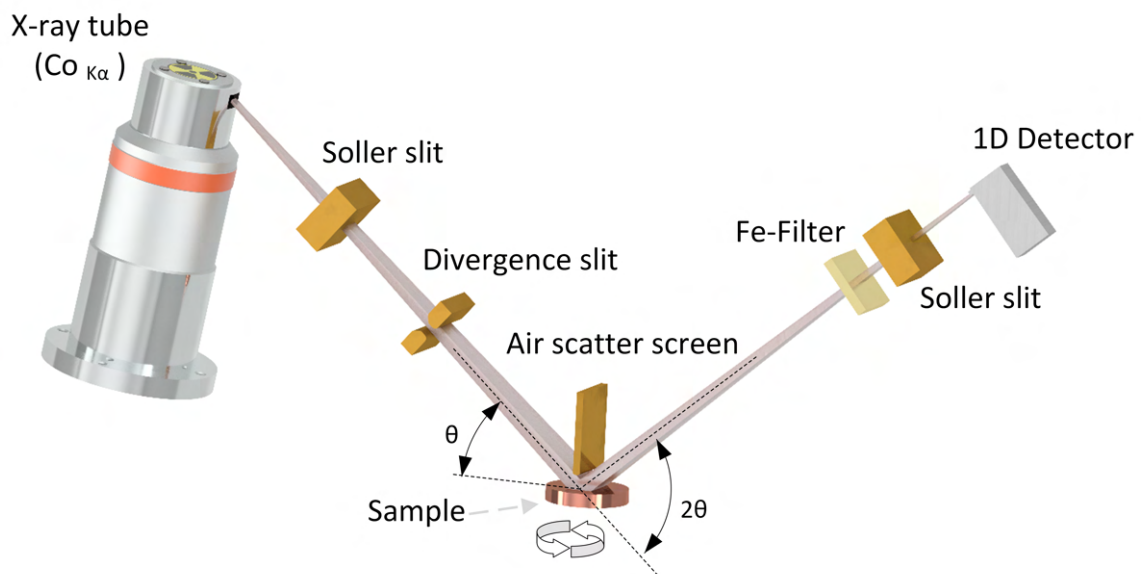
Figure 3.8.: Schematic setup of the XRD Measurements with the Bruker D2 Phaser.

3.7. Magnetic Measurements

To examine the influence of HPT on the Y35-ferrite and the powder composite samples, full loop magnetization curves are measured using a Brockhaus HG 200 hystograph. For this reason, the surfaces of the samples are leveled using sanding. Since the minimum height for measurements is 1.3 mm, two deformed samples are stacked and measured. Compacted powder billets and undeformed Y35 samples fulfill the specifications and are measured as depicted in figure 3.9. The sample is inserted in the surrounding coil with a ⌀ 10 mm and placed between the poles of the electromagnet. After the poles are secured against movement with two eccentric levers, the measurement is performed using the Magexpert software. Artifacts can occur at high fields using this set-up, the initial current is set to 15 A to magnetize the sample and then reduced step-wise, till

an acceptable hysteresis loop, reaching J_s but displaying a minimum image effect, can be measured.
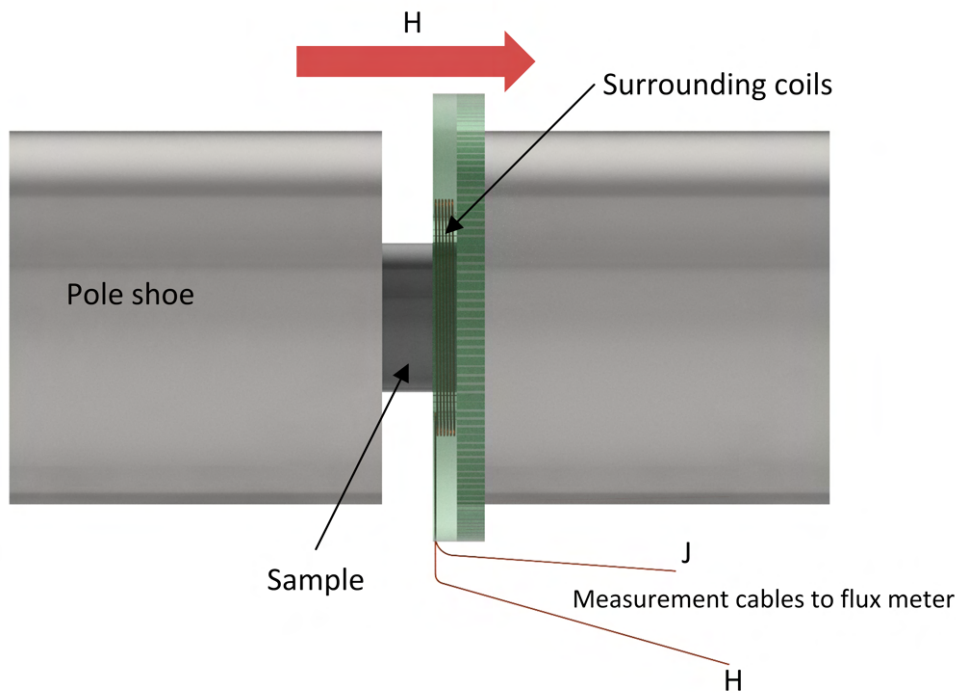
Figure 3.9.: Schematic setup of the magnetic measurement. The magnetization curve is measured with a flux meter and 2 surrounding coils placed around the sample in the air gap. For better centering the polymer holder of the coils are attached to the pole shoe with a concentric ring.

The measured data is processed by a Python script to eliminate any offset. Also, this script is used to extract magnetic parameters, like H_c, J_s, B_r and BH_{max}. In some cases, a relatively flat crossing of the magnetization curve and the magnetic field, H, axis occurred. In these cases, the measured values around 0 are interpolated using a linear function to avoid errors in the correction and calculation caused by fluctuations leading to multiple crossings of the H-axis. The used coder is shown in the appendix A.2.

4. Results

For every class of samples the results of experiments described in chapter 3 are presented with representative micrographs. The results of the magnetic measurements are given in the corresponding tables.

4.1. HPT of Polymers

Figure 4.1 shows the samples of PP, PEEK, PVC, PTFE and POM. Except for PP and POM a deformation for 1 revolution at 1 GPa leads to heavy surface damage. In the PTFE sample, a rupture in the middle of the disc occurred in addition to the lamellar surface damage seen in the PEEK RT sample. The PP sample displayed good deformability at RT at low torque levels, with a relatively smooth surface. PEEK displayed heavy surface damage while POM displayed a similar behavior as PP with some structures, similar looking to shear bands visible at the surface. PVC on the other hand shows a slightly different behavior. Instead of the lamellar surface damage observed at PEEK, small cavities are formed. At elevated temperatures, near T_m, the behavior changed for all polymers. At 100 °C, PP shows a wavy surface with visible structures looking similar to shear bands. As it can be seen in figure 4.1 the increase in temperature has a slight impact on the deformability of PEEK. Also, the formation of voids and cracks within the sample volume is observed.
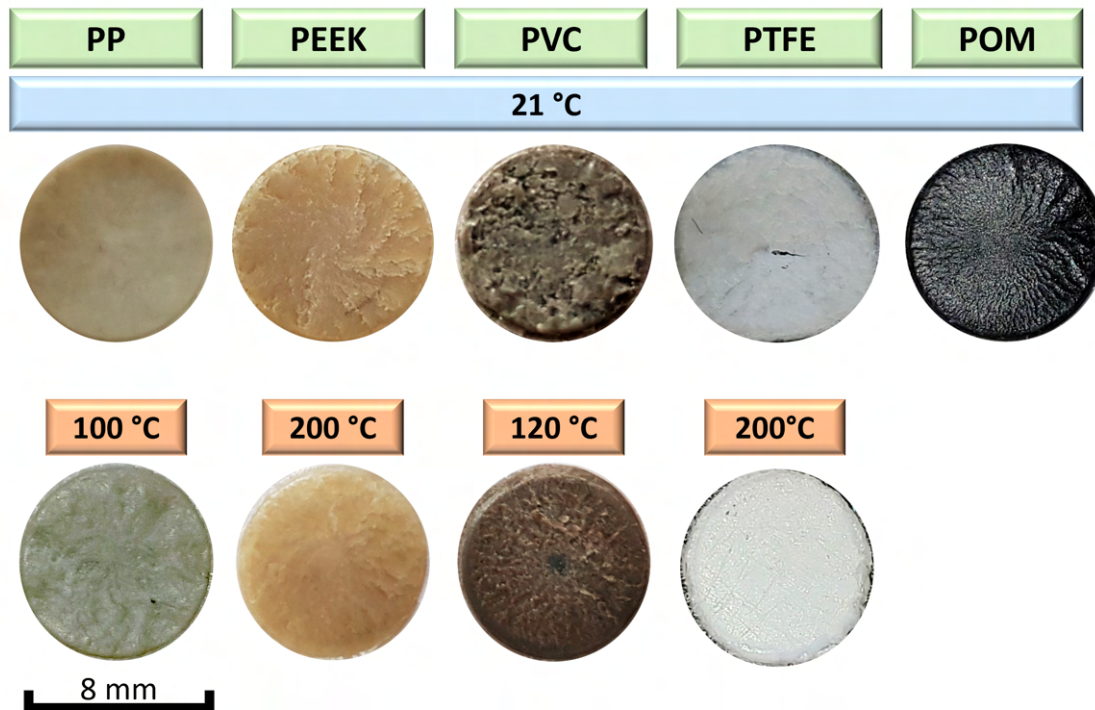
Figure 4.1.: Images of the sample surface of HPT discs made of PP, PEEK, PVC and PTFE, processed at RT and processed near the melting point. At the right: image of the sample surface of the POM HPT disc processed at RT.

A detailed micrograph is given in figure 4.2. The lamellar, pouch-like damaged surface structure can clearly be seen in (a). Further examination reveals cracks and voids in the cross section of the HPT disc (b). The slightly visible pattern under the polarized light used for this image also suggests the presence of smaller defect structures. This is confirmed in by image (c) where several smaller pores can be seen and a crack tip with coalescing lenticular pores is visible. PVC deformed at 120 °C shows good deformability with only small surface defects, compared with PEEK. But exhibits a rather low torque. Similar to PEEK the surface defects on the PVC sample exhibit a lenticular shape. As seen in figure 4.1 some structures similar to shear bands are visible at the surface. POM displayed a similar behavior with a remarkable decrease in visible surface structures at 160 °C.
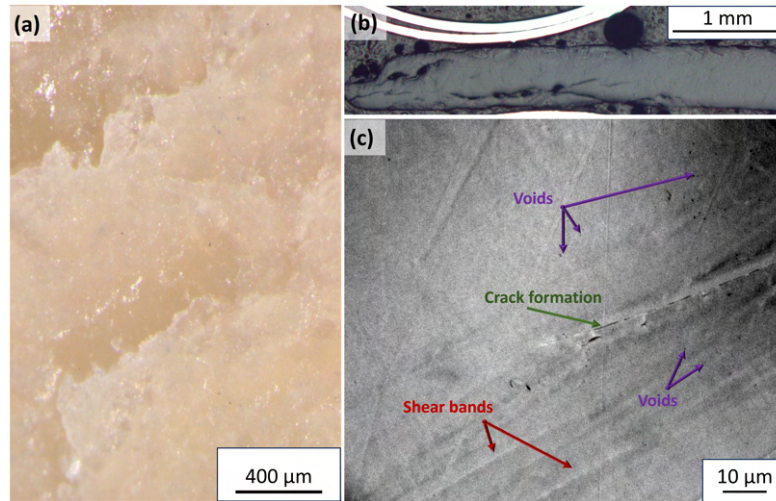
Figure 4.2.: Surface of the PEEK sample deformed at 200 °C (a), radial cross section overview of the PEEK sample deformed at 200 °C (b), void- and crack formation in the sample (c).

As described in chapter 3.1, a PTFE sample made from PTFE sheet material is deformed in preliminary HPT experiments. XRD analysis confirmed its composition of pure PTFE. These samples behaved similarly to the samples cut from extruded virgin PTFE (THOMAPLAST ®) at RT but shows a different behavior in the deformation near T_m. Whilst the virgin PTFE samples displayed torque about 60 to 70 N/mm² during the whole deformation and, in contrast to all other polymer samples, the sample surface looked mostly untouched. The PTFE sample turned out from the sheet material displays a similar torque in the 5th revolution, after strain hardening. A smooth surface without cracks after deformation was accomplished. For PP and PEEK, the amorphization process takes place during HPT. Amorphization is confirmed by XRD and shown in figure 4.3 (a-c) and figure 4.4 (a-c). While for PEEK a complete amorphization is observed, PP shows an increase in orientation along the (200) plane and a higher remaining crystallinity at elevated temperatures. XRD patterns for PP are indexed using data from Clark [102] and De Rosa et al. [103]. For PEEK, crystallographic data from Fratini et al. [104] is used.
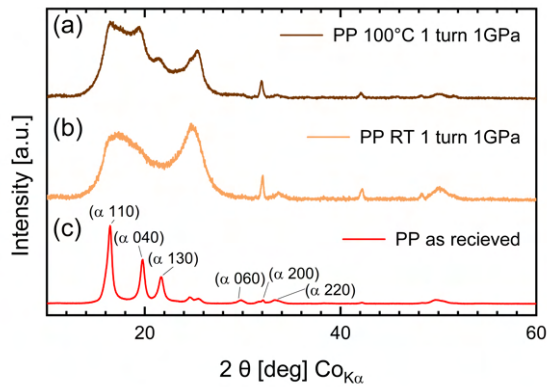
Figure 4.3.: XRD of PP deformed for 1 revolution at 100 °C (a), deformed for 1 revolution at RT (b) and pristine PP (c).
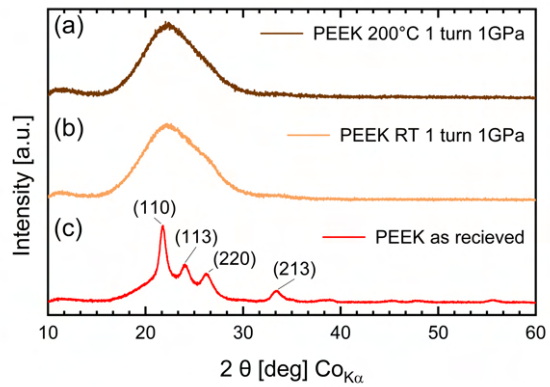
Figure 4.4.: XRD of PEEK deformed for 1 revolution at 200 °C (a), deformed for 1 revolution at RT (b) and pristine PEEK (c).

4.2. Metal-Polymer Composites by Multi-Sector Disk HPT

In the first experiments utilizing ¼ segments (Cu-PEEK and Cu-PVC), most of the polymer is pressed out of the anvil cavity. The remaining polymer in the sample displayed no co-deformation and weak adhesive interfaces. A slight increase of polymer fraction in the deformed sample is achieved for samples with an additional constraining Cu-ring (Cu-PEEK and Cu-PVC). But no co-deformation is observed. In contrast to previous samples, the Cu-POM composites show co-deformation in 2 different configurations. The first sample consisting out of ¼ segments pressed in a Cu-ring was deformed for 1 revolution at 5 GPa and RT. In figure 4.5 (a) the microstructure of this sample is depicted. A further optimization is achieved through the increase of segments to ⅛ and in amount of revolutions. For the sample deformed for 3 revolutions, a layered composite structure is observed and depicted in figure 4.5 (b). One persistent drawback is the low adhesive bonding between the metal and the polymer leading to a clearly visible delamination.
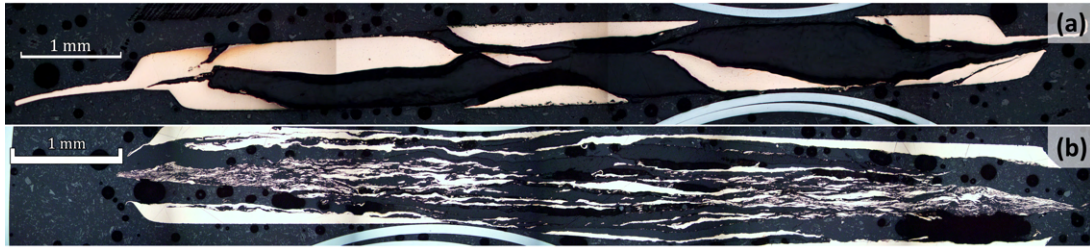
Figure 4.5.: Micrographs of Cu-POM composites: ¼ segments deformed at RT and 5 GPa for 1 revolution (a) and ⅛ segments deformed at RT and 5 GPa for 3 revolutions (b).

4.3. HPT of Magnetic Materials

4.3.1. HPT of Y35 M-type Hexaferrite

As described in chapter 2.2.1 mechanisms of deformation in ceramics are rather intricate processes. An interesting behavior is displayed by the commercial Y35 magnets during HPT. Despite observed stick-slip during HPT, processed samples show some affected regions. A deformation at 2.5 GPa and RT for 1 revolution results in a significant change of microstructure. Grains are fractured into particles, rearranged and refined. The whole sample cross section displays a nonuniform microstructure containing regions with fine rearranged particles besides regions with big particles, as shown in figure 4.6 (a) and (d). The white dots in the pictures are fused silica relicts. Elongated small particles suggest the existence of plastic deformation. However, thin lines through these small particles show that the main forming process is the compaction of small particles into these elongated structures. The refined areas become more pronounced with higher pressure and more rotations. This correlation is depicted in figure 4.6 (a - f). A slight shift of peak positions in the deformed samples also indicates the existence of lattice strain, although the exact behavior is not reproducible like shown in figure 4.7 (a-c). Also, a change in preferred orientation is observed by the XRD analysis, since the maximum intensity shifts from (8) to (107) and (114) respectively. All samples also exhibit parallel angular microcracks through the particles, visible in figure 4.6.
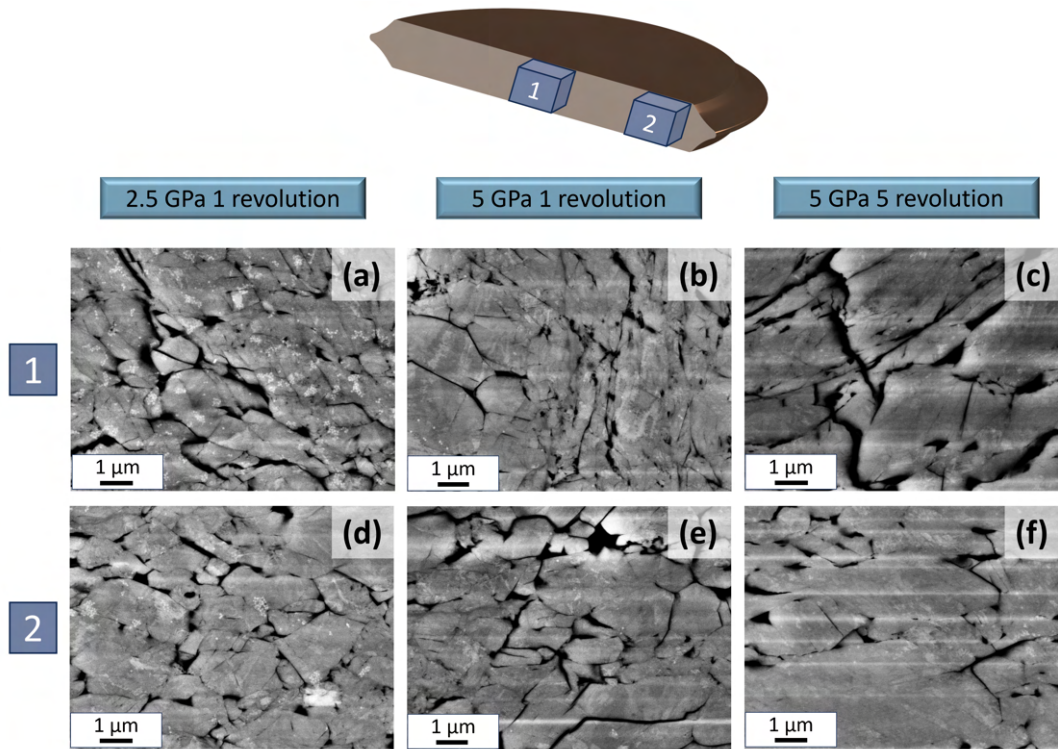
Figure 4.6.: SEM micrographs of Y35 deformed by HPT : for 1 revolution at 2.5 GPa in the center of the sample (a), for 1 revolution at 5 GPa in the center of the sample (b), for 5 revolutions at 5 GPa in the center of the sample (c), for 1 revolution at 2.5 GPa at the outer radius of the sample (d), for 1 revolution at 5 GPa at the outer radius of the sample (e) and 5 revolutions at 5 GPa at the outer radius of the sample (f).
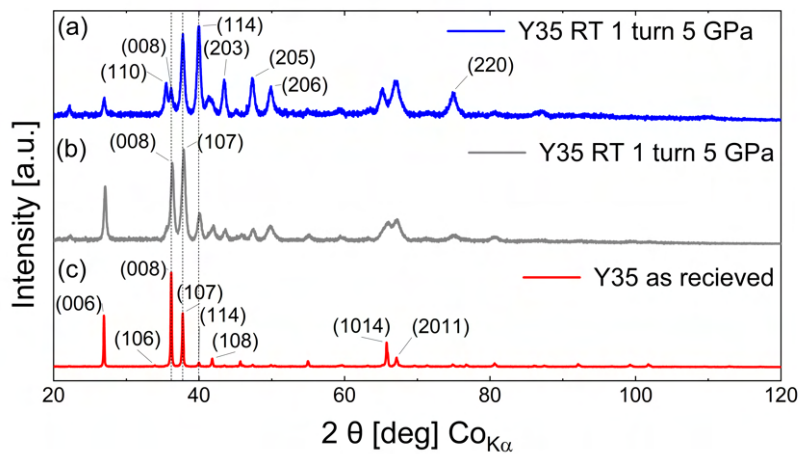
Figure 4.7.: XRD pattern of Y35 deformed by HPT for 5 revolutions at 5 GPa (a-b) and the pristine commercial Y35-ferrite. Indexed using data from Obradors et al. [76] and Rahman et al. [105].

SEM micrographs obtained after compression in the HPT tool showed that the angular microcracks already form at this step. Also, a reduced porosity is observed

in the HPT processed and compressed state. Figure 4.8 shows the microstructure of the pristine magnets (a) compared to the microstructure resulting from uniaxial compression with 5 GPa (b). Images are taken in the center of the samples. After HPT processing, Y35 samples incline to fragment spontaneously during cutting, grinding, or even through slight vibrations.
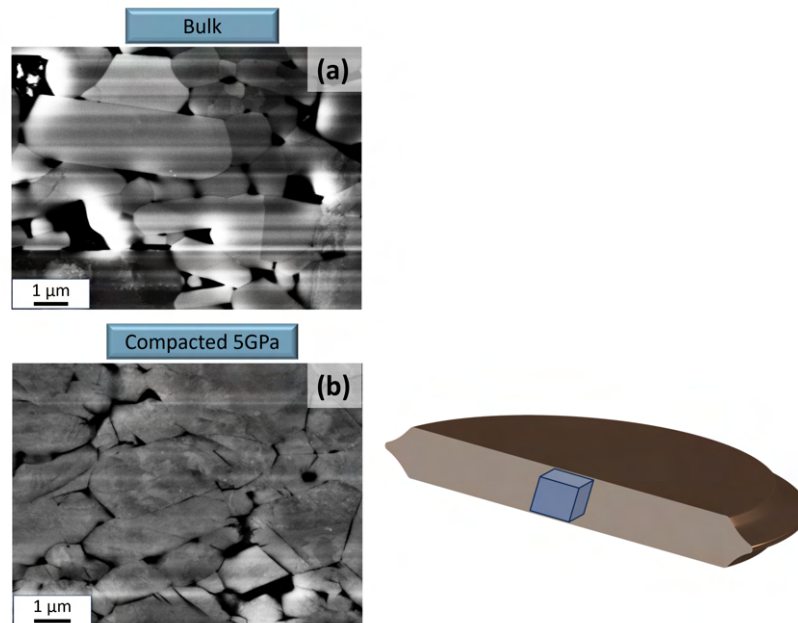
Figure 4.8.: SEM micrographs of pristine Y35 (a) and Y35 after uniaxial compression with 5 GPa (b).

Magnetic measurements reveal an increase of the magnetic hardness, from $\kappa = 1.63$ to 2.99 for samples deformed for 1 revolution. But a sharp reduction in BH_{max}, M_s, H_c, and B_r is observed. An overview of measured values is given in table 4.1 and figure 4.9 (a-e). Figure 4.9 (b-e) describes the 2nd quadrant of the single measured magnetization curves. In summary, HPT processing results in smaller magnetization curves with a less rectangular shape with a significant variation of measured magnetic parameters even for samples deformed with the same process parameters. This can be seen in figure 4.9 (a) where the samples deformed for 0.25 revolutions yield a rather high discrepancy.
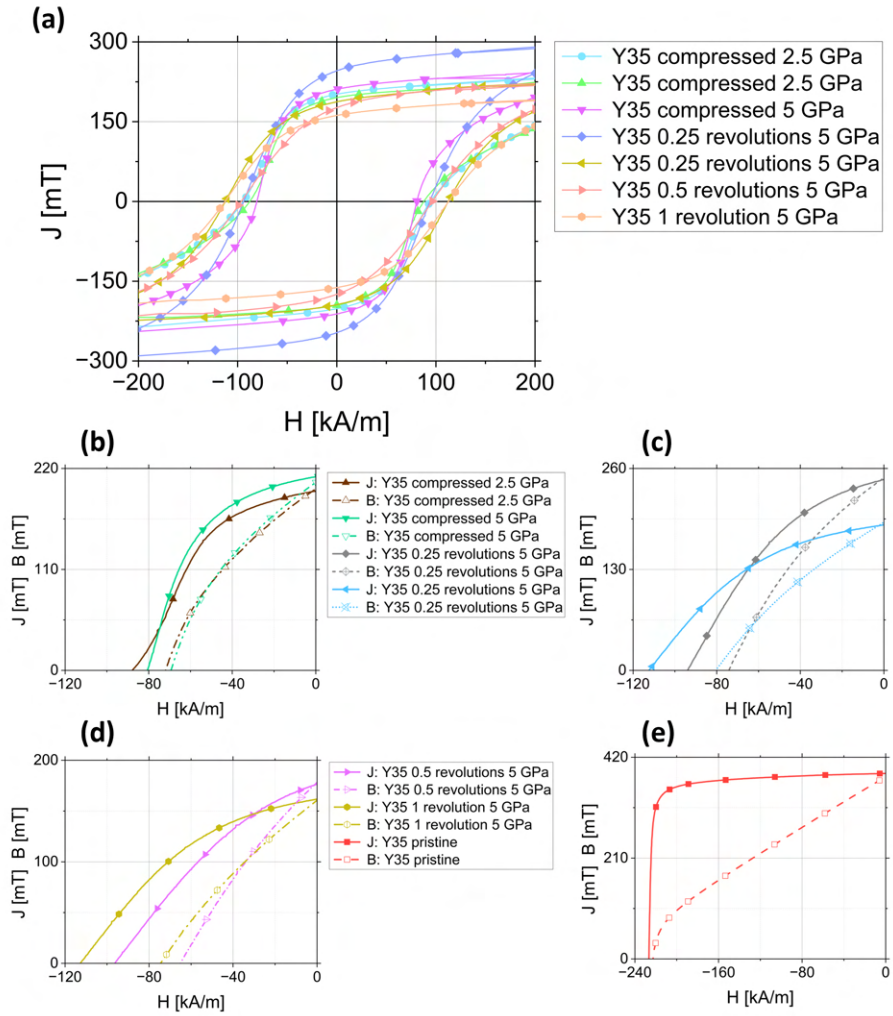
Figure 4.9.: Magnetization curves of Y35 deformed by HPT: overview J-H curves for uni axial pressed to deformed for 1 revolution (a), 2nd of the magnetization curves for pressed samples (b), 2nd of the magnetization curves for deformed samples 0.25 revolutions (b), 0.5 revolutions (c), 1 revolution (d), and 2nd of the magnetization curves for the pristine material (e).

Table 4.1.: Magnetic parameters of the deformed Y35 Hexaferrites.

Deformed Y35	$H_{cJ}[kA/m]$	$H_{cB}[kA/m]$	$B_r[mT]$	$J_s[mT]$	$BH_{max}[kJ/m^3]$
Pristine (X-Y corrected raw data)	226.7	222.8	386.5	405.7	27.9
Pristine (Interpolation)	226.7	222.9	380.3	405.5	26.9
Pressed 2.5 Gpa (X-Y corrected raw data)	91.1	69.6	198.4	269.75	4.9
Pressed 2.5 Gpa (Interpolation)	94.38	71.9	199.5	285.1	4.9
Pressed 5 Gpa (X-Y corrected raw data)	80.6	69.4	211.3	296.1	5.3
Pressed 5 Gpa (Interpolation)	80.87	69.3	204.9	295.8	5.0
0.25 revolutions 5GPa (X-Y corrected raw data)	103.2	77.3	218.5	249.28	5.4
0.25 revolutions 5GPa (Interpolation)	94.071	74.2	248	333.2	6.1
0.5 revolutions 5GPa (X-Y corrected raw data)	96.3	65.1	175.5	263.6	3.3
0.5 revolutions 5GPa (Interpolation)	96.55	65.0	177.6	265.0	3.4
1 revolution 5GPa (X-Y corrected raw data)	112.7	74.5	161.8	222.1	3.6
1 revolution 5GPa (Interpolation)	112.7	74.6	159.9	221.9	3.5

Despite no shift in peak position is observed in XRD, the structural evolution of samples deformed at 500 °C shows no significant difference to experiments at RT. Associated XRD patterns are shown in figure 4.10.
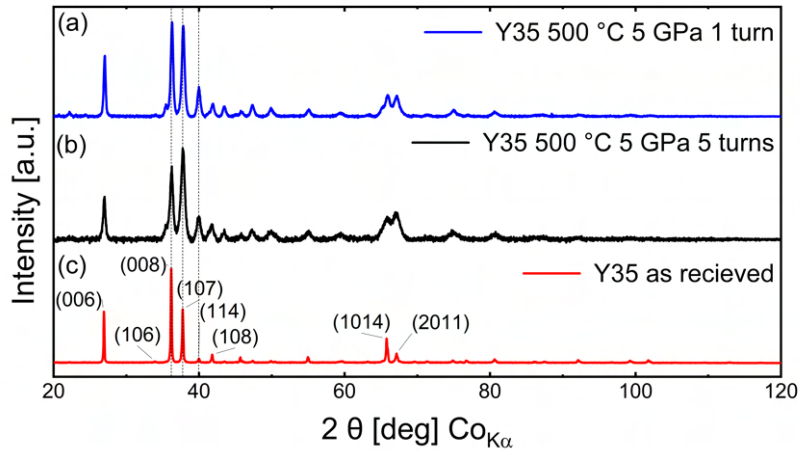
Figure 4.10.: XRD pattern of Y35 deformed by HPT at 5 GPa and 500 °C for 1 revolution (a), 5 revolutions (b) and the pristine commercial Y35-ferrite. Indexed using data from Obradors et al. [76] and Rahman et al. [105].

Y35 samples deformed at higher temperatures exhibit a conical shape, as shown in figure 4.11 accompanied by a deformation of the anvil. A insufficient deformation behavior is expected, thus, no further experiments have been conducted.
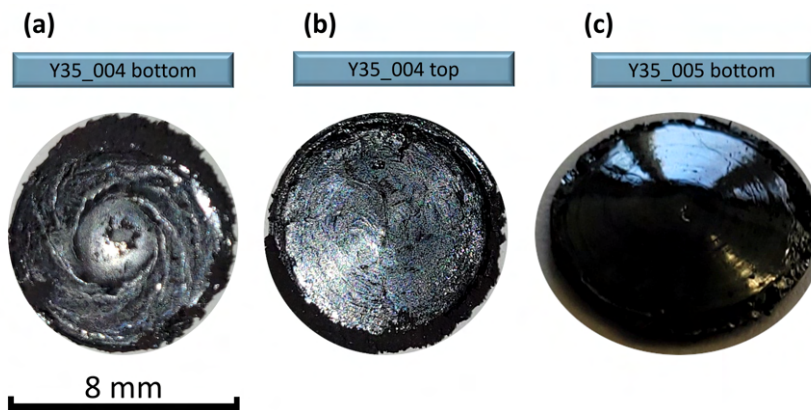
Figure 4.11.: Y35 samples deformed by HPT, at 5 GPa and 500 °C for 5 revolutions (a-b), 1 revolution (c).

4.3.2. HPT of AlNiCo Alloys

The microstructure of all 3 AlNiCo grades is investigated preliminary to the deformation. Figure 4.12 (a-c) shows the microstructure of AlNiCo 8, AlNiCo 5 and AlNiCo 3 respectively. No etching is applied to the polished samples. In AlNiCo 3 black structures can be seen on the polished sample with the naked eye, suggesting some degree of porosity due to casting defects. Since small round or elongated objects visible in microscopic images likely are nonmetallic inclusions [106, 107], further studies are necessary to distinguish between precipitates and pores in this micrograph. The bright regions indicate the presence of a 3rd phase. In the AlNiCo 5 alloy the existence of non-metallic inclusions is also observed. AlNiCo 8 displays a more complex microstructure with elongated nonmetallic inclusions, small areas of a 3rd phase and small round inclusions.
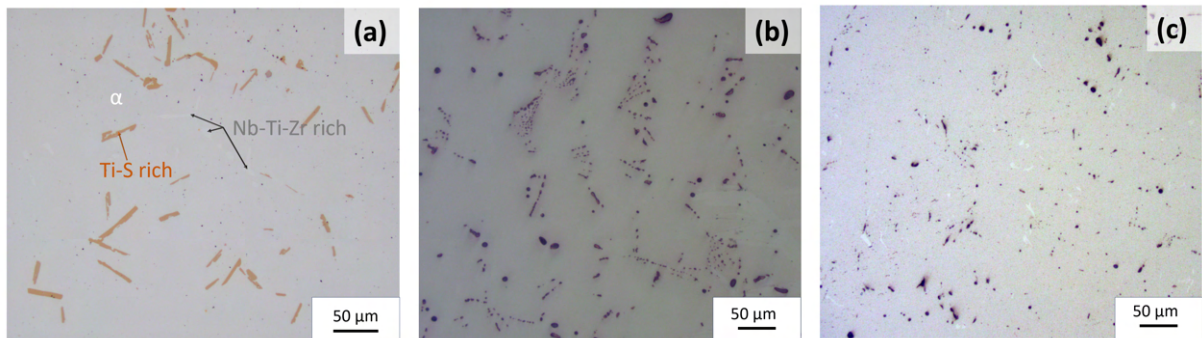
Figure 4.12.: Optical micrographs of the pristine AlNiCo magnets, AlNiCo 8 (a), AlNiCo 5 (b) and AlNiCo 3 (c).

Further investigation with BSE microscopy reveals the nano-structured microstructure of the AlNiCo alloys. In figure 4.13 (a-f) the microstructure of AlNiCo 3, AlNiCo 5 and AlNiCo 8 is shown respectively. Whilst (a-c) shows overview images, affirming the observations of the light microscopy described previously, the images (d-f) show the detailed structure. The marbled pattern originates in the arrangement of the darker α_2 precipitates in the α_1 matrix. One intriguing observation is the decrease in size and the increase in orientation of the α_2 precipitates, from AlNiCo 3 to AlNiCo 8. The 3rd phase observed in the light microscopy image of AlNiCo 8 is found to form at grain boundaries and shows a multi-phase configuration.
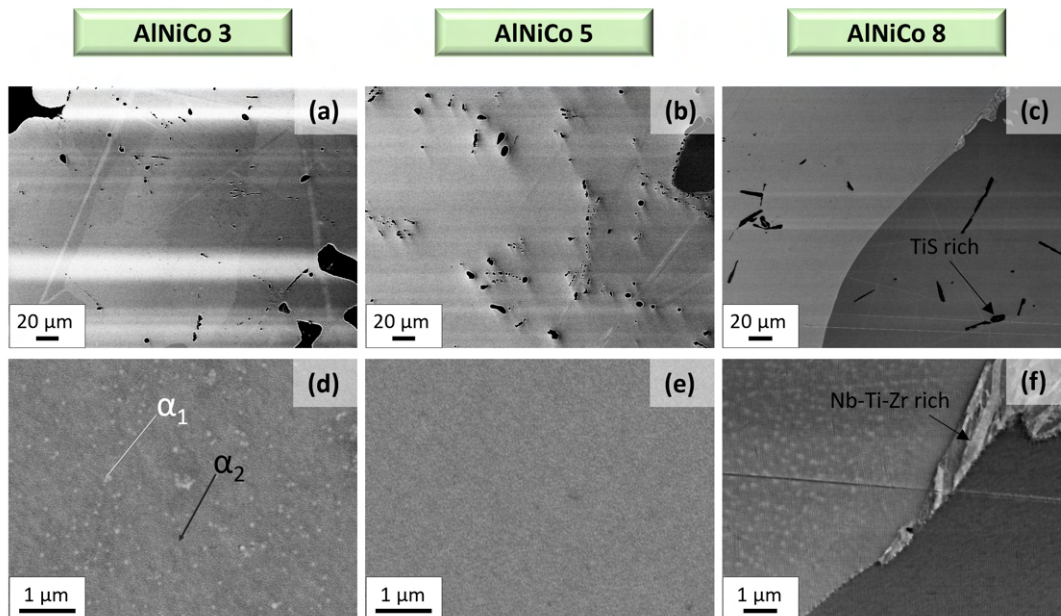
Figure 4.13.: BSE micrographs of the pristine AlNiCo magnets, AlNiCo 3 (a and d) , AlNiCo 5 (b and e) and AlNiCo 8 (c and f).

After the deformation microstructural analyses are carried out by SEM. A columnar refined microstructure with broken and deformed inclusions is observed for all AlNiCo grades. Figure 4.14 (a-i) shows the pristine microstructure compared to the refined. In AlNiCo 5, (e), a fracture, growing from a deformed inclusion is seen. Also in AlNiCo 8 cracks are seen at the interface between the 3rd phase along the old grain boundaries. Remarkable is the change in orientation and form of the precipitates. A similar microstructure is observed by Zhang et al. [108] in AlNiCo alloys deformed by hotrolling. Whole grains get smaller, the precipitations, formed by spinodal decomposition get tilted (creating a seemingly coarsening)and less defined. This especially can be seen in the comparison between figure 4.14 (g) and (i). During XRD, a change in the peak sequence is observed. After deformation, all 3 AlNiCo grades show the same peaks. In contrast to their pristine state, where the patterns are distinct for each grade. In the case of AlNiCo 8, the α_2 present in the pristine pattern can not be resolved in the deformed state. XRD patterns of AlNiCo alloys are presented in appendix D.
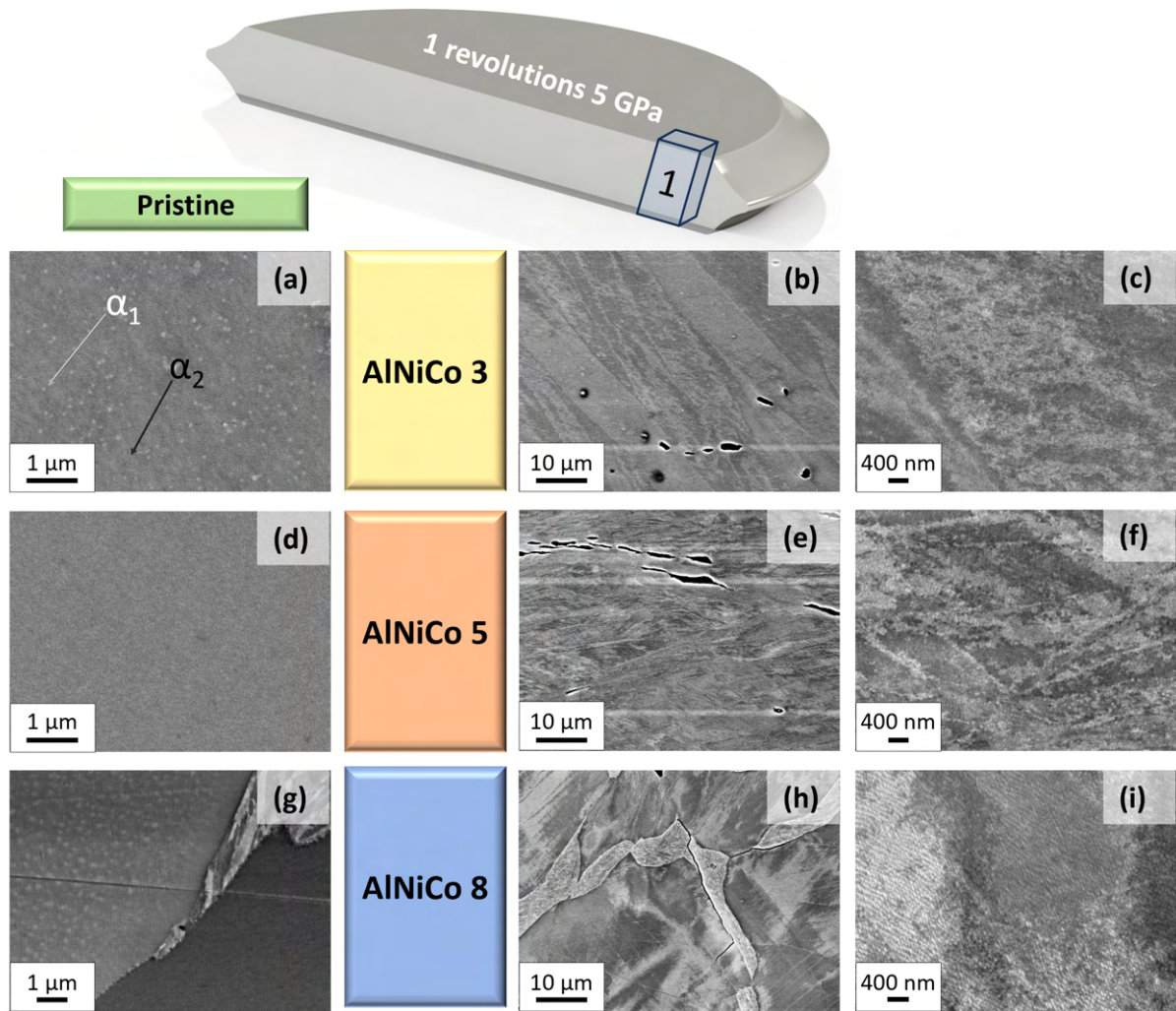
Figure 4.14.: BSE micrographs of deformed AlNiCo magnets. The pristine microstructure is shown in the left column as reference. AlNiCo 3 (a–c), AlNiCo 5 (d–f) and AlNiCo 8 (g–i).

Magnetic measurements reveal a similar trend as for the HPT processed Y35-ferrites. Figure 4.15 (a-c) shows the measured magnetization curves of pristine and deformed AlNiCo alloys. The κ increases about 0.2 for AlNiCo 5 and AlNiCo 8 whereas the BH_{max} drops to values between $0.60\,kJ/m^3$ and $2.97\,kJ/m^3$. The measured magnetization curves get smaller and tilted. Measured values are given in table 4.2 and table 4.3.
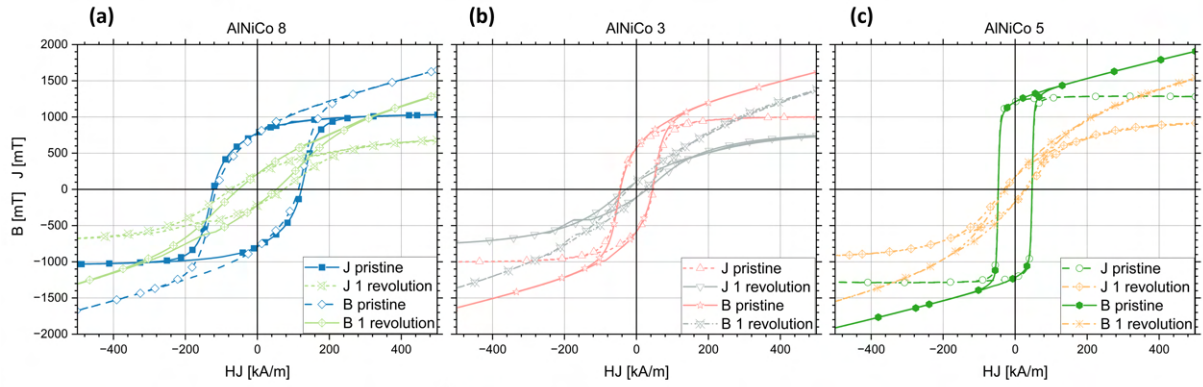
Figure 4.15.: Magnetization curves of AlNiCo magnets, AlNiCo 8 (a), AlNiCo 3 (b) and AlNiCo 5 (c).

Table 4.2.: Magnetic parameters of pristine AlNiCo.

Pristine	H_{cB}[kA/m]	H_{cJ}[kA/m]	B_r[mT]	J_s[mT]	BH_{max}[kJ/m³]
AlNiCo 3 (X-Y corrected raw data)	44.5	46.8	576.4	1002.5	8.7
AlNiCo 3 (Interpolation)	44.5	46.8	570.9	1000.6	8.6
AlNiCo 5 (X-Y corrected raw data)	47.0	47.2	1212.8	1289.9	36.5
AlNiCo 5 (Interpolation)	47.1	47.3	1208.7	1288.9	36.3
AlNiCo 8 (X-Y corrected raw data)	114.2	122.3	785.0	1041.1	31.5
AlNiCo 8 (Interpolation)	114.3	122.1	770.3	1034.5	30.6

Table 4.3.: Magnetic parameters of deformed AlNiCo.

Deformed	H_{cB}[kA/m]	H_{cJ}[kA/m]	B_r[mT]	J_s[mT]	BH_{max}[kJ/m³]
AlNiCo 3 (X-Y corrected raw data)	22.2	29.4	106.8	775.8	0.6
AlNiCo 3 (Interpolation)	22.3	29.2	105.9	761.0	0.6
AlNiCo 5 (X-Y corrected raw data)	26.1	31.5	172.6	929.2	1.2
AlNiCo 5 (Interpolation)	26.0	31.5	172.2	924.8	1.2
AlNiCo 8 (X-Y corrected raw data)	53.0	72.9	216.0	713.6	3.0
AlNiCo 8 (Interpolation)	52.8	73.0	213.7	700.6	2.9

4.4. Metal-Y35-Hexaferrite Composites by Multi-Sector Disk HPT

For each material combination, a microscopic overview is given in figure 4.16 (a-d). In general, plastic deformation is mainly limited to the metal. The ceramic builds big islands in the sample, prone to delamination, if isolated at the sample surface. Also visible is the influence of difference in strength and hardness of the materials on the co-deformation. Composites containing Cu (a) or Fe (b) display more interconnected ceramic regions. The Cr composite (c) displays more detached ceramic islands in the metal matrix. No sample shows a sufficient layered microstructure. In figure 4.16 (d), a Cu-Fe sample deformed with the same parameters is shown for reference.
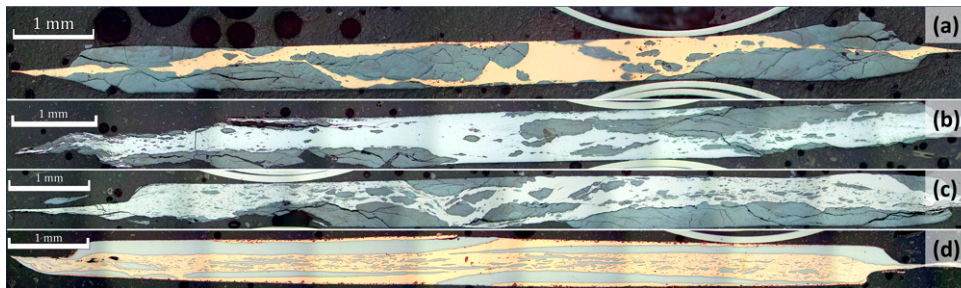
Figure 4.16.: Microgaphs of HPT samples fabricated by the multi-sector disk approach using ¼ segments: a) Y35-Cu composite, b) Y35-Cr composite, c) Y35-Fe composite and d) Fe-Cu Composite.

In Figure 4.17 (a-d), resulting microstructures of the deformation with sheet metal are shown. No positive effect of reducing the ductile metal fraction is observed.
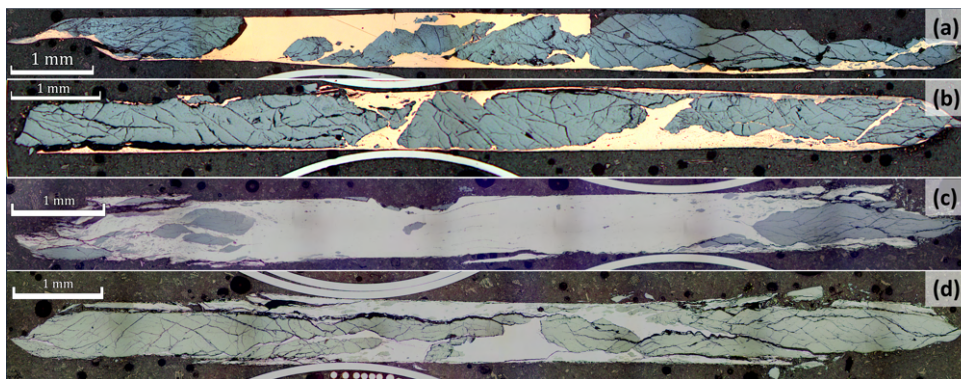
Figure 4.17.: Microgaphs of HPT samples fabricated by the multi-sector disk approach, using ⅛ segments and sheet metal inlays: a) Y35-Cu composite using 0.3 mm sheet material, b) Y35-Cu composite using 0.1 mm sheet material, c) Y35-Fe composite using 0.54 mm sheet material and d) Y35-Fe composite using 0.15 mm sheet material.

4.5. Polymer-Y35-Hexaferrite Composites by Multi-Sector Disk HPT

Figure 4.18 (a-d) shows micrographs of the samples Y35-PTFE s 001, Y35-POM R 002 and Y35-POM s 001 respectively. HPT processing of Y35-PTFE composites result in a fragile HPT sample. No bonding is achieved between PTFE and the ceramic phase. Image a) shows half of an HPT disc fractured after cutting along the polymer-ceramic interface. The majority of PTFE is lost during the HPT process. Remaining PTFE functions as interface causing material failure. The Y35-POM sample shows a slightly different behavior. Since the deformability of POM is better than PTFE during HPT deformation at RT, POM fills out gaps and flows around ceramic islands. Still bonding of the polymer and the ceramic phase is not sufficient. Although the applied PDA improves stability, still a satisfactory joint does not develop. Minimizing the fraction of the polymer does not improve structural stability, similar to the metal-ceramic composites.
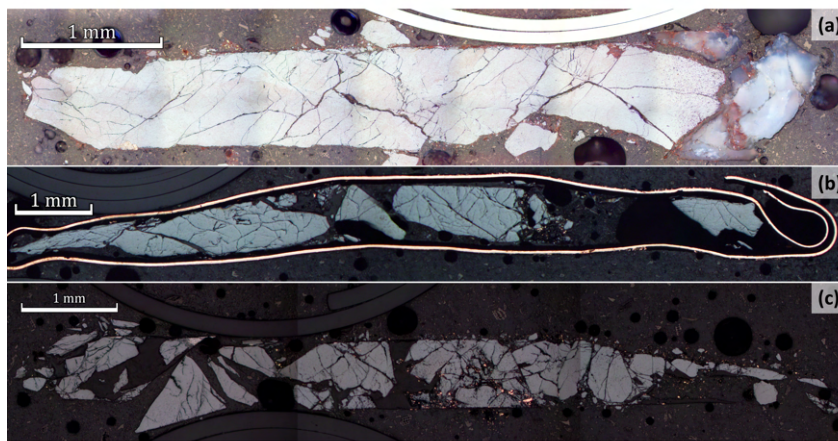
Figure 4.18.: Optical micrograph of the deformed polymer-hexaferrite composites via multi-sector disk HPT: Y35-PTFE sample with PTFE sheet inlays a); Y35-POM ⅛ pieces pressed in the Cu ring, the Cu lining in the picture is added to ensure stability during sample preparation b); Y35-POM with POM sheet inlay (c).

4.6. SrFe$_{12}$O$_{19}$ Powder Composites by HPT

Figure 4.19 (a-c) shows micrographs of compacted SrFe$_{12}$O$_{19}$-M samples, where M is the metal. All three combinations show a sufficiently distributed two-phase microstructure with some remaining porosity. Also remarkable is the size of the formed single-phase regions. Whilst Fe and Cu form rather coarse structures, the structure of the compacted Cr sample is comparatively fine.
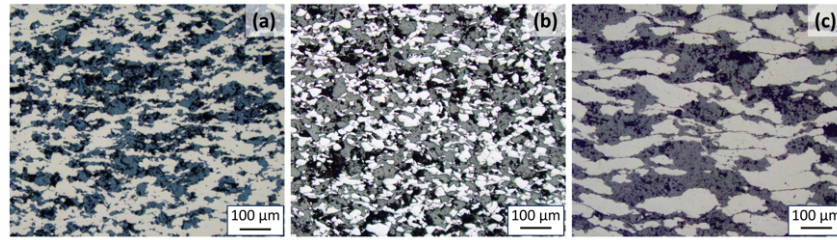
Figure 4.19.: Optical micrograph of powder composites compacted at 2.5 GPa: SrFe$_{12}$O$_{19}$ - Cu (a), SrFe$_{12}$O$_{19}$ - Cr (b) and SrFe$_{12}$O$_{19}$ - Fe (c).

For the SrFe$_{12}$O$_{19}$-PTFE sample a successful compaction also is achieved by the same method. As seen in figure 4.20 PTFE is distributed between the SrFe$_{12}$O$_{19}$ particles, forming thin films along particle surfaces in a net-like manner. Also, large PTFE islands are observed. All compacted samples show some porosity.
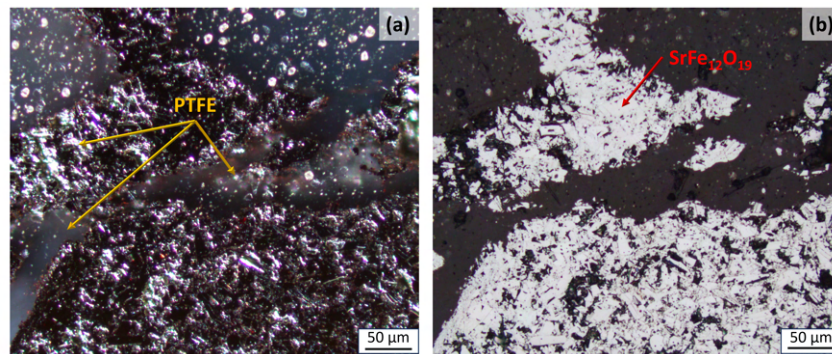
Figure 4.20.: Optical micrograph of the compacted SrFe$_{12}$O$_{19}$ - PTFE powder composite: polarized light microscopy (a) bright field microscopy (b).

After deformation for 5 revolutions at 5 GPa the four samples show various degrees of refinement. Optical micrographs of the composites are given in figure 4.21 (a-d) respectively. The Cu composite displays the best stability and a uniform microstructure over the sample thickness. A clearly visible gradient in phase refinement in the radial direction is observed. In the sample containing Fe and Cr an gradient is also found in the axial direction. Also, surface chipping and cracks are seen with increasing amounts to the outer radial position. Cr composites show a stronger phase refinement as well as a higher amount of chipping. In general, the Cr composite is fragile and prone to fracture. Remarkable are the light gray areas on the sample surface at the outer radius. These regions show fine lamellar structures of Cr and SrFe$_{12}$O$_{19}$. The polymer composite, containing PTFE shows a microstructure similar to the compacted sample, with some refinement at the outer radius. Polymer composite samples are prone to delamination and fracture.
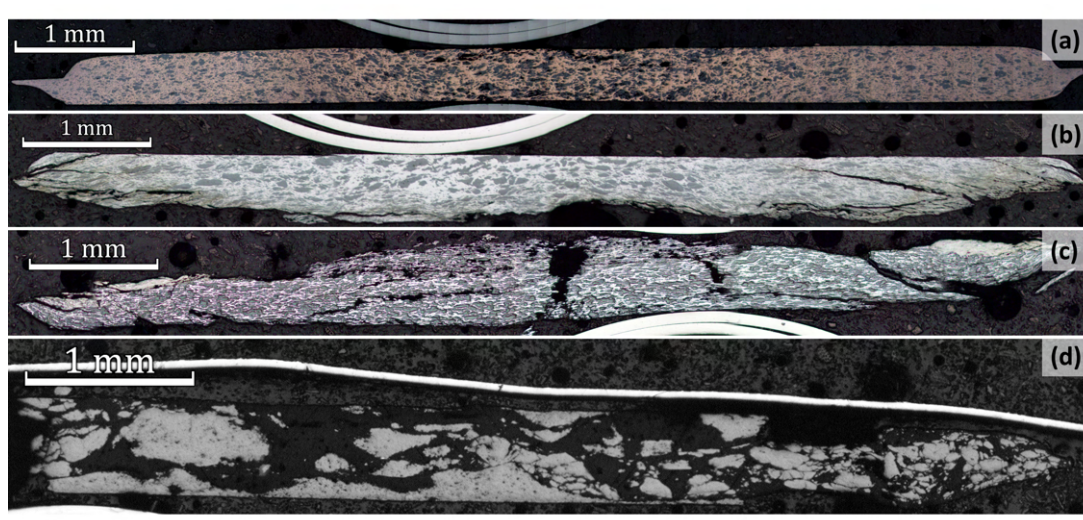
Figure 4.21.: Deformed powder composites, 5 revolutions at $5\,\mathrm{GPa}$: $SrFe_{12}O_{19}$-Cu (a), $SrFe_{12}O_{19}$-Fe (b), $SrFe_{12}O_{19}$-Cr (c) and $SrFe_{12}O_{19}$-PTFE (d).

Further characterization of the microstructure using SEM reveals the difference in shape and size of ceramic islands in the metal matrix. SEM images of the SrFeO-Fe sample are shown in figure 4.22 (a, d and g) respectively. Fe shows rather thick wavy Fe bands between large blocks of $SrFe_{12}O_{19}$. In these bands smaller ceramic islands are visible. The elongated form of the smaller ceramic regions suggests some degree of co-deformation. SEM images of the SrFeO-Cr sample are shown in figure 4.22 (b, e, and h) respectively. Similar to the SrFeO-Fe composite, the SrFeO-Cr composite displays elongated but more uniform structures. In general, the thickness of individual regions is smaller than in the SrFeO-Fe composite, and also fine Cr-linings are seen in the SrFeO regions. SEM images of the SrFeO-Cu sample are shown in figure 4.22 (c,f and I).In contrast to the Cr and Fe composites the SrFeO-Cu sample shows a relatively uniform microstructure with fine dispersed SrFeO particles and some larger ceramic islands.
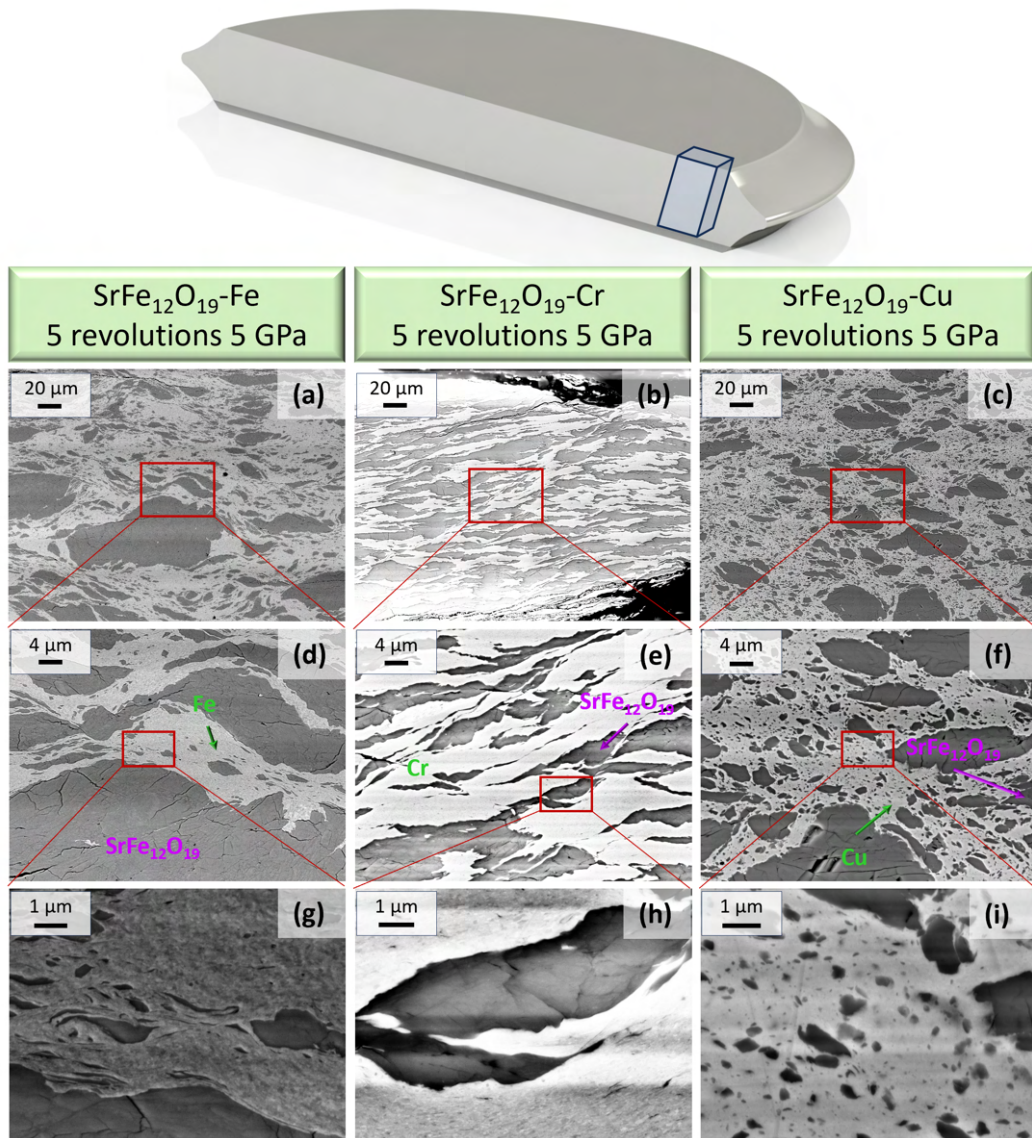
Figure 4.22.: BSE image at the outer radius of SrFe$_{12}$O$_{19}$-M powder composites. Overview: SrFe$_{12}$O$_{19}$-Fe (a), SrFe$_{12}$O$_{19}$-Cr (b), SrFe$_{12}$O$_{19}$-Cu (c). Detailed micrograph: SrFe$_{12}$O$_{19}$-Fe (d), SrFe$_{12}$O$_{19}$-Cr (e), SrFe$_{12}$O$_{19}$-Cu (f), ceramic particles in metal matrix SrFe$_{12}$O$_{19}$-Fe (g), ceramic particles in metal matrix SrFe$_{12}$O$_{19}$-Cr (h), ceramic particles in metal matrix SrFe$_{12}$O$_{19}$-Cu (i).

For SrFeO-PTFE samples microstructural investigation is only conducted using light microscopy. As seen in figure 4.23, deformation leads to a reduction of the PTFE content between the SrFeO particles. This trend is accompanied by a decrease in stability. Only limited refinement of the microstructure is observed.
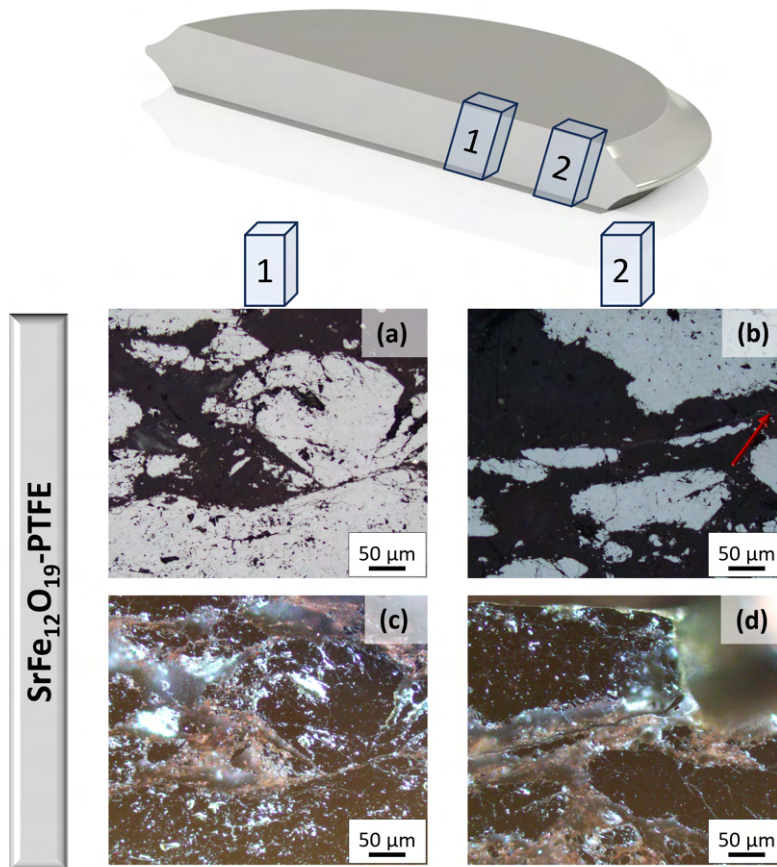
Figure 4.23.: Optical micrographs of the PTFE powder composite at the radial positions of 1.5 mm and 3.5 mm: bright field microscopy (a- b) and polarized light microscopy (c-d). The red arrow marks the location of (d).

For the SrFeO-Fe composite, no valid magnetization curves are measured. Magnetization curves of SrFeO-Cu, SrFeO-Cr and SrFeO-PTFE are shown in figure 4.24 (a-c) respectively. For the Cu and Cr composites, the deformation leads to increasing H_c and decreasing B_r values. On the other hand, H_c and B_r increase for the PTFE composite. For the SrFeO-Cu and SrFeO-PTFE samples BH_{max} is slightly increased by deformation but decreases for SrFeO-Cr. The maximum BH_{max} of the composites is displayed by $SrFe_{12}O_{19}$-PTFE. Magnetization curves of $SrFe_{12}O_{19}$-Cu and $SrFe_{12}O_{19}$-Cr are rather tilted and narrow. Measured values are given in table 4.4 and 4.5. Displacements of the magnetization curves are not reproducible. Therefore, these displacements can not be used as indication of exchange coupling.
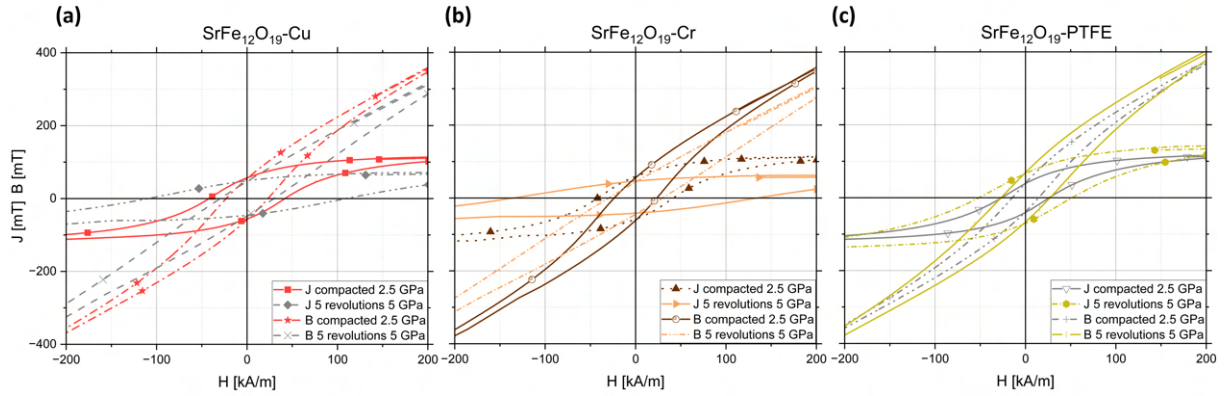
Figure 4.24.: Magnetization curves of powder composites: $SrFe_{12}O_{19}$-Cu (a), $SrFe_{12}O_{19}$-Cr (b) and $SrFe_{12}O_{19}$-PTFE (c).

Table 4.4.: Magnetic parameters of Compacted Powder Composites.

Compacted Powder	$H_{cB}[kA/m]$	$H_{cJ}[kA/m]$	$B_r[mT]$	$J_s[mT]$	$BH_{max}[kJ/m^3]$
$SrFe_{12}O_{19}$-PTFE (X-Y corrected raw data)	22.9	41.6	57.1	140.5	0.34
$SrFe_{12}O_{19}$-PTFE (Interpolation)	14.5	26.5	40.2	139.0	0.2
$SrFe_{12}O_{19}$-Cr (X-Y corrected raw data)	23.7	41.7	58.70	135.0	0.4
$SrFe_{12}O_{19}$-Cr (Interpolation)	23.5	41.8	55.7	136.0	0.4
$SrFe_{12}O_{19}$-Cu (X-Y corrected raw data)	23.2	41.9	56.3	132.7	0.3
$SrFe_{12}O_{19}$-Cu (Interpolation)	23.2	42.1	54.5	133.6	0.3

Table 4.5.: Magnetic parameters of Deformed Powder Composites.

Deformed Powder Composites	$H_{cB}[kA/m]$	$H_{cJ}[kA/m]$	$B_r[mT]$	$J_s[mT]$	$BH_{max}[kJ/m^3]$
$SrFe_{12}O_{19}$-PTFE (X-Y corrected raw data)	27.1	51.8	67.8	165.9	0.5
$SrFe_{12}O_{19}$-PTFE (Interpolation)	27.2	51.51	68.7	156.1	0.5
$SrFe_{12}O_{19}$-Cr (X-Y corrected raw data)	29.7	135.0	44.1	59.8	0.3
$SrFe_{12}O_{19}$-Cr (Interpolation)	30.5	67.4	43.3	63.8	0.3
$SrFe_{12}O_{19}$-Cu (X-Y corrected raw data)	29.7	109.2	47.5	74.3	0.4
$SrFe_{12}O_{19}$-Cu (Interpolation)	29.7	109.5	48.0	77.4	0.4

63

4.7. Annealing of Y35 Hexaferrites

Optical micrographs and determined porosity, for the annealing experiments up to 700 °C are shown in figure 4.25 and table 4.6. Analyzing the microstructure of annealed samples, an increase in relative density (ρ_{rel}) of roughly 2 % is observed for the annealing at 700 °C. XRD analysis reveals no additional phases or significant changes in relative intensities. On the other hand a slight shift to higher angles with increasing temperatures is observed. The $(0\,0\,8)$ peak shifts from 36.177° for the pristine ferrite to 36.318° for the annealed ferrite at 1100 °C.
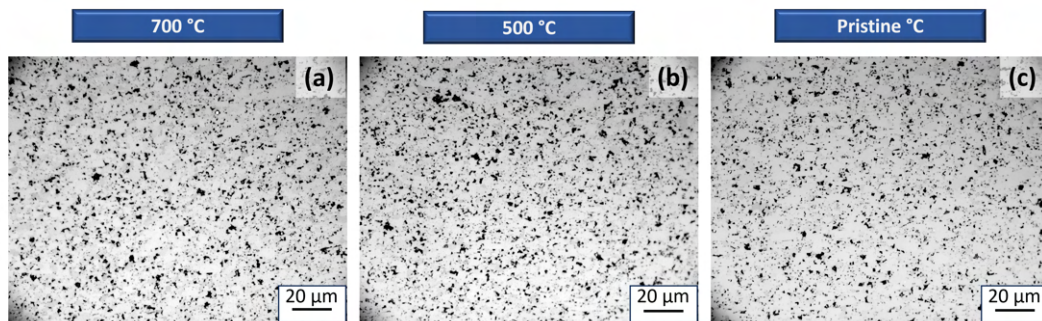
Figure 4.25.: Microstructure of annealed Y35 hexaferrite: annealed at 700 °C (a), 500 °C (b) and pristine Y35 (c).

Table 4.6.: Porosity of Annealed Y35 Hexaferrites.

Temperature	Pristine	500 °C	700 °C
Porosity	9.52	8.78	7.74

No significant influence on magnetic parameters and the magnetization curves are observed. An overview of the resulting magnetization curves and the corresponding parameters are given in figure 4.26 and table 4.7.
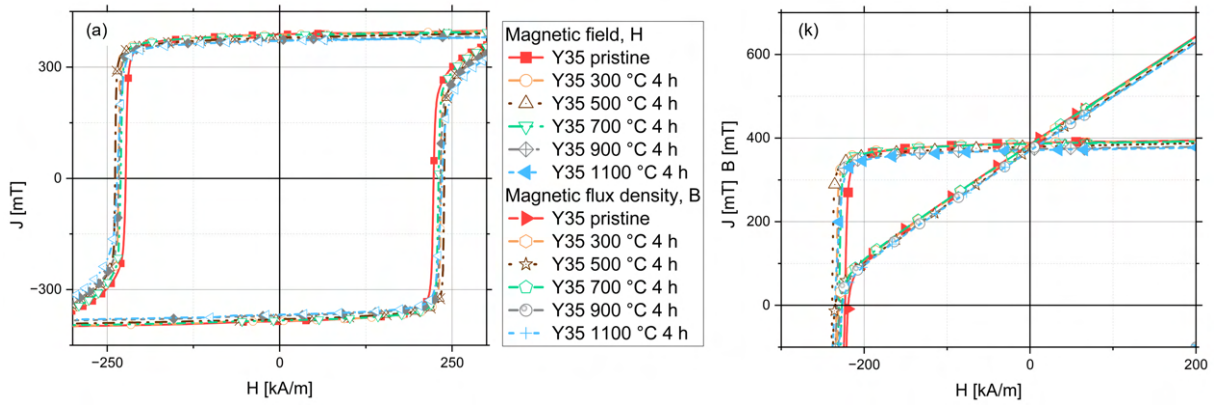
Figure 4.26.: Magnetization curves of annealed Y35 hexaferrite: overview of J-H curves (a), the 2nd quadrant of the magnetization curve, including the B-H curve (b).

Table 4.7.: Magnetic parameters of Annealed Y35 Hexaferrites.

Annealed Y35	$\mathbf{H_{cJ}}[\mathrm{kA/m}]$	$\mathbf{H_{cB}}[\mathrm{kA/m}]$	$\mathbf{B_r}[\mathrm{mT}]$	$\mathbf{J_s}[\mathrm{mT}]$	$\mathbf{BH_{max}}[\mathrm{kJ/m^3}]$
Pristine (X-Y corrected raw data)	222.6	218.7	386.1	403.3	27.9
Pristine (Interpolation)	223.2	219.2	385.9	404.5	27.6
300°C for 4 h (X-Y corrected raw data)	233.5	230.8	379.5	402.0	28.0
300°C for 4 h (Interpolation)	233.5	230.8	382.3	403.3	27.4
500°C for 4 h (X-Y corrected raw data)	238.6	235.2	384.7	397.8	27.0
500°C for 4 h (Interpolation)	238.6	235.2	373.0	397.4	26.1
700°C for 4 h (X-Y corrected raw data)	230.5	226.8	387.0	399.1	27.8
700°C for 4 h (Interpolation)	230.5	226.8	384.8	400.4	27.7
900°C for 4 h (X-Y corrected raw data)	233.0	229.3	371.9	386.2	26.0
900°C for 4 h (Interpolation)	233.0	229.2	371.5	387.8	26.0
1100°C for 4 h (X-Y corrected raw data)	235.5	225.9	369.1	384.1	25.7
1100°C for 4 h (Interpolation)	235.5	225.8	369.9	386.2	25.7

5. Discussion

5.1. HPT of Polymers

The difference in formability of different polymers is correlated to the chain mobility and molecular interactions. PP at RT already exists in a softened configuration with high chain mobility. In consequence, the relaxation behavior as well as the time dependence of deformation are more pronounced [39]. The phase-transition model can explain the smooth surface with hardly any visible defects shown in figure 4.1. This model suggests localized melting of the polymer, at the deformation temperature, followed by a reorganization and crystallization at the same temperature [109]. Liu et al. [109] also suggests that the degree of crystallinity of deformed PP only depends on the deformation temperature. At higher temperatures dislocation activity in crystalline areas is more pronounced [49]. This coupled with the higher chain mobility and lower shear modulus results in a lower torque during the deformation. Despite surface structures looking like shear bands are visible, it is more likely that these structures and the wavy surface form through interaction between the anvil surface and the sample combined with flow instabilities. According to Farrotti et al. [110] shear bands in iPP are more pronounced at low temperatures and high strain rates. For both samples, the high degree of crystal fragmentation followed by amorphization arises in strains exceeding the maximum strain of amorphous regions. A simplified deformation model including the crystal fragmentation is given in figure 2.9. According to Habumugisha et al. [111], stress-induced crystal amorphization and shear-induced crystal slipping are the controlling mechanisms during deformation. The higher crystallinity of the sample deformed at elevated temperature originates in relaxation and crystallization mechanisms during the cooling process accompanied by the formation of oriented fibrils [112–114]. To specify the present damage along with responsible deformation mechanisms and possible influence of the copolymer, further research is needed.

In contrast to PP, a pressure dependence of the dominant damage mechanism at a given stress is confirmed by the literature. Yuan et al. [115] describes the presence of a

brittle to ductile transition under pressure. Above this pressure, the formation of shear bands is favored instead of crazing. On the other hand, formability is dependent on the applied strain rate, temperature, and relaxation of the polymer. As a consequence of the high strain rate applied, the sample deformed in the glass state (at RT) shows a rather brittle damaged structure at the surface. However, no rupture of the sample is observed in succession to an increase in ductility. A rise in temperature in general leads to an increase in chain mobility. A higher chain mobility coupled with high pressure causes an increase in ductile deformation leading to less surface damage. Moreover, the white color of some surface structures on the PVC sample, deformed at 120 °C, also substantiates the presence of shear bands. Further studies are needed to study the influence of single parameters and present deformation mechanisms [39, 115, 116].

The good deformation capability of POM is mostly caused by the low T_g. As the RT lies above T_g, the chain mobility is relatively high. Accompanied by thermally activated deformation of crystalline regions, a high strain without severe damage is achieved. An increase in deformation temperature leads to a further increase of free volume, chain mobility, and crystalline deformation, enhancing deformability [39, 49, 117, 118].

At RT, PEEK is deformed at 0.15 T_g. Therefore deformation is mainly moderated by the amorphous phase in its glass state leading to localized strains between crystalline regions. Despite a complete fragmentation of crystalline regions is achieved, material damage is more pronounced at RT, as the polymer chain movement is limited. At 200 °C, lower relaxation time and higher chain mobility accompanied by thermal activated dislocation activity in crystalline regions leads to a better and uniform deformation. Further investigation of the sample surface and cross section not only revealed heavy surface damage, but also void formation and coalescence in the sample. Voids indicate that the deformation no longer fulfills the condition of volume constancy at this point [119–123]. According to Pawlak et al. [124] and Argon [39] the formation of voids is mainly induced by crazing, as cavitation should not occur under pressure loading. Moreover, a complete amorphization at 200 °C indicates a complete fragmentation of crystalline regions and the culmination of maximum deformation capability, set by the chain length. Further investigation on the exact damage mechanisms is recommended [119–123].

PTFE consists of a soft, amorphous phase and crystalline regions. In contrast to polymers like PE, PP, or PEEK, PTFE has no spherulitic structure. Instead, it consists of oriented grains surrounded by the amorphous phase, comparable with the structure of polycrystalline metals [125]. At both temperatures, the deformation occurs in the

planar zigzag structure due to the imposed pressure [65]. At RT, the deformation is mainly moderated by chain amorphous regions, accompanied by some planar slipping in the crystalline regions [125, 126]. On the other hand, sufficient plastic deformation is possible due to the less complex microstructure and possible relaxation in the amorphous regions [125]. With increasing pressure, an increase in elastic modulus is reported by Sauer et al. [127, 128]. This increase in elastic modulus is accompanied by a decrease in tensile strain. The limitation in crystal deformation at RT is mainly responsible for the material failure observed. At 200 °C, crystal deformation is more likely to occur. Moreover, deformation in amorphous regions no longer is limited by the glassy state. Instead, the amorphous regions are more comparable with a rubbery substance, making rearrangement and orientation of crystalline regions easier [126, 127, 129, 130]. This substantially affects the deformability. Comparing the preliminary experiments with the deformation of THOMAPLAST®, two reasons for the difference in deformation behavior are existent [125, 126, 129, 130]:

1. A different orientation of the microstructure due to processing. The preferred orientation in the THOMAPLAST® sample is in the axial direction. Since the PTFE rod is extruded, polymer chains are oriented in the axial direction, while in the sample produced by turning, the preferred orientation lies in the radial direction.

2. In the preliminary experiment the sample is heated to a temperature of 270 °C in an oven. A change in deformation properties due to thermal history accompanied by a more even temperature gradient across the sample influences deformation properties.

Further studies and characterizations, to fully understand the processes during HPT are advised.

5.2. Metal-Polymer Composites by Multi-Sector Disk HPT

Sandwich sheet compounds (sheet metal system, SMS) are well-known as innovative materials in the automotive and aerospace industries. As testing of SMS includes co-deformation in deep drawing, a comparison of processing SMS with HPT experiments is reasonable. In literature, the adhesion at the metal-polymer interface is one of the most important parameters. The initial adhesion in such materials is usually accomplished using resins as adhesive substances followed by a mechanical treatment

like role bonding (RB) or injection molding. In all cases, the treatment of the metal surface plays an important role in the bonding processes. Moreover, all suitable bonding processes include heat treatment of the metal and an adhesive or melting of the polymer.[131–134]. Samples in this thesis are not joint before deformation. Furthermore, no additional surface modifications, like etching or nanostructuring by laser or plasma treatment, are applied to metal parts, besides sandblasting and cleaning with ethanol (CH_3CH_2OH). Pohl et al. [99] describes the mechanism of co-deformation. At the beginning of deformation, the material with the lower yield point deforms solely, followed by the emergence of an interface-affected zone. Due to the adhesion of the joint, this zone is deformed more severely, acting as a stress redistribution and leading to further plastic deformation in the second phase. Also, the stress shielding of the stiffer material and phase thickness plays a role. This especially holds for metallic laminates and also was observed in [101]. In metal-polymer systems, the co-deformation mechanism including the interface interaction is more complex. There is the viscoelastic/ viscoplastic behavior of polymers which leads to a different amount of strain-hardening or softening, depending on the material, as well as different recovery and relaxation mechanisms. According to van Tijum [131], the interaction of the metal-polymer interface in the strain-hardening stage of deformation is dominated by the roughening of the polymer surface. This is due to the emergence of shear bands. The stored elastic energy in the polymer is one further factor determining the deformation behavior. Whether delamination occurs depends on the dominating mechanism and the thickness of the polymer layer. Van Tijum [131] found that polymer layers with increasing thickness enter a metastable state and are no longer considered stable against delamination. In addition, Kundig et al. [135] observed similar delamination effects in HPT co-deformation of polymers and metallic glasses.

In contrast to the studies discussed above, polymer regions in the unprocessed HPT samples are rather large and deformation is not performed under tension. The main problem observed in these samples is a lack of adhesion leading to delamination. For the PVC-Cu and PEEK-Cu samples, the processing temperatures lie between T_g and T_m (1.5 T_g and 1.38 T_g respectively). Despite Carrado et al [133] suggest better deformation results at elevated temperatures the pressure is set too low for sufficient deformation. Also, the similarity of the PVC and PEEK samples is intriguing. PVC is an amorphous polymer and lacks the additional stability of crystalline regions in the rubbery state, supporting the hypothesis of possible deformation at higher pressure. However, at higher pressure (5 GPa) a co-deformation was accomplished at RT and 2.13 T_g using POM. In the multi-sector disk approach, new surfaces are additionally created during deformation, making bonding more difficult [7, 133]. The improvement

in the layer structure, observed for increasing amount of segments is most likely caused by the smaller size of the segments accompanied by a smaller layer thickness. But at the same time, the POM-Cu sample consisting of 8 segments is more prone to delamination. One suggestion to overcome this problem is post deformation hot pressing, to ensure the adhesion. The exact mechanisms present in this co-deformation process are not fully understood yet and further studies could be of great scientific interest.

5.3. HPT of Magnetic Materials

5.3.1. HPT of Y35 M-type Hexaferrite

Commercial M-type Hexaferrites in cylindrical shape consist of grains oriented in the axial direction. The preferred orientation is given by the magnetic easy axis in $[0\,0\,0\,1]$ direction [36]. The existent high degree of orientation in Y35 ferrites is achieved by uniaxial pressing under an external magnetic field [136]. Hodge et al. [36] describes in his work the usage of deformation by compressive hot forming for the optimization of magnetic properties. These deformation experiments are based on creep mechanisms at temperatures above $1000\,°C$. No deformation experiments of M-type ferrites at lower temperatures are documented in the literature. At RT, diffusion processes necessary for creep are not active. In addition, grain boundary sliding described by Langdon [35] and dislocation movement is not possible at such low temperatures [20]. Therefore, no sufficient deformation is possible. However the dominating mechanism for deformation during HPT at RT is the fracture of grains. This is consistent with the findings of Greenberg et al. [90]. Similar to Hodge et al. [36], no increase of density during compressive loading is observed. This changes with applied torsion. Compression creates a microstructure with smaller pores and a beginning of particle refinement. However, the refined particles are not able to fill all pores. While during compression reorientation is limited, during HPT, oriented grains are refined and a material movement towards the edge of the anvil is introduced [36, 89, 90, 92]. This material flow leads to an increase in reorientation as shown in figure 5.1. The refinement of grains occurs along stress-activated slip systems in the hexagonal unit cell marked by linear parallel cracks visible in the SEM micrographs. The change in geometrical grain shape to rounded edges, with an increasing number of revolutions is also documented in the literature. Wang et al. [137] describes the HPT

processing of Mn_3O_4 powder. Moreover, the large variation in grain size in the samples is based on the same mechanisms described before.
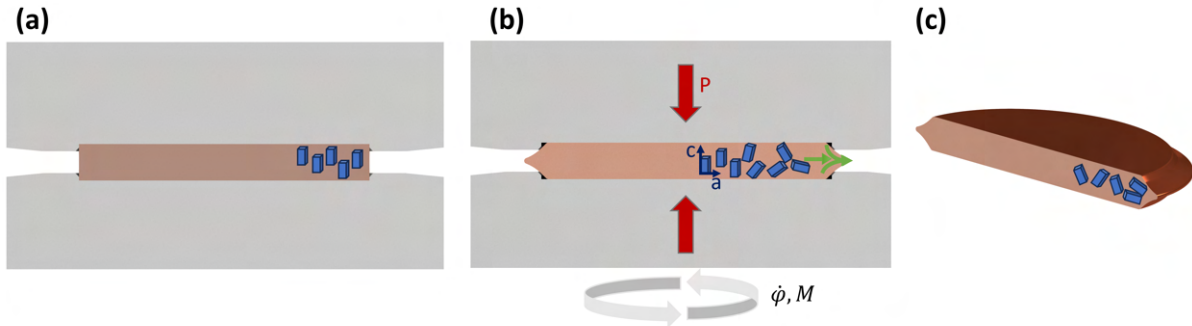
Figure 5.1.: Evolution of crystallite orientation of ceramics during HPT: pristine sample with highly oriented crystallites (a), reorientation of crystallites during HPT (b) and sample with rearranged crystallites after HPT (c). The loading conditions of the sample, pressure (P), torsion momentum (M) and the rotational speed ($\dot{\varphi}$) are indicated with arrows.

Measured changes in the magnetic properties are mainly based on the change of orientation. The influence of change in particle size of the fine grain fraction is masked by the higher fraction of large grains. Despite the particle size of $SrFe_{12}O_{19}$, lattice strain can influence the magnetic properties and the latter even can influence the inter-atomic exchange, through the spacing between atoms. No such influence can be detected with the used methods [138–140].

Samples deformed at $500\,°C$ show a different behavior. This is mainly to due the increase in diffusion linked to the elevated temperature. The amount of diffusion possible in Y35-ferrite is not only dependent on de diffusion in $SrFe_{12}O_{19}$, but also on the used additives. SiO_2, for example, inhibits grain boundary diffusion [79]. Since no Si is found in the used commercial materials, grain boundary diffusion should be possible to some amount [141, 142]. Moreover, this supports the presence of lattice strain in the deformed sample [20, 35, 36].

5.3.2. HPT of AlNiCo Alloys

During HPT in the AlNiCo alloys the grain boundary phases break and tilt like it is presented in figure 4.14. The precipitations are tilted and reoriented. The reorientation process and grain refinement represent expected development during HPT.AlNiCo alloys are nanostructured materials, displaying a coupled deformation of two α_1 and α_2 phases at RT. Zhang et al. [108] found similar lamelar structures, as shown in figure

4.14, in AlNiCo 8 alloys after hot rolling. According to [108] grains oriented in the deformation direction are deformed directly in lath-like structures, while other grains first break into particles followed by reorientation and formation of laths at a defined angle to the previous grain boundary. Angles between the same α phases are found to be either 60° or 120°. These angles also are found in the SEM micrographs of AlNiCo 5 and AlNiCo 8 samples. However, the absence of the de angular relation in deformed AlNiCo 3, is most likely due to the isotropic microstructure before the deformation [81, 85]. In addition, Zhang et al. described a change in phase composition during the deformation. The change in composition accompanied by the reorientation and structural refinement causes the change in the XRD pattern. In AlNiCo 3 a $(1\,1\,0)$ peak shift of 0.24° to lower diffraction angles shows the presence of lattice strain [143, 144]. All three AlNiCo grades are free of γ phase before and after deformation. Magnetic measurements show a decrease of H_c, B_r, J_s and BH_{max} leading to a narrow tilted magnetization curve. These findings are correlated to the disturbance of the ordered structure present in the undeformed samples, in particular, to the correlation between the preferred orientation of the FeCo-rich phase relative to the AlNi-rich phase. This is consistent with the results of swagging experiments on AlNiCo 5 by Kolbe et al. [145] and Zhang et al. [108]. Kolbe et al. [145] conducted magnetic measurements directly after swagging and reported a decrease in H_c, B_r and BH_{max}. On the other hand Zhang et al. [108] reported an increase of these properties combined with a change of relative orientation of the α_1 and α_2 phase, after magnetic-field heat treatment. Moreover, magnetic-field heat treatment and thermal aging play a crucial part in increasing H_c and BH_{max} after deformation [108].

5.4. Metal–Y35 Hexaferrite Composites by Multi-Sector Disk HPT

In experiments using the multi-sector disk approach, the formation of ceramic islands embedded in metal and alongside pure ceramic regions is based on the same mechanisms described in the chapters above. After compression, the ceramic is cracked in pieces of various size. During HPT, plastic deformation first occurs in the ductile metal. Dislocations accumulate at the metal–ceramic interface, imposing additional stress on the ceramic phase. Since no deformation of ceramic bulk material is possible, these additional stresses lead to cracking and breaking. On the other hand, this mechanism is primarily active at the metal–ceramic interface. Thus leading only to the chipping of small particles from the interface. These particles are further distributed in the metal

by the emerging material flow. In consequence, big ceramic parts are still present in the finished sample[97]. Following this argumentation, a reduction in ductile metal fraction leads to less stable samples, without any improvement of co-deformation. The main reason for the filigree samples is the minimized stabilizing effect of the ductile phase. Leading to samples mostly consisting of wedged ceramic fragments [90]. Similar effects were observed by Qi et al. [95] during the fabrication of Cu-ZnO composites using ZnO powder and Cu sheets. Despite the absence of co-deformation for this set-up, co-deformation of ceramic and metals is not impossible. According to Mara et al. [97], co-deformation of metal–ceramic nanolayered composites is possible for ceramic layer $\leq 5\,\mathrm{nm}$ (for Al–TiN system). The resolved shear stress in the ceramic layer ($\tau_{ceramic}^{RSS}$) for such a system is described by

$$\tau_{ceramic}^{RSS} = \tau^{interaction} + m(\sigma_{ceramic}^{dislocation} + \sigma^{applied}) \tag{5.1}$$

where $\tau^{interaction}$ is the stress imposed by the interaction of accumulated dislocations at the interface, $\sigma_{ceramic}^{dislocation}$ is the residual stress due to plastic incompatibility, $\sigma^{applied}$ is the applied stress and m is the Schmid factor [97].

5.5. Polymer–Y35 Hexaferrite Composites by Multi-Sector Disk HPT

For the co-deformation of ceramics with polymers not only the plastic incompatibility, but also the bonding at the interface are major challenges. For PTFE the deformation temperature is below $\mathrm{T_g}$ leading to limited plastic deformation. In addition, the surface does not bond with the ceramic. The latter is no surprise as PTFE is frequently used as a lubricant and anti-stick coating [57]. POM, on the other hand, exhibits a good flow around ceramic fragments. The difference in the deformation behavior of the polymer is based on the lower $\mathrm{T_g}$. Despite POM is forming a matrix, like shown in figure 4.18 , no co-deformation can be determined and the main refining process present in the ceramic is based on high pressure and grinding of ceramic particles between the anvils [90]. This also is supported by the increase of fine and dispersed ceramic fragments in the sample using POM sheets. Due to the less amount of damping by the polymer and the higher volume fraction of ceramic, contact between ceramic fragments is more frequent leading to finer fragments. The limited improvement of sample integrity by PDA is mainly caused by to short annealing time. In addition, pressure loading during the annealing provides better wetting of the interface [146, 147].

5.6. SrFe$_{12}$O$_{19}$ Powder Composites by HPT

Visible differences in phase distribution, grain size, and porosity in the compacted samples are caused by the difference in particle size of used powders [96, 148]. The difference in the shape of metal phases after the compaction is based on the stress shielding effect of the ceramic phase. Since Fe shows the lowest yield strength it displays the largest amount of deformation after compacting [97, 99] . In contrast to the metal–ceramic composites, the polymer–ceramic composites are less porous. This originates in the PTFE powder displaying a soft, almost spongy consistency. Chen et al. [98] describes the microstructure of virgin PTFE powder as particles consisting out of many nanoparticles held together by intermolecular forces. Such agglomerated particles would describe the observed properties. Moreover, during the compaction process, these nanoparticles flow in cavities and small pores creating the PTFE network between ceramic grains observed in light microscopy.

During HPT Cu, Fe, and Cr show a different amount of work hardening. Starink et al. [149] describes the difference in hardness of pure metals after 15 revolutions. His result reveals that the difference in Vickers hardness (ΔH_V) of Cr is 9.5 ΔH_V of Cu and Fe displays a ΔH_V of 6.2 ΔH_V of Cu. Hardness is related to the tensile strength (σ_{UTS}) by the relation [150–153]

$$H_V \approx 3\,\sigma_{UTS}. \tag{5.2}$$

This combined with the tendency of metals to show decreasing ductility with increasing σ_{UTS}, lays the basis for the different amount of spalling present in the metal–ceramic powder composites [22, 154]. As the work hardening increases from Cu to Cr the samples are more prone to mechanical failure. A similar effect is visible for regions of different amounts of strain, starting from the middle to the radial direction, resulting in different amounts of spalling along this gradient. Most cracks are formed in the ceramic phase or at the ceramic–metal interface, while the ductile metal phase acts like a crack arrest. With decreasing ductility, the cracks propagate along the grain boundaries and ceramic–metal interfaces. A second observation limited to the SrFe$_{12}$O$_{19}$–Fe and SrFe$_{12}$O$_{19}$–Cr composites is the pronounced gradient in grain refinement and phase distribution along the axial direction. This effect is based basically on three interlinking effects, co-deformability of the ceramic phase, chosen aspect ratio (¼), and phase distribution. The outer layers of the sample are subject to the most strain and therefore the first work-hardened zone. In a pure metal the outer layer would deform, work harden and as the yield strength of the material beneath is reached the

next layer is deformed. This subsequently leads to the whole sample being uniformly deformed and work-hardened if a ¼ ratio between ⅛ and ¹⁄₁₀ is maintained [89]. In the investigated composite samples, the powder particles of the ceramic phase are too big in size to co-deform. This leads to fragmentation of the ceramic as described before for the multi-sector disk composites. On the other hand, it shields metal layers beneath from deformation, leading to an increase in work hardening of layers near the surface. A major difference is the condition of the ceramic phase. Powder particles $\leq 44\,\mu m$ are only pressed together and fracture of the structure occurs at lower stresses. Since single-phase regions are a multiple of the particle size in the compacted samples, the work hardening of surface layers increases and spalling occurs before the material beneath is deformed homogeneously. This also is supported by the existence of a fine lamellar structured layer at the surface of the $SrFe_{12}O_{19}-Cr$ sample. In this layer, $SrFe_{12}O_{19}$ particles first were transported in the Cr phase by the same mechanism described for the multi-sector disk composites. But as the work hardening and the grain refinement increase the ceramic phase is distributed in fine laths. The structure of the layered structure is depicted in figure 5.2 For lath sizes less than $10\,\vec{b}$ where $\vec{b}$ is the burgers vector, even co-deformation is believed to be possible [97, 137].
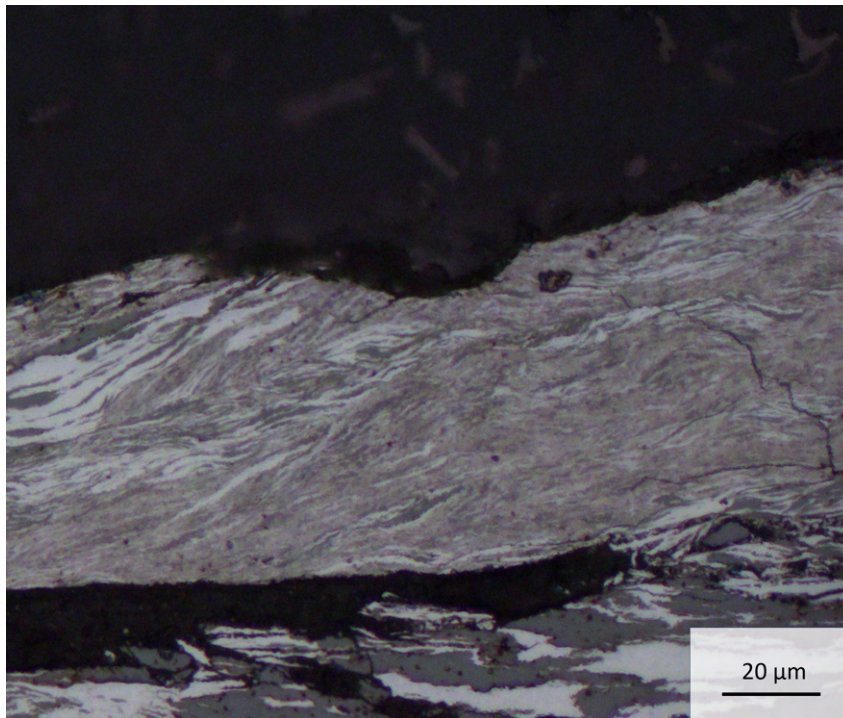

Figure 5.2.: Optical micrographs of the deformed $SrFe_{12}O_{19}-Cr$ powder composite at radial position 3 mm at the sample surface.

To achieve an exchange coupling interaction between the soft and hard magnetic phases, the maximum dimensions of soft magnetic regions are limited. At a layer thickness of the soft magnetic phase, higher than double the domain wall thickness (δ_b)

in the hard magnetic material, no exchange coupling is possible. Since in SrFe$_{12}$O$_{19}$, $\delta_b\ is \sim 10.5\,nm$, the maximum thickness of metal phase should not exceed $\sim 21\,nm$ [155, 156].

Bigger Cr or Fe regions in the composite are shaped in curls. These curls resemble structures observed by Qi et al. [95] as a result of vortex-like flow instabilities in the HPT sample. A microstructural optimization of the SrFe$_{12}$O$_{19}$–Fe and SrFe$_{12}$O$_{19}$–Cr powder composites should be possible with powder of smaller particle size, sufficient mixing, higher deformation pressure, and a decrease in sample thickness [89, 92]. The SrFe$_{12}$O$_{19}$–Cu powder composite displays a different deformation behavior. Due to the lower work hardening, the SrFe$_{12}$O$_{19}$ phase is more evenly distributed. The metal phase exhibits plastic material flow dispersing ceramic fragments, without crack propagation in Cu. But still ceramic fragments are too large in size for co-deformation to occur. However, it is remarkable that many clusters of SrFe$_{12}$O$_{19}$ accompanied with a significant porosity remain in the finished sample. Considering this besides the lower amount of flow instabilities in the SrFe$_{12}$O$_{19}$–Cu sample points to another important influence, the particle size ratio of used ceramic and metal powder ($D^{ceramic}/D^{metal}$, where D is the average particle size) [96].

In the SrFe$_{12}$O$_{19}$–PTFE powder composite the refinement of the ceramic phase is less pronounced. Since the hardness of PTFE is much lower than the hardness of SrFe$_{12}$O$_{19}$, even in the work-hardened state, no co-deformation is possible. Moreover, the polymer phase consisting of nanoparticles, is pressed out between the ceramic grains with increasing deformation. Therefore refinement of the ceramic is dominated by chipping of fragments under the imposed pressure. Deformation is limited to the PTFE phase in the form of nanoparticles sliding over each other with a small amount of deformation of the nanoparticles itself where sliding is not possible [97, 98, 126]. In literature, PTFE-ceramic composites are often accomplished using a cold sintering approach. While the method controlling the arrangement and size of the two phases is variable, the sintering step is important to form a stable polymer matrix along the grain boundaries of the ceramic phase. If a powders processing approach is chosen sufficient mixing is crucial. In addition, the ceramic powder can be surface treated to optimize interfacial adhesion [157–160].

Hard magnetic composites in literature are either based on dispersed magnetic particles in a polymer phase or nano-composite materials with tuned properties utilizing coupling mechanisms between the phases. In magnetic composites where both phases are too coarse for coupling interactions, the net magnetic flux is a superposition of the magnetic flux of both phases. This mechanism is the same for soft and hard

magnetic materials [156, 161–169]. In general, the magnetic properties of the composite material are related to the fraction of magnetic phase, the orientation of the magnetic particles, the particle size and shape [161–164]. The decrease of B_r in the $SrFe_{12}O_{19}$-Cu and $SrFe_{12}O_{19}$-Cr composite with deformation is based on the slight decrease of [0 0 0 1] orientation of the ferrite. H_c, on the other hand, increases slightly due to the existent grain refinement [161, 170]. In the deformed composites, the single phases still are too coarse for exchange interactions [78]. Due to the large particle size, the $SrFe_{12}O_{19}$-Fe composite shows the behavior of a soft magnetic composite [162, 163, 170]. For the $SrFe_{12}O_{19}$-PTFE composite the main parameter is the amount of polymer between the ceramic particles accompanied by the distribution of the magnetic phase. In contrast to the compacted $SrFe_{12}O_{19}$-PTFE samples, the deformed sample show larger $SrFe_{12}O_{19}$ clusters with less PTFE between the ceramic particles. The PTFE, still present in the ceramics, is distributed as thin film along the grain boundaries. This leads to a increase of H_c and B_r with deformation [171].

5.7. Annealing of Y35 Hexaferrites

The observed densification is supported by grain boundary diffusion processes [141, 172]. Typical sinter temperatures for M-type ferrites lie in the range of 1000 °C to 1300 °C. Since temperatures beneath 700 °C are significantly lower, only grain boundary diffusion is active at the temperatures considered above [136, 138, 141, 173]. For higher temperatures, volume diffusion and increasing triple point mobility [174] are also to be considered. The peak shift in the XRD is most likely caused by defects. A shift to higher 2θ values is linked to a decrease in the size of the unit cell. Moon et al. [175] and Lee et al. [176] observed similar peak shifts as an result of Ca and Al substitution in $SrFe_{12}O_{19}$ M-type ferrites. The slight decrease in B_r is also an effect documented by Lee et al. [176] for Substitution, but grain growth and a change in orientation also play a role. The increase of H_c with increasing temperature also supports the substitution theory as Wang et al. [77] and Lee et al. [176] observed similar effects for low levels of substitution by Ca and Al. Furthermore, the drop in H_{cJ} at 700 °C followed by an afresh increase, is caused by the increase of grain boundary diffusion. At 300 °C to 500 °C, the grain growth is slow, as the grain boundary diffusion is low at these temperatures. Ca^+ and Al^+ ions are already mobile enough to participate in Schottky and Frenkel reactions [141, 142]. Since no diffusion data for $SrFe_{12}O_{19}$, except self-diffusion described by Zhukovsky et al. [142] is available further studies are advised. With further increase in temperature, the grain growth rate gets larger

and H_{cJ} drops to a lower value. Since not only the grain growth, but also the cation diffusion increases, H_{cJ} increases. Ca and Al are confirmed in the used material by EDX.
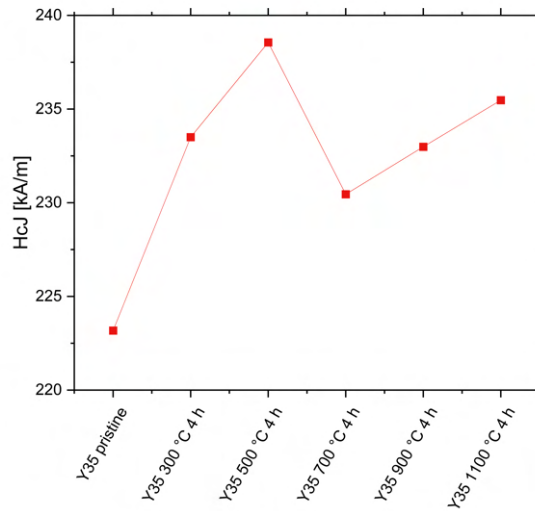
Figure 5.3.: Evolution of H_{cJ} with increasing temperature.

Values for J_s should be reconsidered in further studies since the $^l\!/_D$ ratio is only 0.3. According to Higgins et al. [14] and Chen et al. [15, 16] the $^l\!/_D$ ratio should be $\geq$ 1.8 to ensure a well defined magnetic field across the whole sample, which is important for valid measurement results. This value of minimal $^l\!/_D$ ratio is also affirmed by Bapu [13]. The results in this thesis affirm the negligibility influence of grain growth on magnetic properties up to the sinter temperature. Moreover, CaO and Al_2O_3 are used to achieve small grain sizes, along with a high density, optimized B_r and a higher stability against excessive grain growth [79, 136].

6. Conclusion

The feasibility of magnetic composite fabrication by HPT is studied in this thesis. Various material combinations, as Y35–POM, Y35–PTFE, Y35–Cu, Y35–Cr, Y35–Fe were processed in the multi-sector disc approach. In addition, $SrFe_{12}O_{19}$–PTFE, $SrFe_{12}O_{19}$–Cu, $SrFe_{12}O_{19}$–Cr, $SrFe_{12}O_{19}$–Fe were processed as powder composites.

Preliminary experiments reveal POM and PTFE to be adequate polymers for composite fabrication by HPT. Despite the limitation of deformation in polymers, Cu-polymer composites are fabricated with up to 3 revolutions. For samples created at RT, delamination is a common problem. Possible solutions for better surface adherence are surface treatments, bonding agents, and post-deformation hot pressing [146, 147]. Also, it is shown that process optimization leads to a more refined lamellar microstructure.

Bulk ceramics display a brittle behavior during HPT. The controlling factor is found to be the fracturing of existing grains followed by reordering and compaction of the created particles [90]. Since the reordering of the material is random, emerging orientations are hard to predict. Magnetic parameters like M_s, B_r, H_c, and BH_{max} are reduced with the decrease in orientation. The resulting HPT disks display a low structural integrity and a sintering step is needed to provide stable disks.

Upon plastic deformation, AlNiCo magnets show a refinement of the microstructure accompanied by a decrease in the orientation of the spinodal precipitations. The decrease in orientation causes a reduction of M_s, B_r, H_c and BH_{max}. Optimization of magnetic properties is expected to be possible by magnetic field heat treatment, as reported by Zhang et al. [108] and Kolbe et al. [145].

A fabrication of layered ceramic–metal composites using 8 segments in the multi-sector disk approach, is not feasible. One main drawback is the difference in plastic deformability accompanied by the low refinement rate of the bulk ceramic. This hinders a co-deformation and an even distribution of ceramic fragments in the metal. Experiments using less metal phase only lead to more fragile samples. No optimization in phase arrangement could be accomplished [95, 97]. The same holds for ceramic polymer composites, with additional adhesion problems at the ceramic–polymer

interface. Deformation of sintered bulk ferrite ceramics is reported to be possible at temperatures around 1200 °C [36]. Since the maximum temperature possible for the used HPT set-up is about 700 °C, deformation of bulk ferrites is considered as not feasible [92].

$SrFe_{12}O_{19}$–M composites are successfully fabricated by HPT processing of powder mixtures. The work-hardening properties of the metal accompanied by the particle size of the powders and the preceding mixing process, is found to be determining for the resulting microstructure. Spalling occurred in the $SrFe_{12}O_{19}$–Fe and $SrFe_{12}O_{19}$–Cr sample. The reason for spalling is the stress shielding mechanism imposed by large ceramic islands on metal regions beneath. Furthermore, this leads to excessive work hardening of metal layers at the surface. Due to the high amount of work hardening, the refinement of the ceramic and metal phases reaches a level where lamellar structures are formed and even co-deformation might be possible [97]. To achieve a homogeneous microstructure in the axial direction single-phase regions must be smaller and a homogeneous phase distribution in the compacted state is necessary. In the microstructure of fabricated samples, no co-deformation is present. For magnetic composites without exchange coupling between phases, magnetic properties are mainly governed by the orientation of magnetic particles and the amount of second phase between magnetic phase clusters and particles. On the other hand magnetic properties of the metal or polymer phase have an influence, especially for soft magnetic materials like Fe. While the deformation of compacted samples leads to a decrease in H_c, the $SrFe_{12}O_{19}$–Fe composite is already a soft magnetic composite in the compacted state. Using different material compositions combined with chosen powder particle sizes, magnetic properties can be tuned to some extent. Additional magnetic field heat treatment provides further tuning by controlling the orientation of magnetic particles [108, 138, 161–164, 166, 168, 169].

Annealing experiments of commercial Y35-ferrites affirm the grain size stability up to temperatures above 700 °C. The stabilizing effect of additives, like Al or Al_2O_3 are used in those commercial ferrites [79, 136]. Furthermore, substitution processes in $SrFe_{12}O_{19}$ during annealing are affirmed by XRD and magnetic measurements [77, 175, 176].

Appendix

Appendix A.

Data Processing

In the following pages, the methods of data processing used in this thesis are described in detail.

A.1. Micrograph Based Calculation of Porosity

For sintered materials, the porosity is an important parameter. This not only holds for ceramics as powder metallurgical processed metals and alloys also exhibit similar mechanisms and values of porosity. The most accurate way to determine the relative density ($\rho_{rel} = 1 - Porosity$) with the Archimedean principle. In this process, a known volume of the material is weighed in air and a medium with known density. Based on the difference between these two measurements ρ_{rel} can be calculated.Without such a measurement, it is possible to estimate the porosity using a micrograph. in this process, a section of the sample, which should represent the average porosity of the sample, is chosen. The ImageJ software is used to set a threshold for black spots. This threshold is adjusted till all pores are colored, but no coloring of grain boundaries or grains is allowed. The areal fraction of the pores is representative of the estimated value of porosity. To achieve better results, more than one area of the sample should be processed, and the arithmetic average used as the estimated porosity. An example of a processed sample is shown in figure A.1. A porosity of 9.97 % is observed in this example.
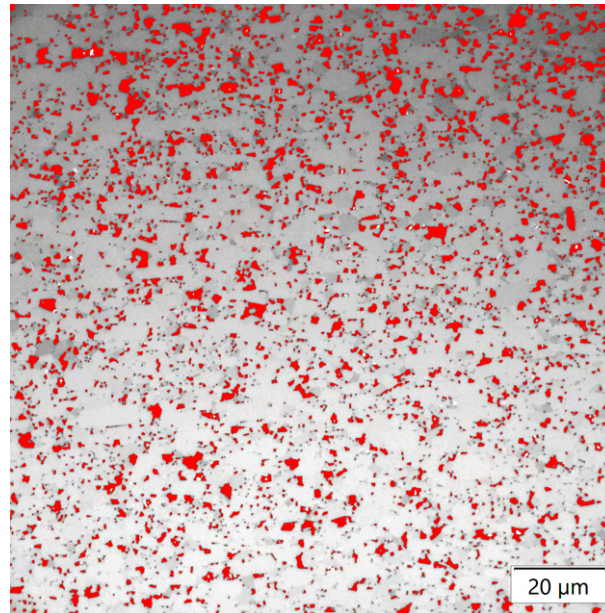
Figure A.1.: Estimation of porosity of Y35 magnetic ceramics using the ImageJ software. Pores are colored red.

A.2. Magnetic Data Acquisition with Python

```
1   ###########################################################################
2   ######              Program Analysis of magnetic data,            ######
3   ######       measured with the Brockhaus Hysterograpf at ESI Leoben      ######
4   ###########################################################################
5   #                 © created by Felix Römer and Philipp Payer
6   #
7   #  This program needs the Input data in form of an Excel file with
8   #  following structure:
9   #              Worksheet named "RawData"
10  #              1st row including the Header
11  #              H[kA/m], J[mT], B[mT]
12  #
13  #   The Program first corrects any shifts in the hysteresis and
14  #   calculates the values for:
15  #                  HcB [kA/m]
16  #                  Br [mT]
17  #                  HcJ [kA/m]
18  #                  Js [mT]
19  #                  Ms [kA/m]
20  #                  BHmax [kJ/m³]
21  #                  BHmax [MGOe]
22  #          the curve BH over B is calculated
23  #          and used for the calculation of BHmax
```

```python
# The H-M curve is calculated using the corrected H-J values
#
# In the second part, the Hysteresis is split and interpolated with
# segmented polynomials. I recommend to use of 5 to 12 segments
# with polynomial functions of maximum 6th order
#
# After the interpolation the  Data is stored and the same Parameters
# are calculated again. In one additional step, the values for µr are
# calculated as a function of B.
#
# All data corrections, Parameters, and interpolated Data are stored
# in .txt files in a folder with the name of the input file.
# For each step a figure is created and saved in the same folder
#
###############################################################################
#
#              !!!!!!!be aware that corrections of x-shifts
#                    can mask measured coupling effects  !!!!!!!!
#
######################### Import of Python packages #######################
import numpy as np
import matplotlib.pyplot as plt
get_ipython().run_line_magic('matplotlib', 'notebook')
import csv
import os
import math as m
# hysteresis package -> not used jet,
# import for eventual further analysis
import hysteresis as hys
# stoner package for Data analysis in physics
# -> not used jet, import for
# eventual further analysis or adaptation
import Stoner
# Pandas for work with data frames
import pandas as pd
from scipy.integrate import simpson
from numpy import trapz
import tkinter as tk
from tkinter import filedialog
from matplotlib.gridspec import GridSpec
from scipy.optimize import curve_fit
from scipy.optimize import leastsq
from scipy.optimize import minimize_scalar
from scipy.optimize import brentq
from scipy.interpolate import interp1d
import warnings
warnings.filterwarnings("ignore") #Ignore all warnings!
```

```python
1  ########################## Load File #####################################
2  root = tk.Tk()
3  root.withdraw()
4  filename = filedialog.askopenfilename()
5  print(filename)
6
7  directory = filename [:-5]
8  print(directory)
9  # Check whether the specified path exists or not
10 isExist = os.path.exists(directory)
11 if not isExist:
12 # Create a new directory because it does not exist
13     os.makedirs(directory)
14     print("The new directory is created!")
15
16 #defines varable for naming the exported files and the folder
17 full_name = os.path.basename(filename)
18 name = os.path.splitext(full_name)
19 print(full_name)
20 print(name[0])
21 ########################## Definitions and methods ##########################
22 #read hysteresis data from file
23 def read_hysteresis(file):
24     df = pd.read_excel(filename, sheet_name='RawData', usecols=[0, 1, 2],
25         names=["H [kA/m]", "J [mT]", "B [mT]"])
26
27     xH = df['H [kA/m]']
28     yJ = df['J [mT]']
29     yJ_name = 'J [mT]'
30     yB = df['B [mT]']
31     y_B = 'B [mT]'
32
33     myhyst = df
34
35     plt.close()
36     plt.plot(xH,yB, label = 'B')
37     plt.plot(xH,yJ, label = 'J')
38     plt.xlabel(df.keys()[0])
39     plt.ylabel(f'{df.keys()[1][:-5]} , {df.keys()[2]}')
40     plt.grid()
41     plt.legend()
42     plt.savefig(f'{directory}/JB vs H_uncorrected.png', bbox_inches='tight')
43
44
45     return xH,yJ,yB,df,myhyst
```

```python
1  #correction of shifts in the Hysteresis
2
3  def correct_y_shift(y_data):
4      y_corr =
5       y_data - (max(y_data)-(abs(max(y_data)+abs(min(y_data)))))/2
6      return y_corr
7
8  #split of hysteresis
9  def split_curve(x_data, y_data):
10     boundaries = []
11     for n, _ in enumerate(x_data):
12         if _ == max(x_data) or _ == min(x_data):
13             boundaries.append(n)
14     x1 = x_data[boundaries[0]:boundaries[1]]
15     y1 = y_data[boundaries[0]:boundaries[1]]
16     x2 = x_data[boundaries[1]:]
17     y2 = y_data[boundaries[1]:]
18     x_loop = x_data[boundaries[0]:]
19     y_loop = y_data[boundaries[0]:]
20     return x1,y1,x2,y2
21
22 def find_crossing(x1,x2,y1,y2):
23     m = (y2 - y1) / (x2 - x1)
24     b = y1 - m * x1
25     x_intersect = -b / m
26     return x_intersect
27
28
29 def correct_x_shift(x_data, y_data):
30     all_crossings = []
31     for i in range(len(y_data)):
32         if i >= 1:
33             if y_data[i]<0
34             and y_data[i-1]>0
35             or y_data[i]>0
36             and y_data[i-1]<0:
37                 x_intersect =
38                 find_crossing(x_data[i],x_data[i-1],y_data[i],y_data[i-1])
39                 all_crossings.append(x_intersect)
40     delta_x = all_crossings[1]-(all_crossings[1]-all_crossings[0])/2
41     Hc = abs(all_crossings[1]-delta_x)
42     x_corr = x_data-delta_x
43
44     return x_corr, Hc
```

89

```
1   #alternative code if a problem with the code above appeares
2   def find_crossings1(x_data, y_data):
3       crossings = []
4       for i in range(len(y_data)-1):
5           if y_data[i] * y_data[i+1] < 0:
6               crossing =
7               x_data[i] - (x_data[i+1] - x_data[i])
8                * y_data[i] / (y_data[i+1] - y_data[i])
9               crossings.append(crossing)
10      return crossings
11
12  def correct_x_shift2(x_data, y_data):
13      crossings = find_crossings1(x_data, y_data)
14      delta_x = np.mean(crossings)
15      x_corr = x_data - delta_x
16      crossings_corr = find_crossings1(x_corr, y_data)
17     # Hc = np.abs(np.mean(crossings_corr))
18      Hc = abs(crossings_corr[1] - delta_x)
19
20      return x_corr, Hc
21
22  def correct_x_shift1(x_data, y_data):
23      # Find the indices of positive and negative values
24      positive_indices = np.where(x_data > 0)[0]
25      negative_indices = np.where(x_data < 0)[0]
26
27      # Find the indices of the closest positive
28      # and negative values to the origin
29      closest_positive_index =
30        positive_indices[np.argmin(x_data[positive_indices])]
31      closest_negative_index =
32        negative_indices[np.argmax(x_data[negative_indices])]
33
34      # Interpolate the x-coordinates of the crossings
35      x1 = np.interp(0, [x_data[closest_positive_index],
36                         x_data[closest_negative_index]],
37                         [closest_positive_index, closest_negative_index])
38      x2 = np.interp(0, [x_data[closest_negative_index],
39                         x_data[closest_positive_index]],
40                         [closest_negative_index, closest_positive_index])
```

```python
    # Adjust the x-coordinates to center them around the origin
    center = (x1 + x2) / 2
    delta_x = (x1-center+x2-center)/2

    x1 -= center
    x2 -= center

    x_corr = x_data - delta_x

    crossings_corr = find_crossings1(x_corr, y_data)
    # Hc = np.abs(np.mean(crossings_corr))
    Hc = abs(crossings_corr[1] - delta_x)

    return x_corr, Hc

def correct_x_shift3(x_data, y_data):
    # Convert Pandas Series to NumPy arrays
    x_data = x_data.to_numpy()
    y_data = y_data.to_numpy()

    # Create a piecewise linear interpolation function
    interpolator = interp1d(x_data, y_data, kind='linear')

    # Find the x-coordinates of the crossings of the interpolation with the x-axis
    crossings = x_data[np.where(np.diff(np.sign(y_data)))[0]]

    # Find the two crossings closest to the origin without sorting
    origin = 0.0
    closest_crossings = crossings[np.argsort(np.abs(crossings - origin))[:2]]

    # Adjust the x-coordinates to center them around the origin
    center = np.mean(closest_crossings)
    x_corr = x_data - center

    # Calculate the corrected Hc as the absolute value of the
    # corrected crossings
    crossings_corr = closest_crossings-center
    Hc = np.abs(crossings_corr[0])

    return x_corr, Hc

#polynomial interpolation of the whole B-H hysteresis

def objective_func(coeffs, x, y):
    return np.polyval(coeffs, x) - y
```

```python
def int_segmented_polynomial(x, y, num_segments, max_degree):
    num_points = len(x)
    points_per_segment = num_points // num_segments

    segment_starts = []
    segment_ends = []
    segment_degrees = []
    int_curves = []


    for i in range(num_segments):
        start = i * points_per_segment
        end = start + points_per_segment
        segment_starts.append(start)
        segment_ends.append(end)

        best_degree = None
        min_residuals = float('inf')

        for degree in range(1, max_degree+1):
            segment_x = x[start:end]
            segment_y = y[start:end]

            initial_coeffs =
             np.polyint(segment_x, segment_y, deg=degree)
            coeffs, _ =
             leastsq(objective_func,
                     initial_coeffs,
                     args=(segment_x, segment_y))

            residuals =
             np.mean((np.polyval(coeffs, segment_x) - segment_y) ** 2)

            if residuals < min_residuals:
                min_residuals = residuals
                best_degree = degree

        segment_degrees.append(best_degree)

        segment_x = x[start:end]
        segment_y = y[start:end]
        initial_coeffs =
         np.polyint(segment_x, segment_y, deg=best_degree)
        coeffs, _ =
         leastsq(objective_func, initial_coeffs, args=(segment_x, segment_y))
        int_curve = np.polyval(coeffs, segment_x)
        int_curves.append(int_curve)

    return segment_starts, segment_ends, segment_degrees, int_curves
```

```python
########### reading and plotting of the uncorrected data #######################

xH,yJ,yB,df,myhyst = read_hysteresis(filename)
plt.title('Uncorrected Data')
plt.savefig(f'{directory}/JB vs H_uncorrected_.png',
            bbox_inches='tight')

################# H-J correction of the y shift ############################

yJ_corr = correct_y_shift(yJ)
print(f'{min(yJ_corr)},{max(yJ_corr)}')


plt.close()
plt.plot(xH,yJ, label = 'uncorrected J')
plt.plot(xH,yJ_corr, label = 'y-corrected J')
plt.xlabel(df.keys()[0])
plt.ylabel(f'{df.keys()[1][:-5]} [mT]')
plt.grid()
plt.legend()
plt.savefig(f'{directory}/J vs H_y-corrected.png',
            bbox_inches='tight')



############## H-B correction of the y shift ##############################

yB_corr = correct_y_shift(yB)
print(f'{min(yB_corr)},{max(yB_corr)}')


plt.close()
plt.plot(xH,yB, label = 'uncorrected B')
plt.plot(xH,yB_corr, label = 'y-corrected B')
plt.xlabel(df.keys()[0])
plt.ylabel(f'{df.keys()[2]}')
plt.grid()
plt.legend()
plt.savefig(f'{directory}/B vs H_y-corrected.png',
            bbox_inches='tight')
```

```python
1  ###################### H-J correction of the x shift #####################
2  #calc of HcJ
3  #chose 'correct_x_shift2'
4  #or 'correct_x_shift3' instaed if 'correct_x_shift' does not work
5  xJ_corr, HcJ = correct_x_shift3(xH,yJ_corr)
6  print(f'HcJ = {HcJ}')
7
8  Js = np.max(yJ_corr)
9  print('Js = ',Js)
10
11 plt.close()
12 plt.plot(xJ_corr,yJ_corr, label = 'xy-corrected J')
13 plt.xlabel(df.keys()[0])
14 plt.ylabel(f'{df.keys()[1]}')
15
16 plt.grid()
17 plt.legend()
18 plt.text(100,
19         500,
20         f'$J_s = {max(yJ_corr):6.2f}{df.keys()[0][1:]}$',
21         backgroundcolor='w')
22 plt.savefig(f'{directory}/J vs H_xy-corrected.png', bbox_inches='tight')
23 print(HcJ)
24
25 ###################### H-B correction of the x shift #####################
26 #calc of HcB
27 #chose 'correct_x_shift2'
28 # or 'correct_x_shift3' instaed if 'correct_x_shift' does not work
29 xB_corr, HcB = correct_x_shift(xH,yB_corr)
30
31
32
33 plt.close()
34 plt.plot(xB_corr,yB_corr, label = 'xy-corrected B')
35 plt.plot(xH,yB, label = 'uncorrected B')
36 plt.xlabel(df.keys()[0])
37 plt.ylabel(f'{df.keys()[2]}')
38 plt.plot(HcB,0,'o')
39 plt.plot(-HcB,0,'o')
40 plt.xlim(-HcB*2,HcB*2)
41 plt.ylim(-400,400)
42 plt.grid()
43 plt.legend()
44 plt.text(-0.1,0,f'$H_c = {HcB:6.2f}{df.keys()[0][1:]}$')#,backgroundcolor='w'.
45 plt.savefig(f'{directory}/B vs H_xy-corrected.png', bbox_inches='tight')
46 print(HcB)
```

```python
1   ################### calculation of the magnetization M ########################
2   #scaling of J with µ0 to get M
3   #setting the max of M as Ms
4
5   # Magnetic vaccuum permeability (magnetic field constant)
6   #in Si units (Vs/Am) or (Tm/A)
7   mu0 = 4*m.pi*10**(-7)
8   # Magnetization in Si units (A/m)
9   M_ = (yJ*10**(-3))/mu0
10  # Magnetization in Si units (kA/m)
11  M = M_*10**(-3)
12  #corrected Magnetization in Si units (A/m)
13  M_corr_ = (yJ_corr*10**(-3))/mu0
14  #corrected Magnetization in Si units (kA/m)
15  M_corr = M_*10**(-3)
16  #calc of Ms
17  Ms = np.max(M_corr)
18
19  ######### saving the corrected Data of H, J, B and M to a Text file ##########
20
21  df = pd.DataFrame({'HB [kA/m]':xB_corr,
22                     'B [mT]':yB_corr,
23                     'HJ [kA/m]':xJ_corr,
24                     'J [mT]':yJ_corr,
25                     'M [kA/m]':M_corr
26                     })
27  print(df)
28  df.to_csv(os.path.join(directory,
29          f'{filename[:-5]}/{name[0]}_corr.txt'),
30          index=False
31          )
32
33  ############## calculation of Br, BHmax and BH as a function of B ############
34  #results are stored in a txt file
35  # Reduction of Data to 2nd quadrant
36  second_quadrant_data =
37   np.array([(xB_corr[i], yB_corr[i])
38          for i in range(len(xB_corr))
39              if xB_corr[i] <= 0
40              and yB_corr[i] >= 0])
41  # Extract H and B values from second quadrant data
42  H_quadrant = second_quadrant_data[:, 0]
43  B_quadrant = second_quadrant_data[:, 1]
44
45  # print("Br:", Br)
46
47  # Find the index of the closest point to the y-axis
48  closest_index = np.argmin(np.abs(H_quadrant))
```

```python
# Retrieve the closest x and y values
closest_x = H_quadrant[closest_index]
closest_y = B_quadrant[closest_index]

print("Closest point to the y-axis (B-axis):")
print("x =", closest_x)
print("y =", closest_y)

# Extrapolate to find the crossing point
extrapolated_x = 0   # The x-value at which we want to find the crossing
extrapolated_y = np.interp(extrapolated_x, H_quadrant[::-1], B_quadrant[::-1])

print("Extrapolated crossing point:")
print("x =", extrapolated_x)
print("y =", extrapolated_y)

Br = extrapolated_y
print("Br estimated:", Br)

# calculate BH

BH = np.abs(B_quadrant*10**(-3))*np.abs(H_quadrant*10**(3))

BHmax_ = np.max(BH*10**(-3)) # [kA/m] * [mT] * 10^(-3) = [kJ/m³]

BHmax = np.max(BH*(10*10**(-6))*(10**(3)/79.577))# [Oe]*[MG] = [MGOe]

print('BHmax in Si-units [kJ/m³]: ',BHmax_)
print('BHmax [MGOe]: ',BHmax)

BH_data_df = pd.DataFrame({'H [kA/m]':H_quadrant,
                           'B [mT]':B_quadrant,
                           'BH [kJ/m³]':BH*10**(-3)
                           })
print(BH_data_df)
BH_data_df.to_csv(os.path.join(directory,
                  f'{filename[:-5]}/{name[0]}_BH_data.txt'),
                  index=False)
```

```python
# Plot the second quadrant data
plt.close()
plt.show()

fig = plt.figure(figsize=(7, 5))
gs = GridSpec(nrows=1, ncols=2)
gs.update(wspace=0.5, hspace=0.5)

ax0 = fig.add_subplot(gs[0])
ax0.plot(H_quadrant, B_quadrant)
ax0.set_xlabel('Magnetic Field Intensity, H [kA/m]')
ax0.set_ylabel('Magnetic Flux Density, B [mT]')
ax0.set_title('Hysteresis 2nd Quadrant')
ax0.grid(True)
ax0.set_xlim(-HcB, 0)
ax0.set_ylim(0,Br+5)
ax1 = fig.add_subplot(gs[1])
ax1.plot(BH*10**(-3), B_quadrant)
ax1.set_xlabel('Energy product, BH [kJ/m³]')
ax1.set_ylabel('Magnetic Flux Density, B [mT]')
ax1.set_title('BH')
ax1.grid(True)
ax1.set_ylim(0,Br+5)
ax1.set_xlim(0,BHmax_+ 0.5*BHmax)

fig.savefig(f'{directory}/BH.png', bbox_inches='tight')

#################### export of HcB, HcJ, Br, Js, Ms, BHmax,  ###############

print(directory)
index = [0]
magnetic_data_df = pd.DataFrame({'HcB [kA/m]':HcB,
                                 'HcJ [kA/m]':HcJ,
                                 'Br [mT]':Br,
                                 'Js [mT]':Js,
                                 'Ms [kA/m]':Ms,
                                 'BHmax [kJ/m³]':BHmax_,
                                 'BHmax [MGOe]':BHmax
                                }, index=index)
print(magnetic_data_df)
magnetic_data_df.to_csv(
                    os.path.join(directory,
                    f'{filename[:-5]}/{name[0]}_magnetic_data.txt'),
                    index=False)
```

```python
1   ################# masking of the H-B hysteresis data #####################
2   # masks out the re-curve part of the hysteresis (first increasing points)
3   #(cause this part could cause trouble with the splitting of the hysteresis)
4   # if you have good data you can adapt the splitting to use the whole
5   # corrected data by setting xB_corr as input of the splitting
6
7   # Define a threshold for the slight decrease in x
8   threshold = 0.1
9
10  # Find the index of the first occurrence of a slight decrease in x
11  decrease_index = np.argmax(np.diff(xB_corr) < -threshold)
12
13  # Create a mask to ignore data points before the decrease index
14  mask = np.arange(len(xB_corr)) >= decrease_index
15
16  # Apply the mask to the data
17  masked_xB_corr = xB_corr[mask]
18  masked_yB_corr = yB_corr[mask]
19
20  # Plot the masked hysteresis data
21  plt.close()
22  plt.plot(masked_xB_corr, masked_yB_corr)
23  plt.title('Masked Hysteresis Data')
24  plt.xlabel('H [kA/m]')
25  plt.ylabel('B [mT]')
26  plt.grid(True)
27  plt.show()
28
29  print(masked_xB_corr, masked_yB_corr)
30
31  ##################### Split the H-B Hysteresis ###########################
32  #Find the index where the x values start increasing
33  increase_start_index = np.where(np.diff(masked_xB_corr) > 0)[0][0]
34
35   # Split the data into two segments
36  x1 = masked_xB_corr[:increase_start_index]
37  y1 = masked_yB_corr[:increase_start_index]
38
39  x2 = masked_xB_corr[increase_start_index:]
40  y2 = masked_yB_corr[increase_start_index:]
41
42  # Plot the two segments
43  plt.close()
44  plt.plot(x1, y1, label='Decreasing branch')
45  plt.plot(x2, y2, label='Increasing branch')
46  plt.xlabel('H [kA/m]')
47  plt.ylabel('B [mT]')
48  plt.legend()
49  plt.grid(True)
50  plt.savefig(f'{directory}/B vs H_splitt.png', bbox_inches='tight')
51
52  # Print the data of the two segments
53  print("Decreasing branch (x1):", x1)
54  print("Decreasing branch (y1):", y1)
55  print("Increasing branch (x2):", x2)
56  print("Increasing branch (y2):", y2)
57
```

```python
58  ################## Split the H-B hysteresis Data alternative code ############
59  # #chose this code if the lines above do not work
60  # plt.close()
61  # boundaries = []
62  # for n, _ in enumerate(xB_corr):
63  #     if _ == max(xB_corr) or _ == min(xB_corr):
64  #         boundaries.append(n)
65
66  # print(boundaries)
67  # x1 = xB_corr[boundaries[0]:boundaries[1]]
68  # y1 = yB_corr[boundaries[0]:boundaries[1]]
69  # x2 = xB_corr[boundaries[1]:]
70  # y2 = yB_corr[boundaries[1]:]
71  # x_loop = xB_corr[boundaries[0]:]
72  # y_loop = yB_corr[boundaries[0]:]
73  # plt.plot(x1,y1, label = 'falling brance')
74  # plt.plot(x2,y2,label = 'rising branche')
75  # plt.xlabel('H [kA/m]')
76  # plt.ylabel('B [mT]')
77  # plt.grid(True)
78  # plt.legend()
79
80  # plt.savefig(f'{directory}/B vs H_splitt.png',
81  #             bbox_inches='tight'
82  #             )
83
84  # print(x1,x2)
85
86  ################## H-B polynomial interpolation #########################
87
88  # Create empty arrays to store the interpolated x and y
89  # values for both branches
90  int_x1 = np.empty(0)
91  int_y1 = np.empty(0)
92  int_x2 = np.empty(0)
93  int_y2 = np.empty(0)
94
95  num_segments = 10
96  max_degree = 6
```

```python
# Interpolate and plot the first branch
segment_starts1, segment_ends1, segment_degrees1, int_curves1 =
    int_segmented_polynomial(x1, y1, num_segments, max_degree)
segment_starts2, segment_ends2, segment_degrees2, int_curves2 =
    int_segmented_polynomial(x2[::-1],
                             y2[::-1],
                             num_segments,
                             max_degree)

plt.close()
plt.show()

plt.scatter(x1, y1, label='Branch 1 - Original Data')
for segment_start1, segment_end1, int_curve1
    in zip(segment_starts1, segment_ends1, int_curves1):
    segment_x1 = x1[segment_start1:segment_end1]
    segment_y1 = int_curve1

    #plt.plot(segment_x1, segment_y1, label='Branch 1 - Segment int')

    int_x1 = np.concatenate((int_x1, segment_x1))
    int_y1 = np.concatenate((int_y1, segment_y1))

# Interpolate and plot the second branch

plt.scatter(x2, y2, color='c' ,label='Branch 2 - Original Data')
for segment_start2, segment_end2, int_curve2
    in zip(segment_starts2, segment_ends2, int_curves2):
    segment_x2 = x2[::-1][segment_start2:segment_end2]
    segment_y2 = int_curve2

    #plt.plot(segment_x2, segment_y2, label='Branch 2 - Segment int')

    int_x2 = np.concatenate((int_x2, segment_x2))
    int_y2 = np.concatenate((int_y2, segment_y2))
```

```python
# Combine the interpolated x and y values for both branches
#into a single array or DataFrame
combined_int_data =
 np.column_stack((np.concatenate((int_x1, int_x2[::-1][1:])),
                                    np.concatenate((int_y1,
                                                    int_y2[::-1][1:]
                                                    ))))
combined_int_df =
 pd.DataFrame({'H': combined_int_data[:, 0],
               'B': combined_int_data[:, 1]
               })
combined_int_df.to_csv(os.path.join(directory,
                    f'{filename[:-5]}/{name[0]}_B-H_int.txt'),
                    index=False)

xB_int = combined_int_data[:, 0]

# Plot the combined interpolation
plt.plot(combined_int_data[:, 0],
         combined_int_data[:, 1],
         "r-", label='Combined interpolation')


# Add labels, title, and grid
plt.xlabel('H [kA/m]')
plt.ylabel('B [mT]')
plt.title('Polynomial Interpolation of the Hysteresis Curve')
plt.grid(True)
plt.legend()
plt.savefig(f'{directory}/B vs H_int.png', bbox_inches='tight')

# Print the combined interpolated data
print(combined_int_data)
print(combined_int_df)

############## calculation of BH and BHmax with interpolation #################

# Reduce the combined interpolate or the first branch of the hysteresis
# to the second quadrant data
reduced_H_int = combined_int_data[:, 0]
reduced_B_int = combined_int_data[:, 1]

# Select only the data points in the second quadrant
second_quadrant_indices_int =
 np.where((reduced_H_int <= 0) & (reduced_B_int >= 0))
H_quadrant_int =
 reduced_H_int[second_quadrant_indices_int]
B_quadrant_int =
 reduced_B_int[second_quadrant_indices_int]
```

```
1   # Find the index of the closest point to the y-axis
2   closest_index_int = np.argmin(np.abs(H_quadrant_int))
3
4   # Retrieve the closest x and y values
5   closest_x_int = H_quadrant_int[closest_index_int]
6   closest_y_int = B_quadrant_int[closest_index_int]
7
8   print("Closest point to the y-axis (B-axis):")
9   print("x =", closest_x_int)
10  print("y =", closest_y_int)
11
12  # Extrapolate to find the crossing point
13  extrapolated_x_int = 0   # The x-value at which we want to find the crossing
14  extrapolated_y_int = np.interp(extrapolated_x_int,
15                                 H_quadrant_int[::-1],
16                                 B_quadrant_int[::-1])
17
18  print("Extrapolated crossing point:")
19  print("x =", extrapolated_x_int)
20  print("y =", extrapolated_y_int)
21
22  Br_int_ = extrapolated_y_int
23  print("Br estimated:", Br_int_)
24
25
26  # calculate BH
27  BH_int =
28   np.abs(B_quadrant_int * 10 ** (-3)) * np.abs(H_quadrant_int * 10 ** (3))
29
30  BHmax_int_ =
31   np.max(BH_int*10**(-3)) # [kA/m] * [mT] * 10^(-3) = [kJ/m³]
32  # [Oe]*[MG] = [MGOe]
33  BHmax_int =
34   np.max(BH_int * (10 * 10 ** (-6)) * (10 ** (3) / 79.577))
35
36  print('BHmax in Si-units [kJ/m³]: ',
37        BHmax_int_)
38
39  BH_data_df_int = pd.DataFrame({'H [kA/m]': H_quadrant_int,
40                                 'B [mT]': B_quadrant_int,
41                                 'BH [kJ/m³]': BH_int * 10 ** (-3)
42                                 })
43  print(BH_data_df_int)
44  BH_data_df_int.to_csv(os.path.join(directory,
45                    f'{filename[:-5]}/{name[0]}_BH_int_data.txt'),
46                    index=False)
```

```python
# Plot the second quadrant data with interpolated curve
plt.close()
plt.show()

fig_1 = plt.figure(figsize=(7, 5))
gs = GridSpec(nrows=1, ncols=2)
gs.update(wspace=0.5, hspace=0.5)

ax4 = fig_1.add_subplot(gs[0])
ax4.plot(H_quadrant_int, B_quadrant_int)
ax4.set_xlabel('Magnetic Field Intensity, H [kA/m]')
ax4.set_ylabel('Magnetic Flux Density, B [mT]')
ax4.set_title('Hysteresis 2nd Quadrant with interpolated Curve')
ax4.grid(True)
ax4.set_xlim(-HcB, 0)
ax4.set_ylim(0, Br_int_ + 5)

ax5 = fig_1.add_subplot(gs[1])
ax5.plot(BH_int * 10 ** (-3), B_quadrant_int)
ax5.set_xlabel('Energy product, BH [kJ/m³]')
ax5.set_ylabel('Magnetic Flux Density, B [mT]')
ax5.set_title('BH with interpolated Curve')
ax5.grid(True)
ax5.set_ylim(0, Br_int_ + 5)
ax5.set_xlim(0, BHmax_int_ + 0.5*BHmax_int)

fig_1.savefig(f'{directory}/BH_int.png', bbox_inches='tight')

######################## calculation of µr ##################################
# calculation with interpolated data
#H=B/(µ0*µr)
mur =
  (np.abs((int_x1*10**(3)) * 4*m.pi*10**(-7)) )/np.abs((int_y1 *10**(-3)))

plt.close()
plt.show()
fig2 = plt.figure(figsize=(7, 7))
gs = GridSpec(nrows=1, ncols=1)
gs.update(wspace=0.5, hspace=0.5)

ax0 = fig2.add_subplot(gs[0])
ax0.plot(int_x1, int_y1, label='B')
ax0.plot(int_x1, mur, label='µr')
ax0.set_xlabel('Magnetic Field Intensity, H [kA/m]')
ax0.set_ylabel('Magnetic Flux Density, B [mT]')
ax0.set_title('Hysteresis 2nd Quadrant with interpolated Curve')
ax0.grid(True)

fig2.savefig(f'{directory}/B_vs_H_mu-r_int.png', bbox_inches='tight')

# plt.close()
# plt.plot(int_x1, int_y1, label='B')
# plt.plot(int_x1, mur, label='µr')
# plt.grid(True)
# plt.legend()
# plt.savefig(f'{directory}/B vs H_mur.png', bbox_inches='tight')
```

```
58  print(mur)
59
60  ########################### export of µr ###################################
61
62
63  mu_data_df = pd.DataFrame({'H [kA/m]':int_x1,'B [mT]':int_y1, 'µr
64  []':mur})
65  print(mu_data_df)
66  mu_data_df.to_csv(os.path.join(directory,
67                                 f'{filename[:-5]}/{name[0]}_mu_data.txt'),
68                                 index=False)
69
70  ########################### calculation of Br and HcB wit interpolation #####
71
72  # Find the index of the x-axis crossing closest to 0
73  xB_index = np.abs(int_y1).argmin()
74  xB_crossing = int_x1[xB_index]
75
76  # Find the index of the y-axis crossing closest to 0
77  yB_index = np.abs(int_x1).argmin()
78  yB_crossing = int_y1[yB_index]
79
80
81  HcB_int = abs(xB_crossing)
82  Br_int = yB_crossing
83
84
85  # Print the x-axis and y-axis crossings
86  print("HcB:", HcB_int)
87  print("Br:", Br_int)
```

```python
######################### masking of the H-J hysteresis data #################

# Define a threshold for the slight decrease in x
threshold = 0.1

# Find the index of the first occurrence of a slight decrease in x
decrease_index = np.argmax(np.diff(xJ_corr) < -threshold)

# Create a mask to ignore data points before the decrease index
mask = np.arange(len(xJ_corr)) >= decrease_index

# Apply the mask to the data
masked_xJ_corr = xJ_corr[mask]
masked_yJ_corr = yJ_corr[mask]

# Plot the masked hysteresis data
plt.close()
plt.plot(masked_xJ_corr, masked_yJ_corr)
plt.title('Masked Hysteresis Data')
plt.xlabel('H [kA/m]')
plt.ylabel('J [mT]')
plt.grid(True)
plt.show()

print(masked_xJ_corr, masked_yJ_corr)

#################### split the H-J hysteresis Data ##########################
# Find the index where the x values start increasing
increase_start_index = np.where(np.diff(masked_xJ_corr) > 0)[0][0]

# Split the data into two segments
x1J = masked_xJ_corr[:increase_start_index]
y1J = masked_yJ_corr[:increase_start_index]

x2J = masked_xJ_corr[increase_start_index:]
y2J = masked_yJ_corr[increase_start_index:]
# Plot the two segments
plt.close()
plt.plot(x1J, y1J, label='Decreasing branch')
plt.plot(x2J, y2J, label='Increasing branch')
plt.xlabel('H [kA/m]')
plt.ylabel('J [mT]')
plt.legend()
plt.grid(True)
plt.savefig(f'{directory}/B vs H_splitt.png', bbox_inches='tight')
# Print the data of the two segments
print("Decreasing branch (x1):", x1)
print("Decreasing branch (y1):", y1)
print("Increasing branch (x2):", x2)
print("Increasing branch (y2):", y2)
```

```
1   ############## split the H-J hysteresis Data alternative code ############
2   # #chose this code if the lines above do not work
3   # boundaries = []
4   # for n, _ in enumerate(xJ_corr):
5   #     if _ == max(xJ_corr) or _ == min(xJ_corr):
6   #         boundaries.append(n)
7
8   # print(boundaries)
9   # x1J = xJ_corr[boundaries[0]:boundaries[1]]
10  # y1J = yJ_corr[boundaries[0]:boundaries[1]]
11  # x2J = xJ_corr[boundaries[1]:]
12  # y2J = yJ_corr[boundaries[1]:]
13  # x_loop = xJ_corr[boundaries[0]:]
14  # y_loop = yJ_corr[boundaries[0]:]
15
16  # plt.close()
17  # plt.show()
18  # fig3 = plt.figure(figsize=(5, 5))
19  # gs = GridSpec(nrows=1, ncols=1)
20  # gs.update(wspace=0.5, hspace=0.5)
21
22  # ax = fig3.add_subplot(gs[0])
23
24  # ax.plot(x1J,y1J, label = 'falling brance')
25  # ax.plot(x2J,y2J,label = 'rising branche')
26  # plt.xlabel('H [kA/m]')
27  # plt.ylabel('B [mT]')
28  # ax.legend(loc='upper left', fontsize='x-small')
29  # ax.grid(True)
30
31  # fig3.savefig(f'{directory}/J vs H_splitt.png', bbox_inches='tight')
32
33  # print(x1J,x2J)
```

```python
1  ########### polynomial interpolation of the H-J hysteresis Data ##########
2  # Create empty arrays to store the interpolated x and y values
3  # for both branches
4  int_x1J = np.empty(0)
5  int_y1J = np.empty(0)
6  int_x2J = np.empty(0)
7  int_y2J = np.empty(0)
8
9  num_segments_J = 6
10 max_degree_J = 6
11
12 # Interpolation and plot the first branch
13 segment_starts1J, segment_ends1J, segment_degrees1J, int_curves1J =
14     int_segmented_polynomial(x1J, y1J,num_segments_J, max_degree_J)
15 segment_starts2J, segment_ends2J, segment_degrees2J, int_curves2J =
16     int_segmented_polynomial(x2J[::-1],
17                              y2J[::-1],
18                              num_segments_J,
19                              max_degree_J)
20
21 plt.close()
22 plt.show()
23
24 plt.scatter(x1J, y1J, label='Branch 1 - Original Data')
25 for segment_start1J, segment_end1J, int_curve1J
26     in zip(segment_starts1J, segment_ends1J, int_curves1J):
27     segment_x1J = x1J[segment_start1J:segment_end1J]
28     segment_y1J = int_curve1J
29
30     #plt.plot(segment_x1, segment_y1, label='Branch 1 - Segment int')
31     int_x1J = np.concatenate((int_x1J, segment_x1J))
32     int_y1J = np.concatenate((int_y1J, segment_y1J))
33
34 # Interpolation and plot the second branch
35 plt.scatter(x2J, y2J, color='c' ,label='Branch 2 - Original Data')
36 for segment_start2J, segment_end2J, int_curve2J
37     in zip(segment_starts2J, segment_ends2J, int_curves2J):
38     segment_x2J = x2J[::-1][segment_start2J:segment_end2J]
39     segment_y2J = int_curve2J
40
41     #plt.plot(segment_x2, segment_y2, label='Branch 2 - Segment int')
42
43     int_x2J = np.concatenate((int_x2J, segment_x2J))
44     int_y2J = np.concatenate((int_y2J, segment_y2J))
```

```python
1  # Combine the interpolated x and y values for both branches
2  # into a single array or DataFrame
3  combined_int_dataJ =
4   np.column_stack((np.concatenate((int_x1J,
5                                    int_x2J[::-1][1:])),
6                                     np.concatenate((int_y1J,
7                                                     int_y2J[::-1][1:]
8                                                     ))))
9  combined_int_J_df =
10   pd.DataFrame({
11   'H': combined_int_dataJ[:, 0],
12   'J': combined_int_dataJ[:, 1]
13   })
14  combined_int_J_df.to_csv(
15                           os.path.join(directory,
16                           f'{filename[:-5]}/{name[0]}_J-H_int.txt'),
17                           index=False)
18
19  xJ_int = combined_int_dataJ[:, 0]
20
21  # Plot the combined interpolation
22  plt.plot(combined_int_dataJ[:, 0],
23          combined_int_dataJ[:, 1],
24          "r-", label='Combined interpolation'
25          )
26
27  # Add labels, title, and grid
28  plt.xlabel('H [kA/m]')
29  plt.ylabel('J [mT]')
30  plt.title('Polynomial interpolation of the Hysteresis Curve')
31  plt.grid(True)
32  plt.legend(loc='upper left', fontsize='x-small')
33  plt.savefig(f'{directory}/J vs H_int.png', bbox_inches='tight')
34
35  # Show the legend and the plot
36  #plt.legend()
37  plt.show()
38
39  # Print the combined interpolated data
40  print(combined_int_dataJ)
41  print(combined_int_J_df)
```

```python
########## calculation of Js, M(H) and Ms with interpolated data ############
Js_int = np.max(int_y1J)
#corrected Magnetization in Si units (A/m)
M_int_ = (int_y1J*10**(-3)))/mu0
#corrected Magnetization in Si units (A/m)
M_int_full = (combined_int_dataJ[:, 1]*10**(-3)))/mu0
#corrected Magnetization in Si units (kA/m)
M_int = M_int_full*10**(-3)

Ms_int = np.max(M_int)
print('Ms [kA/m] = ',Ms_int)
############### calculation of HcJ with interpolated data ###################
# Find the index of the x-axis crossing closest to 0
xJ_index = np.abs(int_y1J).argmin()
xJ_crossing = int_x1J[xJ_index]
# Find the index of the y-axis crossing closest to 0
yJ_index = np.abs(int_x1J).argmin()
yJ_crossing = int_y1J[yJ_index]

HcJ_int = abs(xJ_crossing)
Jr_int = [yJ_crossing]
# Print the x-axis and y-axis crossings
print("HcJ:", HcJ_int)
print("Y-axis crossing:", yJ_crossing)
###### exporting the magnetic data calculated wit the interpolated data ######
index = [0]
magnetic_data_int_df = pd.DataFrame({'HcB [kA/m]':HcB_int,
                                     'HcJ [kA/m]':HcJ_int,
                                     'Br [mT]':Br_int,
                                     'Js [mT]':Js_int,
                                     'Ms [kA/m]':Ms_int,
                                     'BHmax [kJ/m³]':BHmax_int_,
                                     'BHmax [MGOe]':BHmax_int
                                     }, index=index)
print(magnetic_data_int_df)
magnetic_data_int_df.to_csv(
                     os.path.join(directory,
                     f'{filename[:-5]}/{name[0]}_magnetic_data_int.txt'),
                     index=False)
##############################################################################
# To get more information out of your data, the data must be of good quality.
# You can model the isotropic parameters with the Jilles-Atherton model or
# use the Preisach model.
##############################################################################
```

Source code A.1: Python code for processing magnetization data measured with a Brockhaus hystograph. Occurring shifts of the hysteresis on both axis are corrected and magnetic parameters, as H_c, B_r, M_s and BH_{max} are calculated.

Appendix B.

Material Cards of Used Polymers

The following material cards should give a broad overview of the properties of polymers used in this thesis. All material cards are extracted from G. Ehrenstein's work [37] and supplemented with details from Osswald et al. [56].

PP-H – Polypropylene (Homopolymer; isotactic)

Microstructure: semi-crystalline
(60 % - 70 %)

Characteristics: inexpensive, versatile, low strength and stiffness, low dimensional stability, low stress cracking, chemical resistance, copolymerization with ethylene reduces glass transition temperature; often filled and reinforced, homopolymer brittle at low temperatures

Identified by: translucence, smell of paraffin during burn test,
bright blue dripping flame during burn test, floats on water

Parameters:

$\rho\ = 0.90 - 0.91\ \frac{g}{cm^3}$
$E\ = 1300 - 1800\ \text{MPa}$
$\sigma_s\ = 25 - 40\ \text{MPa}$
$\varepsilon_s\ = 8 - 18\ \%$
$\varepsilon_B\ = > 50\ \%$
$T_g\ = 0 - 20\ °C$
$T_m = 160 - 165\ °C$

Operational limits:

$T_{max}^{long\ term}\ \sim\ 130\ °C$
$T_{max}^{short\ term}\ \sim 90\ °C$

Chemical structure:
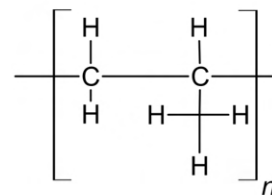
Blends:
PE, EPDM

σ– ε– Diagram:

Elastic modulus:

DSC–Diagram:

Coefficient of expansion:

Material card B.1.: General properties of polypropylene[37].
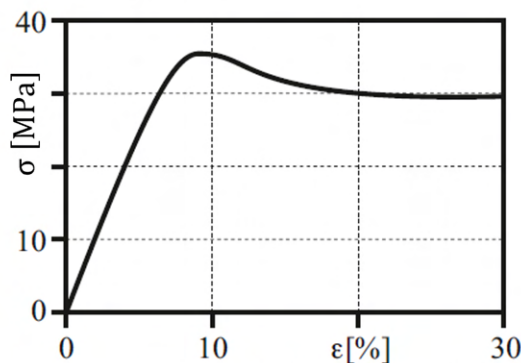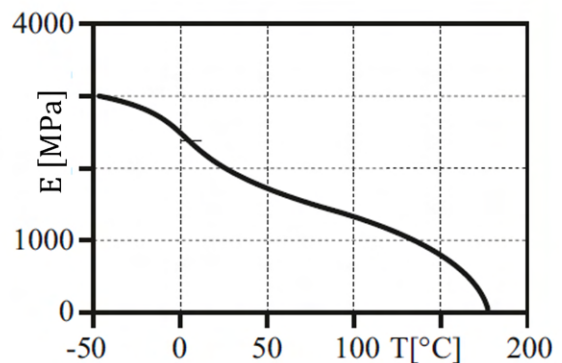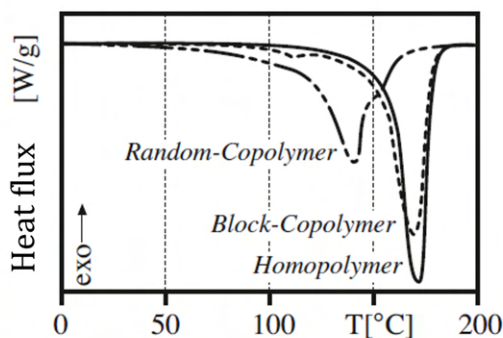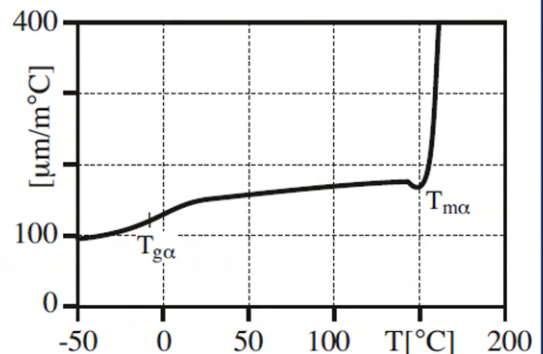
PVC-U – Polyvinylchloride (unplasticized)

Microstructure: amorphous

Characteristics: low toughness at low temperature, good dimensional stability, good environmental and chemical resistance, flame retardant, large variability in properties when plasticized; inexpensive

Identified by: transparency to opaqueness, toxic fumes during burn test, release of hydrochloric acid during burn test, self extinguishing

Parameters:

$\rho = 1.38 - 1.55\ \frac{g}{cm^3}$
$E = 2700 - 3000\ MPa$
$\sigma_s = 50 - 60\ MPa$
$\varepsilon_s = 4 - 6\ \%$
$\varepsilon_B = 10 - 50\ \%$
$T_m = 80\ °C\ Homopolymer$

Operational limits:

$T_{max}^{long\ term} \sim 60°C$
$T_{max}^{short\ term} \sim 70\ °C$

Chemical structure:
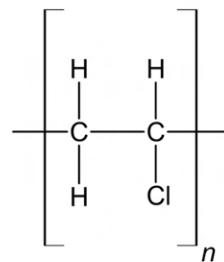
Blends:
ABS, NBR, PE-C, PMMA

σ– ε– Diagram:

Elastic modulus:

DSC–Diagram:

Coefficient of expansion:

Material card B.2.: General properties of poly(vinyl chloride)[37].
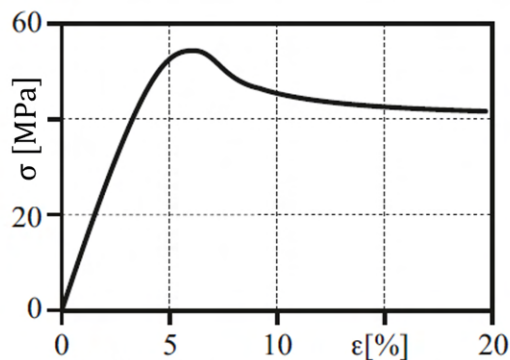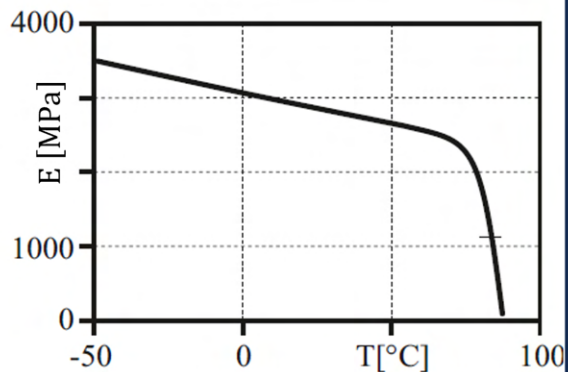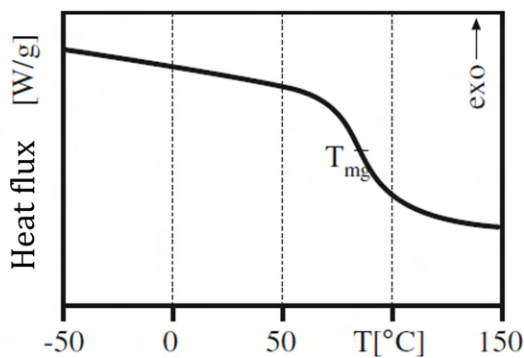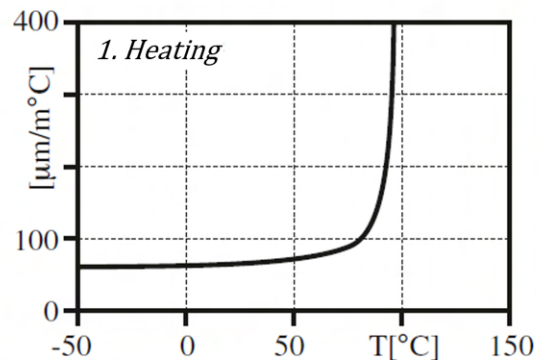
POM – Polyoxymethylene (Polyacetal; Polyformaldehyde)

Microstructure: semi-crystalline
(Homopolymer 70 %-80 %; Copolymer 50 %-60 %)

Characteristics: high strength and stiffness, high flexibility, low friction coefficient, high dimensional stability, low susceptibility to stress cracking, sensitivity to UV light

Identified by: opaque - white color, smell of formaldehyde during burn test, blue, dripping flame during burn test
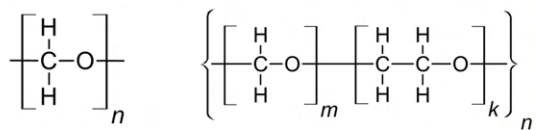
Parameters:

$\rho = 1.39 - 1.43 \frac{g}{cm^3} \ (H > C)$
$E = 2600 - 3200 \ \text{MPa} \ (H > C)$
$\sigma_s = 60 - 75 \ \text{MPa}$
$\varepsilon_s = 8 - 25 \ \%$
$\varepsilon_B = 20 \ to \ > 50 \ \% \ Homopolymer$
$\quad\ 15 \ to \ 40 \ \% \quad Copolymer$
$T_g = -70 \ ℃$
$T_m = 175 \ ℃ \ Homopolymer$
$\quad\ 164 - 172 \ ℃ \ Copolymer$

Operational limits:

$T_{max}^{long \ term} \sim 90 - 100 \ ℃$
$T_{max}^{short \ term} \sim 110 - 140 \ ℃$

Chemical structure:

Homopolymer (H)   Copolymer (C)

Co-monomers:
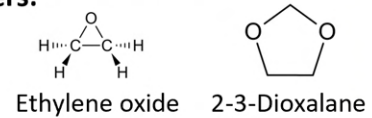
Ethylene oxide   2-3-Dioxalane

Blends:
PUR, PE, PTFE

σ– ε– Diagram:

Elastic modulus:

DSC–Diagram:

Copolymer

Homopolymer

Coefficient of expansion:

Material card B.3.: General properties of poly(oxymethylene) [37].
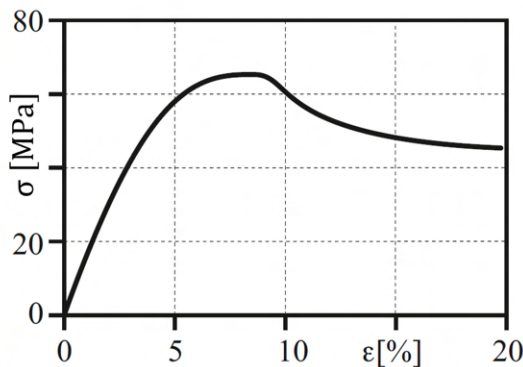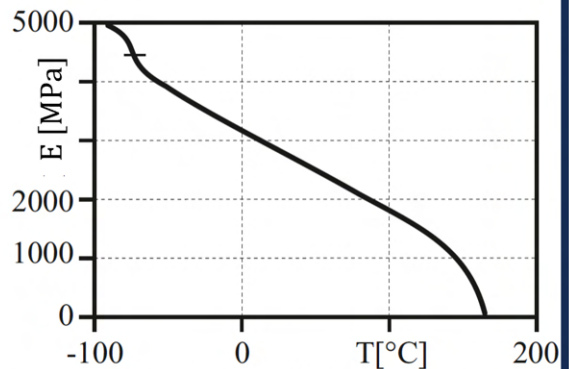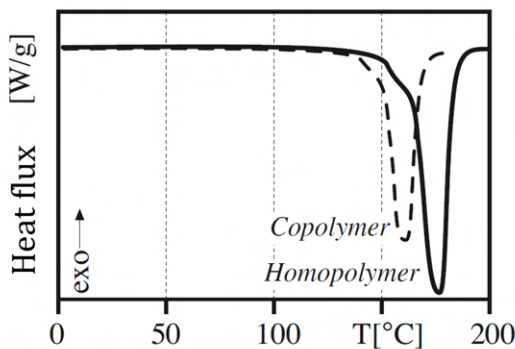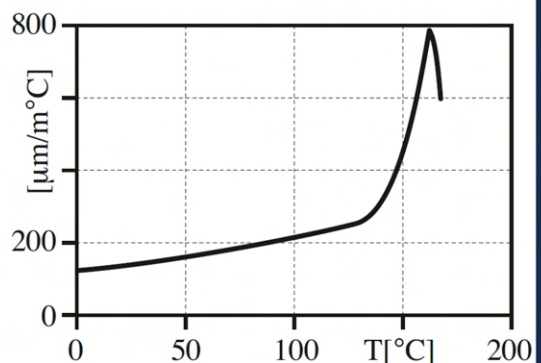
PEEK – Polyetheretherketone

Microstructure: semi-crystalline, amorphous
(~ 35 %)

Characteristics: high strength and stiffness, high resistance to temperature and chemicals, low susceptibility to stress cracking (except Acetone), complete mixability with PEI

Identified by: opaque, flame retardant, low smoke formation, faint phenol smell

Parameters:

ρ $= 1.32 \frac{g}{cm^3}$ *semicrystalline*
$1.27 \frac{g}{cm^3}$ *amorphous*
E $= 3700$ MPa
σ_s $= 100$ MPa
ε_s $= 5\,\%$
ε_B $= > 50\,\%$
T_g $= 145\,°C$
T_m $= 335\,°C$

Operational limits:
$T_{max}^{long\ term}$ ~ $250\,°C$
$T_{max}^{short\ term}$ ~ $300\,°C$

Chemical structure:
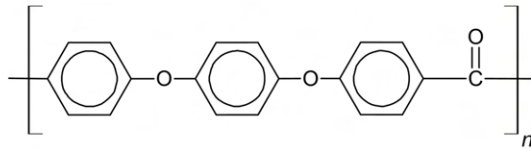
Blends:
PEI

σ– ε– Diagram:

Elastic modulus:

DSC–Diagram:

Coefficient of expansion:

Material card B.4.: General properties of polyetheretherketone [37].
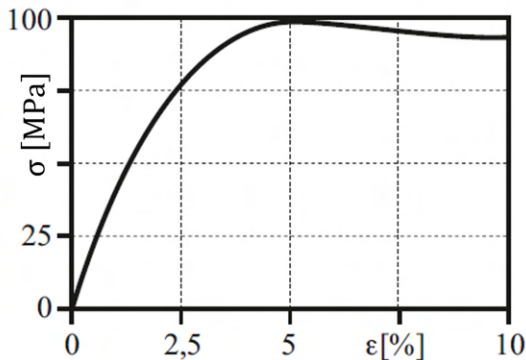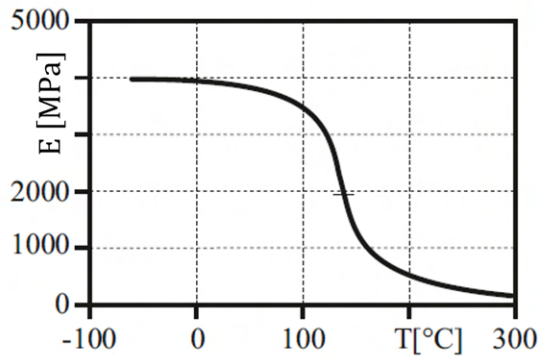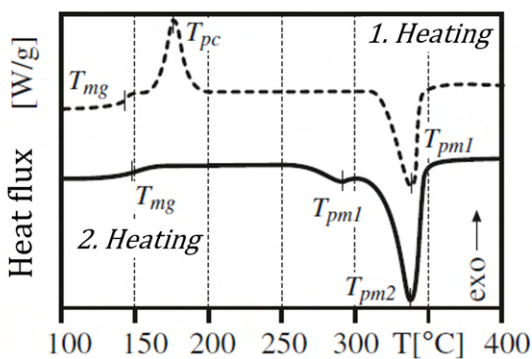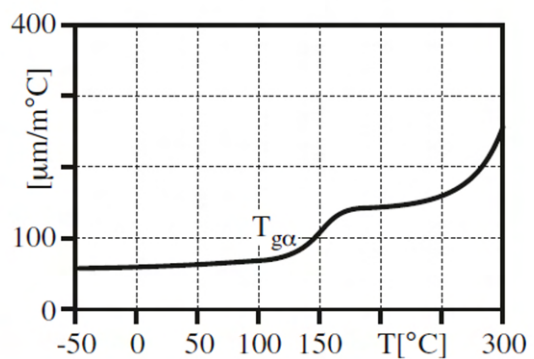
PTFE – Polytetrafluorethylene

Microstructure: semi-crystalline
(55 % - 90 %)

Characteristics: Highly resistant to chemicals, temperature and stress cracking, anti-adhesive, low wear resistance, high specific weight, prone to creep, sintered semifinished products, not suitable for injection molding

Identified by: milky white, opaque, non flammable, glowing with a blue-green flame

Parameters:

$\rho = 2.13 – 2.23 \, \frac{g}{cm^3}$
$E = 400 – 750 \, \text{MPa}$
$\sigma_s = 20 – 40 \, \text{MPa}$
$\varepsilon_B = > 50 \, \%$
$T_g = 125 – 1300 \, °C$
$T_m = 325 – 330 \, °C$

Operational limits:

$T_{max}^{long\ term} \sim 240 \, °C$
$T_{max}^{short\ term} \sim 280 \, °C$

Chemical structure:

σ– ε– Diagram:

Elastic modulus:

DSC–Diagram:

Coefficient of expansion:

Material card B.5.: General properties of poly(tetrafluoroethylene) [37].
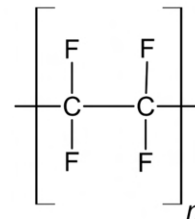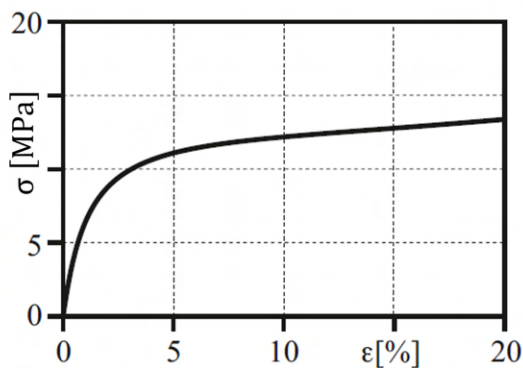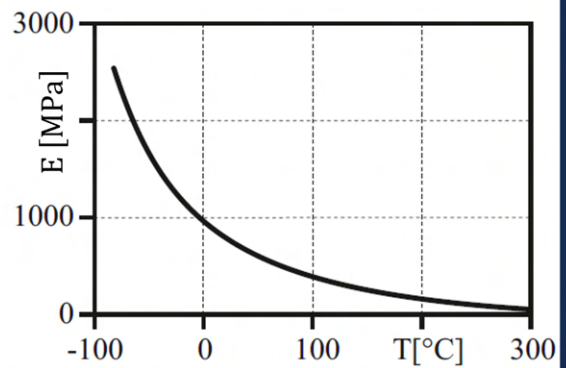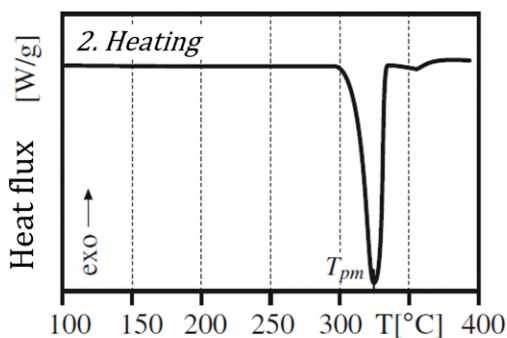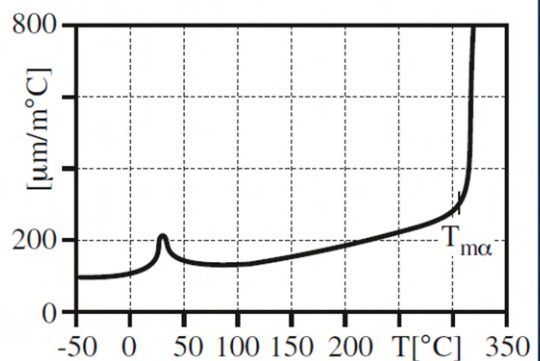
Appendix C.

Magnetic Properties of Materials

C.1. Magnetic Properties of Pristine Materials

Table C.1.: Magnetic parameters of the pristine magnetic materials according to the supplier.

Material	$\mathbf{H_{cJ}}[\mathrm{kA/m}]$	$\mathbf{H_{cB}}[\mathrm{kA/m}]$	$\mathbf{B_r}[\mathrm{mT}]$	$\mathbf{BH_{max}}[\mathrm{kJ/m^3}]$
AlNiCo 3	40	38	650	10
AlNiCo 5	52–54	50	1100–1250	34–44
AlNiCo 8	112–117	110–115	800–900	38–44
Y35 Ferrit	180–200	175–195	400–410	30–32

C.2. Evolution of Magnetic Properties During HPT

C.2.1. Y35 M-Type Hexaferrite
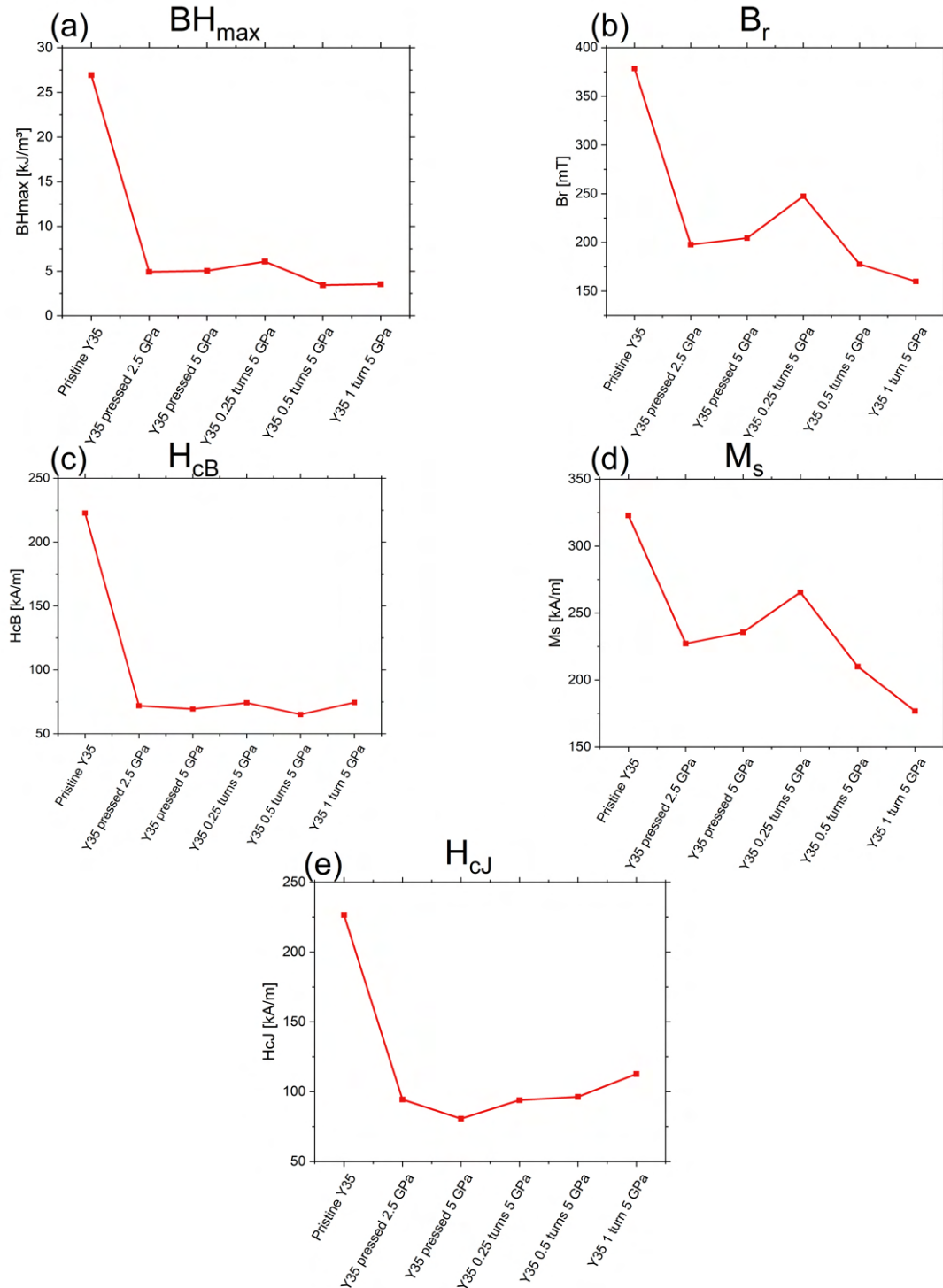
Figure C.1.: Evolution of Magnetic parameters of Y35, deformed by HPT: BH_{max}(a), B_r(b), H_{cB}(c), M_s(d), H_{cJ}(e).

C.2.2. AlNiCo Magnets
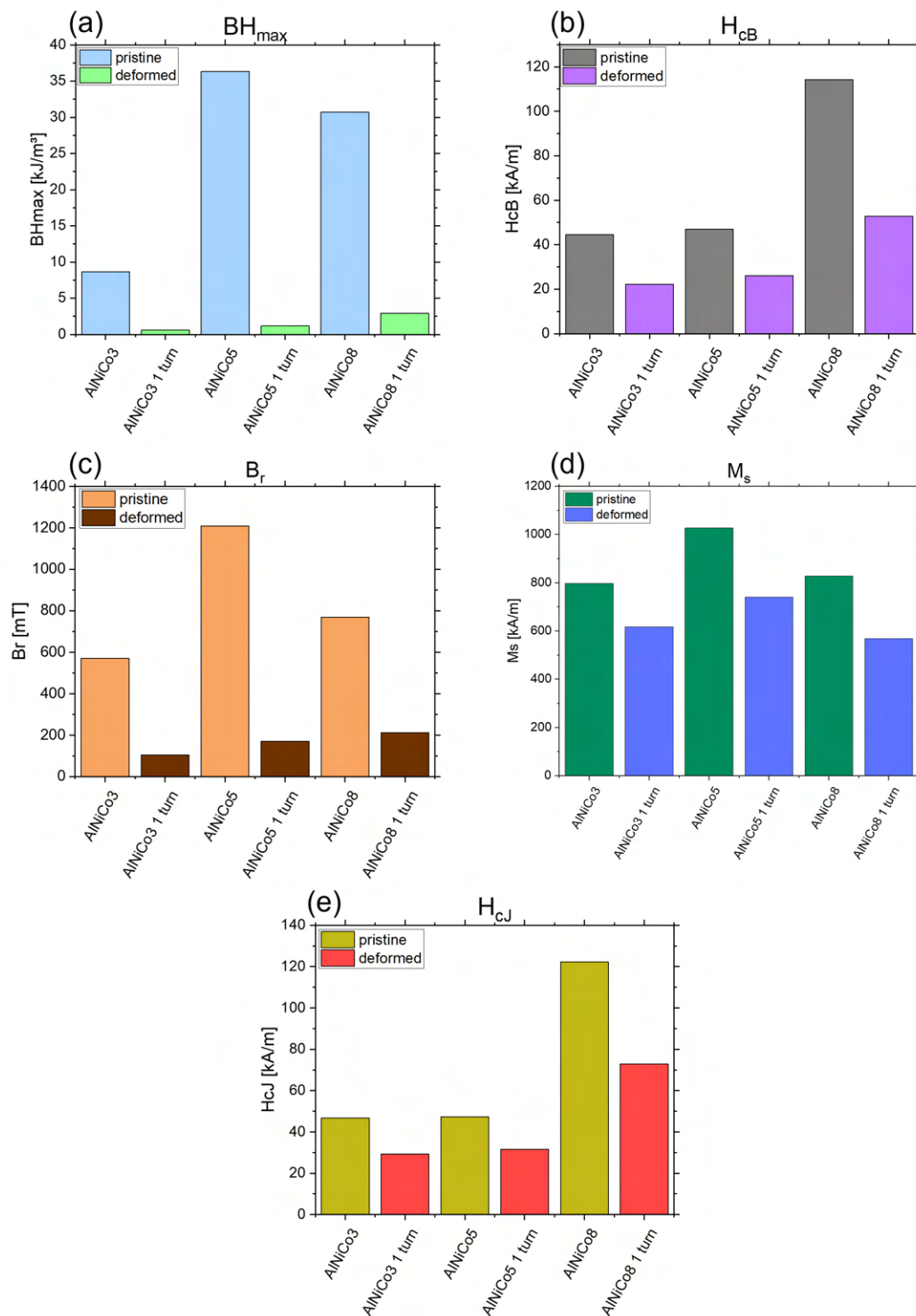
Figure C.2.: Evolution of magnetic parameters of AlNiCo deformed by HPT: BH_{max}(a), B_r(b), H_{cB}(c), M_s(d), H_{cJ}(e).

C.2.3. SrFe$_{12}$O$_{19}$ Powder Composites
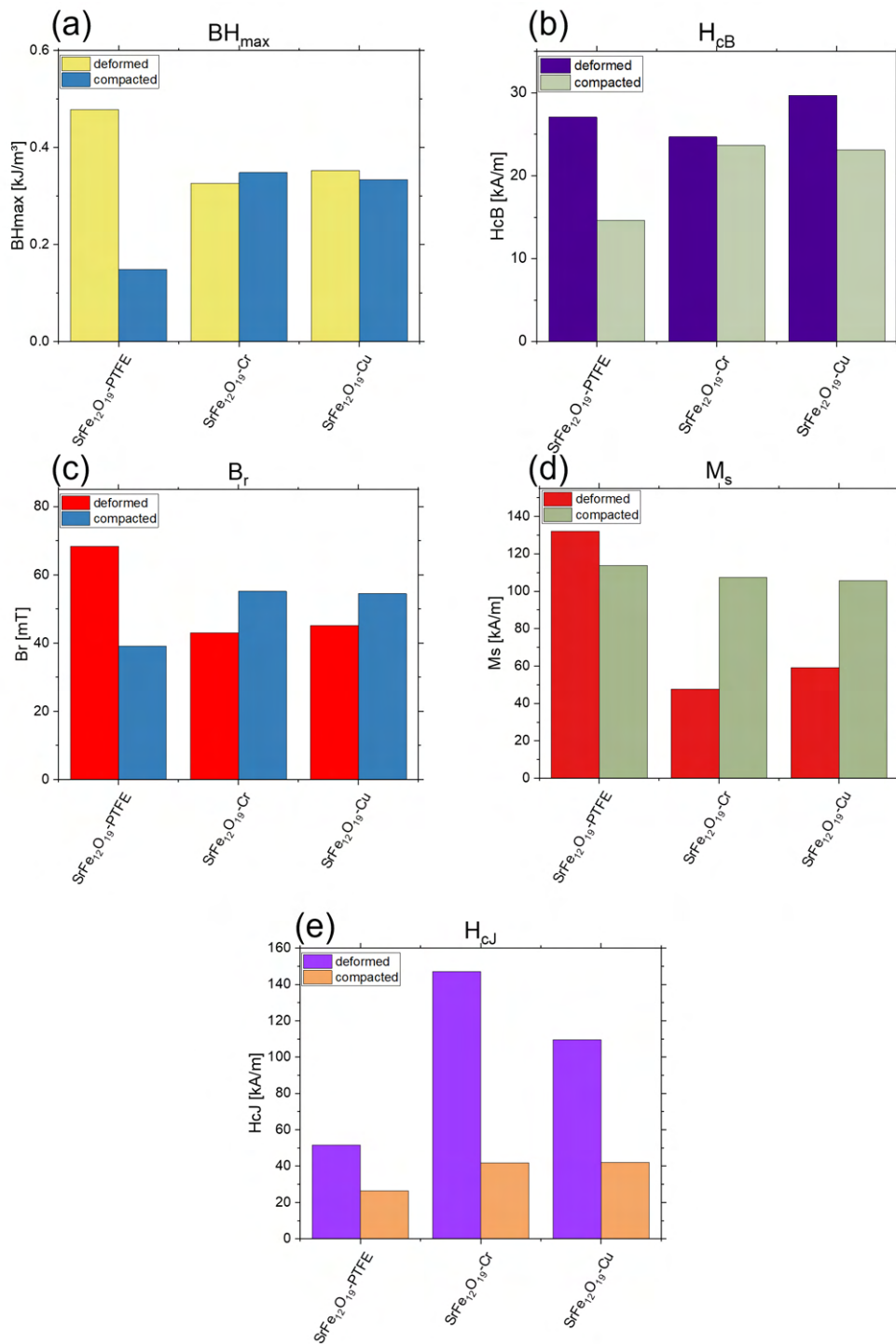
Figure C.3.: Evolution of magnetic parameters of powder composites pressed and deformed by HPT: BH$_{max}$(a), B$_r$(b), H$_{cB}$(c), M$_s$(d), H$_{cJ}$(e).

Appendix D.

XRD Analysis of Studied Materials

D.1. Polymers
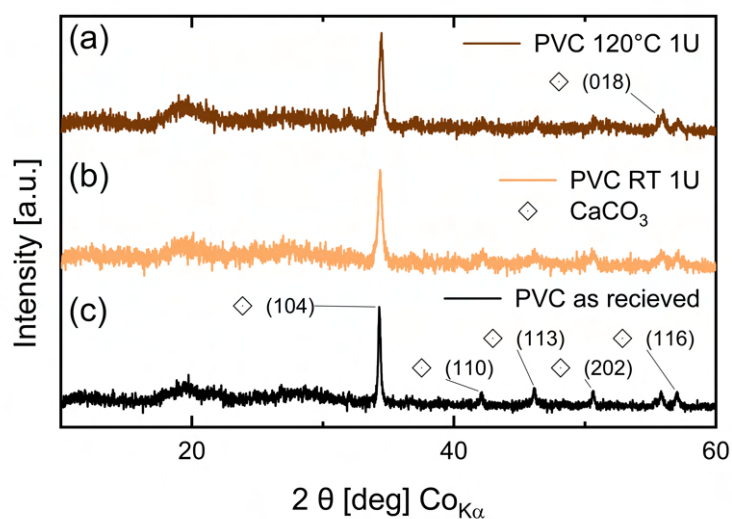
Figure D.1.: XRD pattern of PVC: deformed for 1 revolution at 120 °C and 1 GPa (a), deformed at RT for 1 revolution and 1 GPa (b) and pristine (c). XRD peaks from inorganic filler (CaCo$_3$) indexed using data from Kontoyannis et al [177].
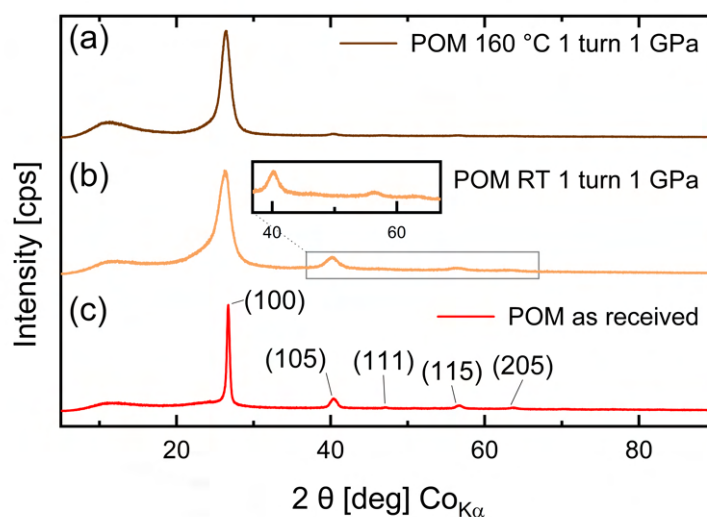
Figure D.2.: XRD pattern of POM: deformed for 1 revolution at 160 °C and 1 GPa (a), deformed at RT for 1 revolution and 1 GPa (b) and pristine (c). Indexed using data from Clark [102].
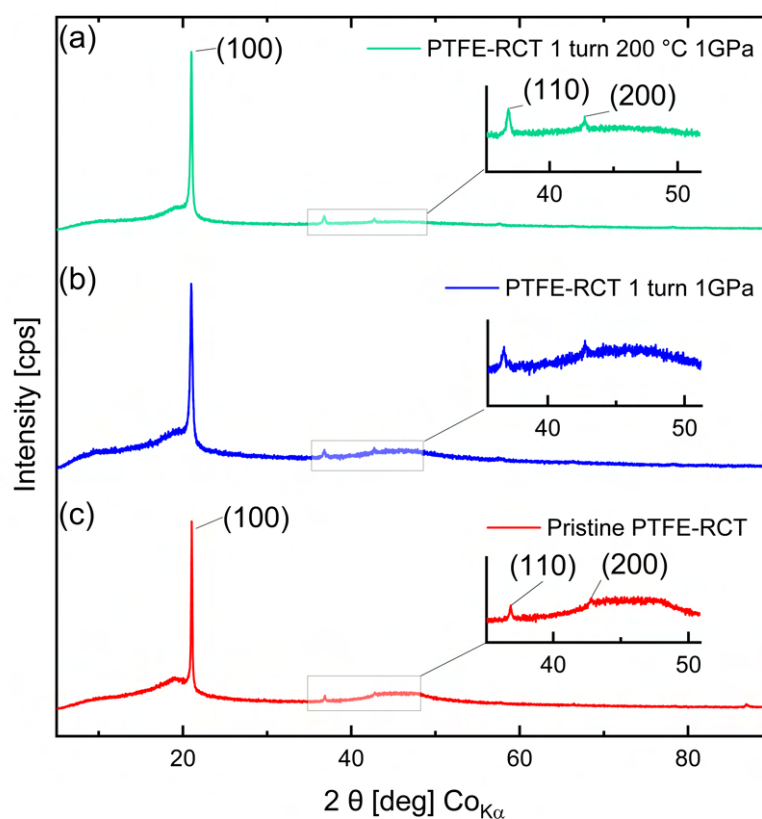
Figure D.3.: XRD pattern of PTFE: deformed for 1 revolution at 160 °C and 1 GPa (a), deformed at RT for 1 revolution and 1 GPa (b) and pristine (c). Indexed using data from Clark [102].
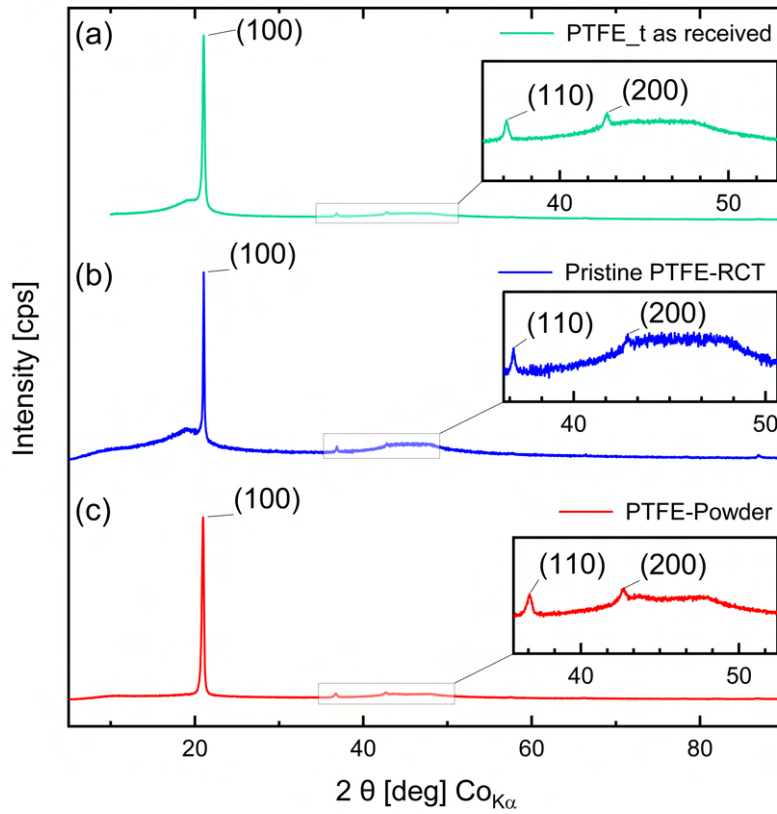
Figure D.4.: XRD pattern of all three used PTFE grades: PTFE provided by the in-house workshop (a), PTFE (THOMAPLAST $^{®}$) provided by Reichelt Chemietechnik GMbH + Co. (b), and PTFE powder provided by Sigma-Aldrich (c). Indexed using data from Clark [102].

D.2. Y35 Hexaferrite
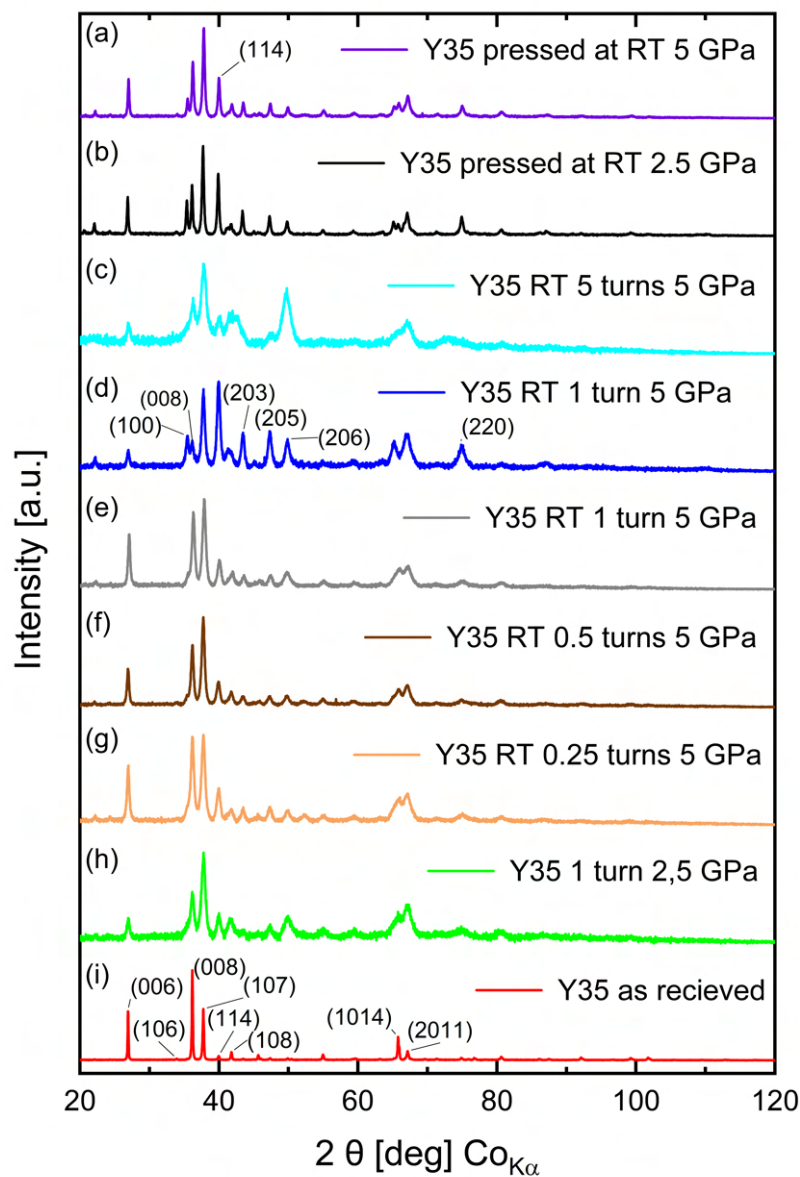
Figure D.5.: XRD pattern of pressed and deformed Y35-ferrites: pressed with 5 GPa (a), pressed with 5 GPa (b), deformed at 5 GPa for 5 revolutions (c), deformed at 5 GPa for 1 revolution (sample Y35_002) (d), deformed at 5 GPa for 1 revolution (sample Y35_011) (e), deformed at 5 GPa for 0.5 revolutions (f), deformed at 5 GPa for 0.25 revolutions (g), deformed at 2.5 GPa for 1 revolution (h) and the pristine commercial Y35-ferrite (i). Indexed using data from Obradors et al. [76] and Rahman et al. [105].
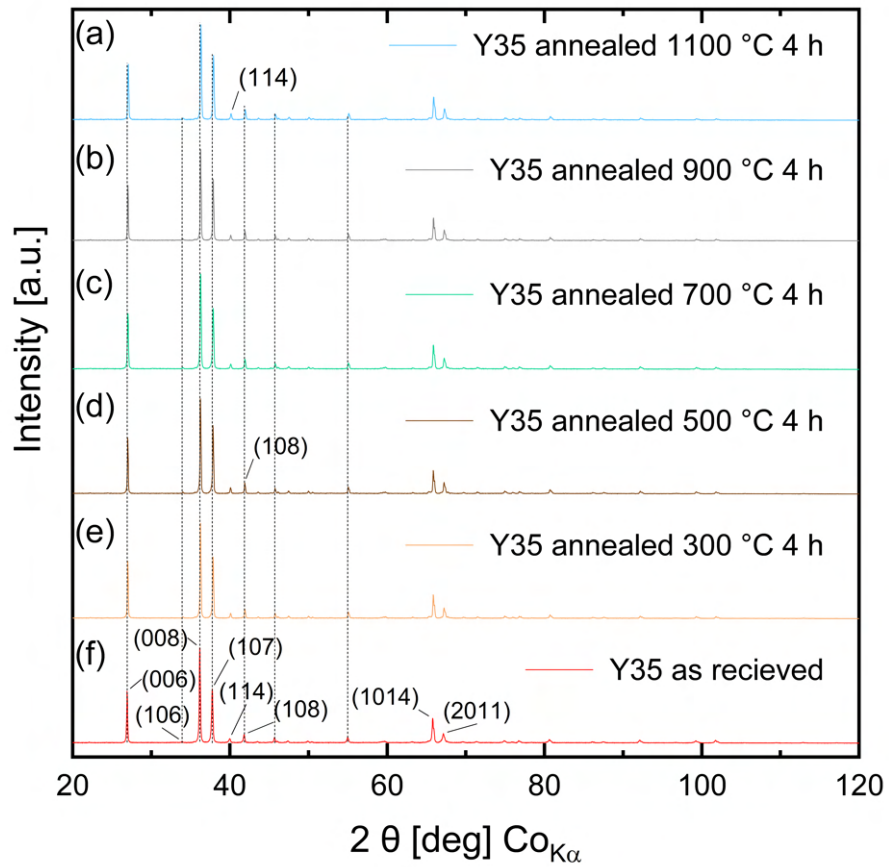
Figure D.6.: XRD pattern of annealed Y35 for 4 h at 1100 °C (a), 900 °C (b), 700 °C (c), 500 °C (d), 300 °C (e) and the pristine Y35- ferrite (f). Indexed using data from Obradors et al. [76] and Rahman et al. [105].

D.3. AlNiCo

For the indexing of measured data, peak positions are approximated using crystallographic data of AlNi (ICSD-151386) [178], and FeCo (ICSD-155839) [179]. The pattern of $AlFe_2Ni$ (ICSD-57808) [180], shows a approximation for peaks of Co-free AlNiCo before spinodal decomposition. After the spinodal decomposition, the α_1 and α_2 phases have a bcc structure [81, 83]. According to this, the 1st peak in the pattern of AlNiCo 3 and AlNiCo 8 is the $(1\,0\,0)$ peak followed by the $(1\,1\,0)$ peak. The $(1\,1\,0)$ peak is the peak with the highest intensity for all three AlNiCo grades.
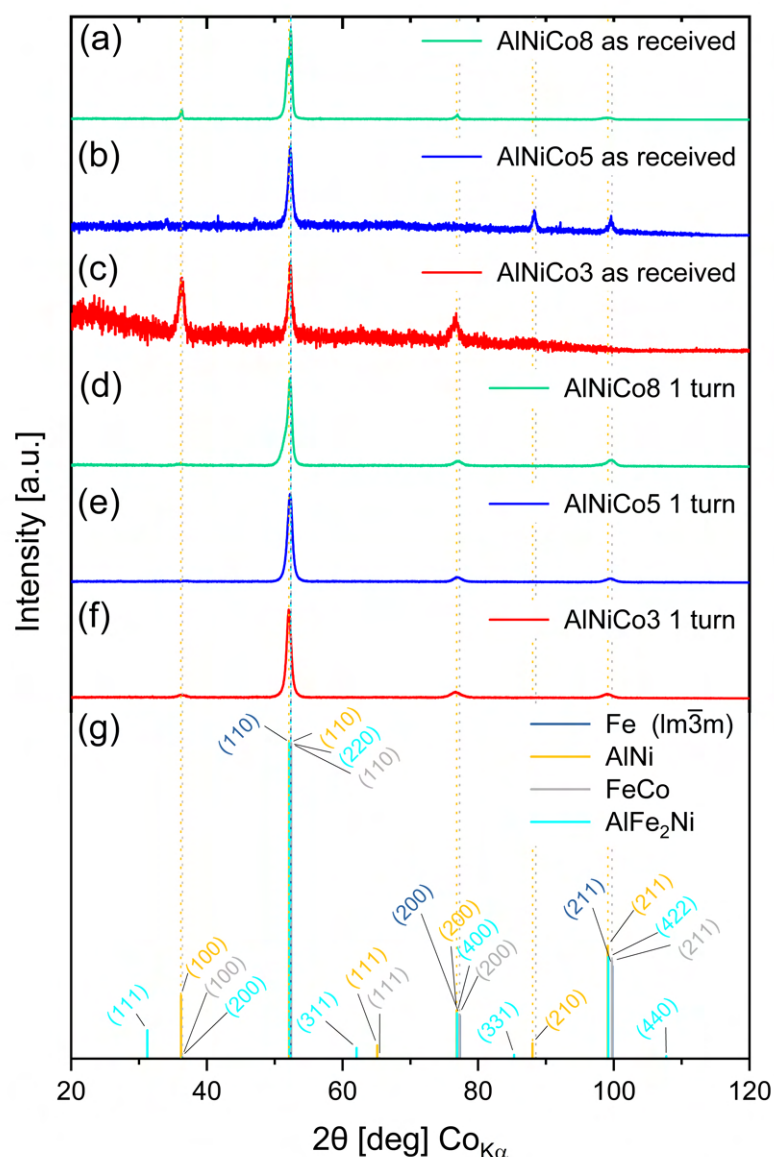
Figure D.7.: XRD pattern of AlNiCo: pristine AlNiCo 8 (a), pristine AlNiCo 5 (b), pristine AlNiCo 3 (c), AlNiCo 8 deformed at RT and 5 GPa (d), AlNiCo 5 deformed at RT an 5 GPa (e), AlNiCo 3 deformed at RT an 5 GPa (f), reference patterns calculated using the VESTA software [54] for Fe (amcsd 0011214) [181], AlNi [178], FeCo [179], $AlFe_2Ni$ [180] (g).

In Contrast to the indexed XRD data depicted above, Zhao et al. [182] and Rehman et al. [183] suggest a different sequence in position of the α_1 and α_2 phase, as shown in figure D.8.
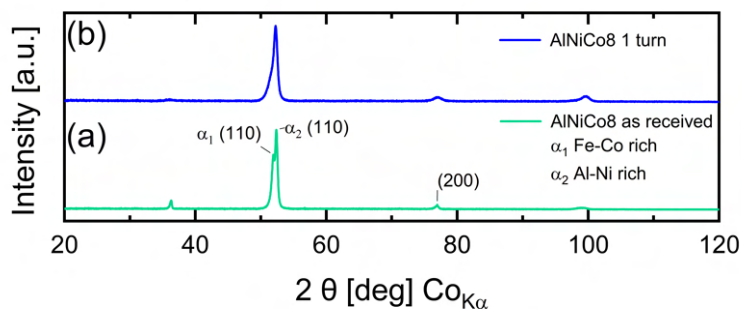
Figure D.8.: XRD pattern of AlNiCo 8: deformed at RT and 5 GPa for 1 revolution (a), and pristine (b).

[H]

D.4. Powder Composites
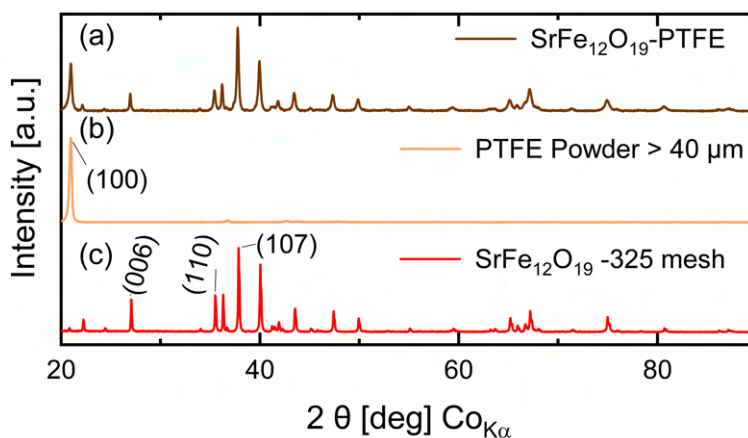
Figure D.9.: XRD pattern of pressed $SrFe_{12}O_{19}$-PTFE (a) powder composites and pure powders, PTFE (b) and $SrFe_{12}O_{19}$ (c). PTFE indexed according to data from Clark [102]. $SrFe_{12}O_{19}$ indexed according to data from Obradors et al. (OCD-1006000) [76] and Kimura et al. (ICSD-69022) [184].
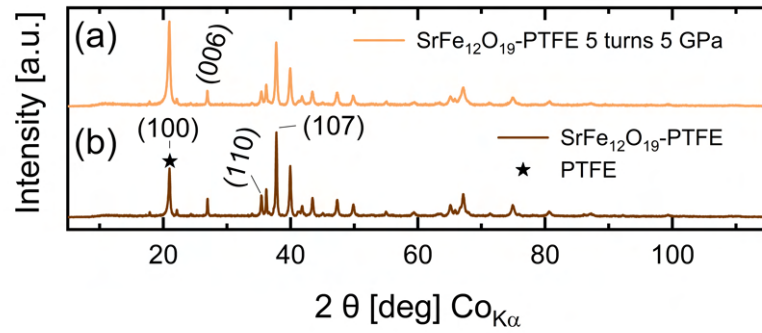
Figure D.10.: XRD pattern of deformed (a) and pressed (b) SrFe$_{12}$O$_{19}$-PTFE powder composites.
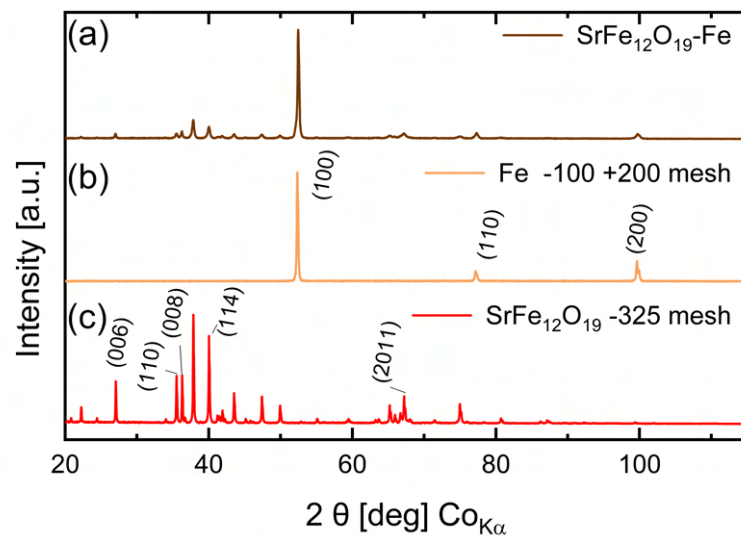
Figure D.11.: XRD pattern of pressed SrFe$_{12}$O$_{19}$-Fe (a) powder composites and pure powders, Fe (b) and SrFe$_{12}$O$_{19}$ (c). Fe indexed according to data from Wyckoff [181]. SrFe$_{12}$O$_{19}$ indexed according to data from Obradors et al. [76] and Kimura et al. [184].
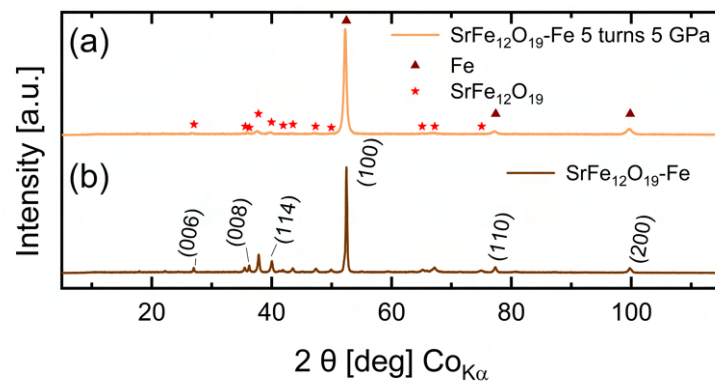
Figure D.12.: XRD pattern of deformed (a) and pressed (b) SrFe$_{12}$O$_{19}$-Fe powder composites.
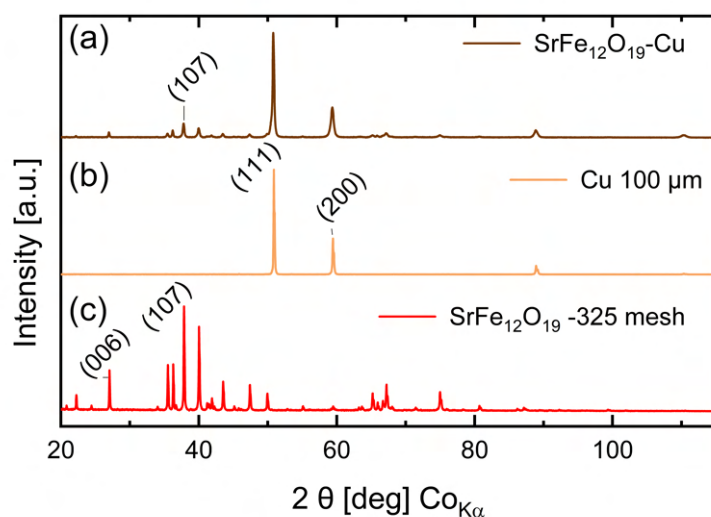
Figure D.13.: XRD pattern of pressed $SrFe_{12}O_{19}$-Cu (a) powder composites and pure powders, Cu (b) and $SrFe_{12}O_{19}$ (c). Cu indexed according to data from Bragg [185] and Wyckoff [181]. $SrFe_{12}O_{19}$ indexed according to data from Obradors et al. [76] and Kimura et al. [184].
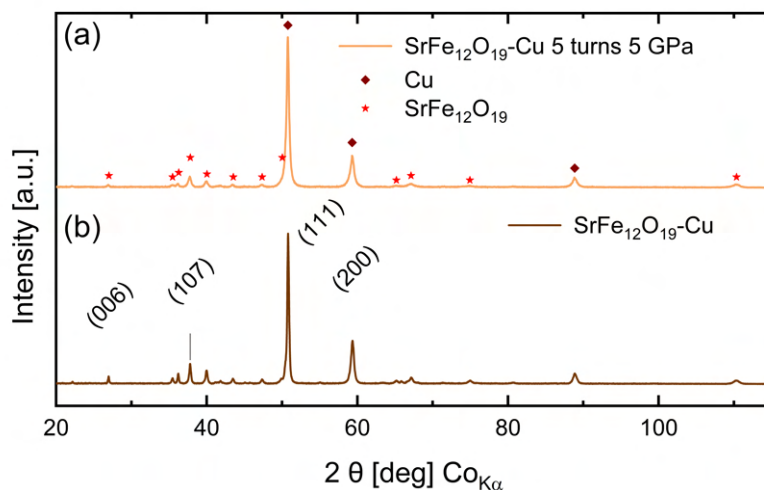
Figure D.14.: XRD pattern of deformed (a) and pressed (b) $SrFe_{12}O_{19}$-Cu powder composites.
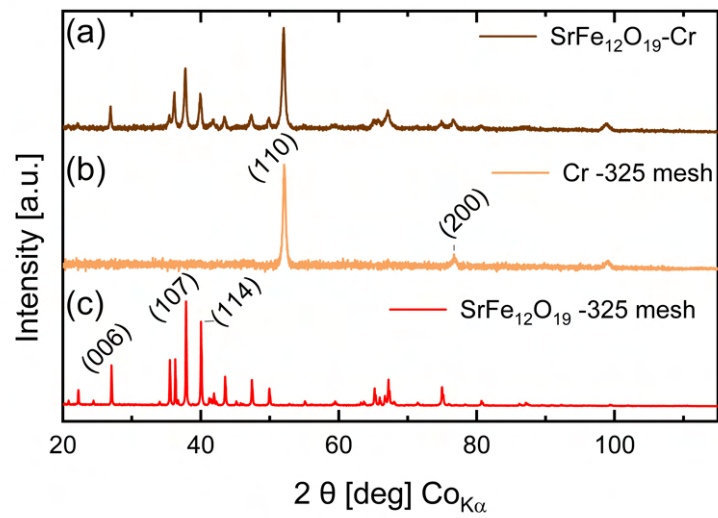
Figure D.15.: XRD pattern of pressed SrFe$_{12}$O$_{19}$-Cr (a) powder composites and pure powders, Cr (b) and SrFe$_{12}$O$_{19}$ (c). Cr in bcc configuration (Im3m), indexed according to data from Wyckoff [181]. SrFe$_{12}$O$_{19}$ indexed according to data from Obradors et al. [76] and Kimura et al. [184].
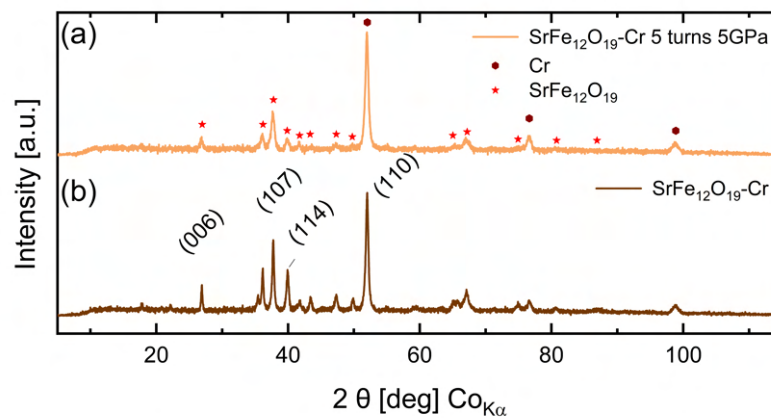
Figure D.16.: XRD pattern of deformed (a) and pressed (b) SrFe$_{12}$O$_{19}$-Cu powder composites. Cr in bcc configuration (Im$\bar{3}$m), indexed according to data from Wyckoff [181].

Appendix E.

EDX Analysis of Y35 Hexaferrites

EDX analysis of the commercial Y35-ferrite reveals the presence of metallic impurities. Especially the elements: Ca, Al and Ba have an influence on the magnetic properties. Since these elements can substitute Sr or Fe in the unit cell. This substitution is supported by the uniform distribution of Sr, Ca, Ba, and Al, shown in figure E.2 [77, 186]. The EDX spectrum is given in figure E.1.
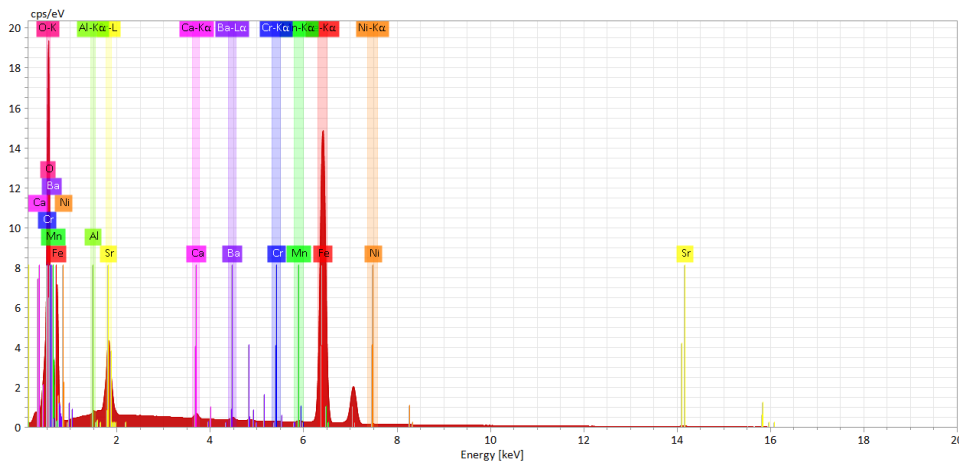
Figure E.1.: EDX analysis of commercial Y35 hexaferrite.
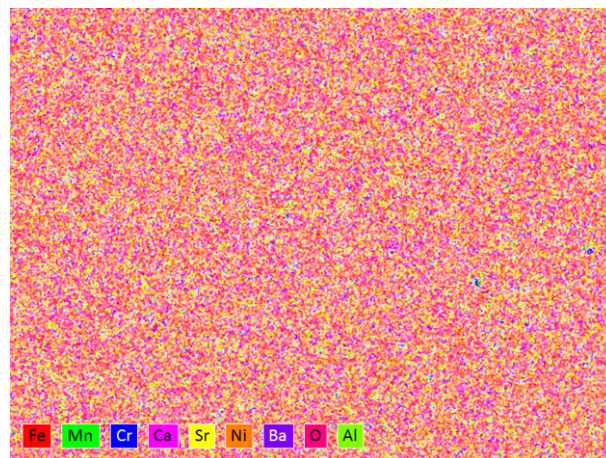
Figure E.2.: EDX mapping of elements in commercial Y35 hexaferrite.

Appendix F.

Additional Data on Deformed Powder Composites
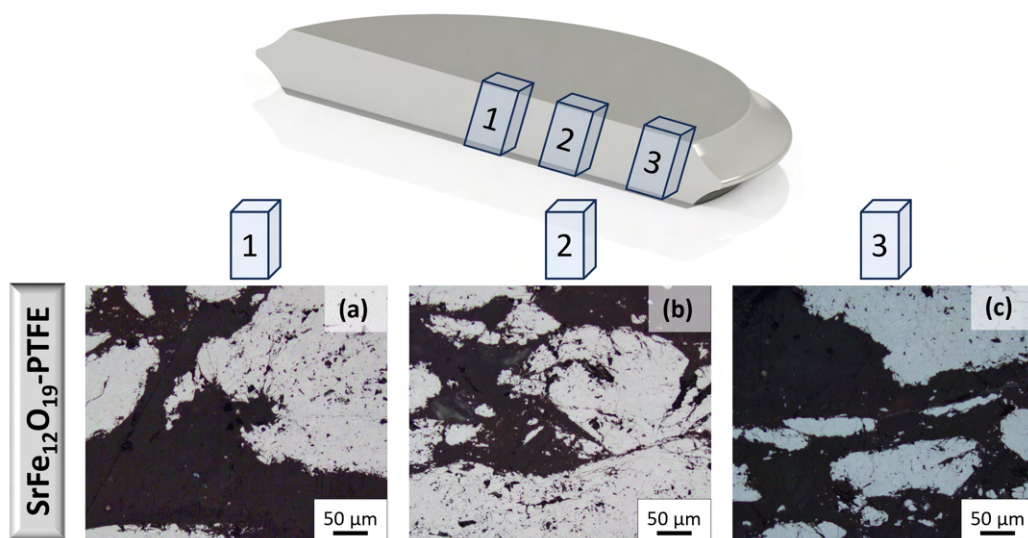
Figure F.1.: Optical micrographs of the PTFE powder composite at the radial positions of $0\,\text{mm}$ (a) $1.5\,\text{mm}$ (b) and $3.5\,\text{mm}$ (c).
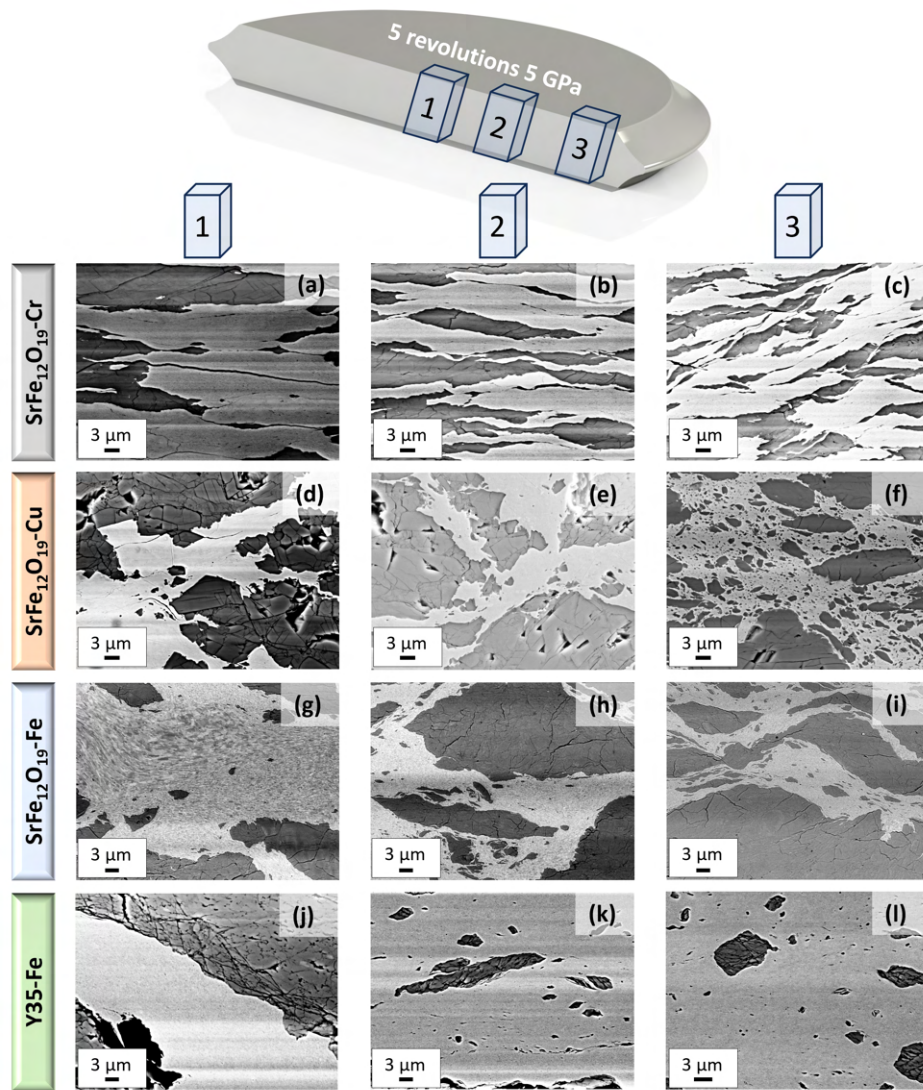
Figure F.2.: BSE image of gradient microstructure in radial direction of $SrFe_{12}O_{19}$-M powder composites. Microstructure at radial position $0.5\,mm$ $SrFe_{12}O_{19}$-Cr (a), at radial position $1.5\,mm$ $SrFe_{12}O_{19}$-Cr (b), at radial position $3.5\,mm$ $SrFe_{12}O_{19}$-Cr (c), at radial position $0\,mm$ $SrFe_{12}O_{19}$-Cu (d), at radial position $1.5\,mm$ $SrFe_{12}O_{19}$-Cu (e), at radial position $3.5\,mm$ $SrFe_{12}O_{19}$-Cu (f), at radial position $0\,mm$ $SrFe_{12}O_{19}$-Fe (g), at radial position $1.5\,mm$ $SrFe_{12}O_{19}$-Fe (h), at radial position $3.5\,mm$ $SrFe_{12}O_{19}$-Fe (i), reference images of Y35-Fe sample using ¼ segments at al radial positions respectively (j-l).

Bibliography

[1] J. M. D. Coey. "History of Magnetism and Basic Concepts." In: *Handbook of Magnetism and Magnetic Materials*. Ed. by J. M. D. Coey and S. S. P. Parkin. Cham: Springer International Publishing, 2021, pp. 3–51. ISBN: 978-3-030-63208-3. DOI: 10.1007/978-3-030-63210-6_1.

[2] B. D. Cullity and C. D. Graham. *Introduction to magnetic materials*. 2nd edition. Piscataway, NJ and Hoboken, NJ: IEEE Press and Wiley, 2009. ISBN: 978-0-471-47741-9.

[3] L. Masisi, M. Ibrahim, and P. Pillay. "Control strategy of a variable flux machine using AlNiCo permanent magnets." In: *2015 IEEE Energy Conversion Congress and Exposition (ECCE 2015)*. Ed. by Institute of Electrical and Electronics Engineers. Piscataway, NJ: IEEE, 2015, pp. 5249–5255. ISBN: 978-1-4673-7151-3. DOI: 10.1109/ECCE.2015.7310398.

[4] E. Schmidt, M. Kaltenbacher, and A. Wolfschluckner. "Eddy current losses in permanent magnets of surface mounted permanent magnet synchronous machines—Analytical calculation and high order finite element analyses." In: *e & i Elektrotechnik und Informationstechnik* 134.2 (2017), pp. 148–155. DOI: 10.1007/s00502-017-0498-y.

[5] B. Slusarek et al. "Synchronous motor with hybrid permanent magnets on the rotor." In: *Sensors* 14.7 (2014), pp. 12425–12436. DOI: 10.3390/s140712425.

[6] M. Ibrahim, L. Masisi, and P. Pillay. "Design of Variable-Flux Permanent-Magnet Machines Using Alnico Magnets." In: *IEEE Transactions on Industry Applications* 51.6 (2015), pp. 4482–4491. ISSN: 0093-9994. DOI: 10.1109/TIA.2015.2461621.

[7] A. Hohenwarter. "Microstructure, strength and fracture toughness of CuNb nanocomposites processed with high pressure torsion using multi-sector disks." In: *Scripta Materialia* 189 (2020), pp. 48–52. ISSN: 13596462. DOI: 10.1016/j.scriptamat.2020.07.061.

[8] S. Blundell. *Magnetism in condensed matter*. 1. publ. Vol. 4. Oxford master series in physics Oxford master series in condensed matter physics. Oxford: Oxford Univ. Press, 2001. ISBN: 978-0-19-850591-4.

[9] R. Skomski. "Magnetic Exchange Interactions." In: *Handbook of Magnetism and Magnetic Materials*. Ed. by J. M. D. Coey and S. S. P. Parkin. Cham: Springer International Publishing, 2021, pp. 53–102. ISBN: 978-3-030-63208-3. DOI: 10.1007/978-3-030-63210-6_2.

[10] E. P. Furlani. *Permanent magnet and electromechanical devices: Materials, analysis, and applications*. Series in electromagnetism. San Diego, Calif.: Acad. Press, 2001. ISBN: 0-12-269951-3. DOI: 89410.

[11] L. Weissitsch et al. "Magnetic Materials via High-Pressure Torsion of Powders." In: *Materials Transactions* 64.7 (2023), pp. 1537–1550. ISSN: 1345-9678. DOI: 10.2320/matertrans.MT-MF2022026.

[12] D. Goll and H. Kronmüller. "High-performance permanent magnets." In: *Die Naturwissenschaften* 87.10 (2000), pp. 423–438. ISSN: 0028-1042. DOI: 10.1007/s001140050755.

[13] Th. Bapu. "DC Hysteresigraphs for Hard and Soft Materials." In: *Magnetic Measurement Techniques for Materials Characterization*. Ed. by V. Franco and B. Dodrill. Springer eBook Collection. Cham: Springer International Publishing and Imprint Springer, 2021, pp. 91–117. ISBN: 978-3-030-70442-1. DOI: 10.1007/978-3-030-70443-8_5.

[14] A. K. Higgins et al. "Apparent Image Effect in Closed-Circuit Magnetic Measurements." In: *IEEE Transactions on Magnetics* 44.11 (2008), pp. 3269–3272. ISSN: 0018-9464. DOI: 10.1109/TMAG.2008.2002388.

[15] C. H. Chen, A. K. Higgins, and R. M. Strnat. "Effect of geometry on magnetization distortion in closed-circuit magnetic measurements." In: *Journal of Magnetism and Magnetic Materials* 320.9 (2008), pp. L84–L87. ISSN: 03048853. DOI: 10.1016/j.jmmm.2008.01.035.

[16] C. H. Chen et al. "Verification by finite element modeling for the origin of the apparent image effect in closed-circuit magnetic measurements." In: *Journal of Magnetism and Magnetic Materials* 323.1 (2011), pp. 108–114. ISSN: 03048853. DOI: 10.1016/j.jmmm.2010.08.042.

[17] R. Skomski. "Permanent Magnets: History, Current Research, and Outlook." In: *Novel Functional Magnetic Materials*. Ed. by A. Zhukov. Vol. 231. Cham: Springer International Publishing, 2016, pp. 359–395. ISBN: 978-3-319-26104-1. DOI: 10.1007/978-3-319-26106-5_9.

[18] R. Skomski and J. M. D. Coey. "Magnetic anisotropy — How much is enough for a permanent magnet?" In: *Scripta Materialia* 112 (2016), pp. 3–8. ISSN: 13596462. DOI: 10.1016/j.scriptamat.2015.09.021.

[19] O. Gutfleisch. "Controlling the properties of high energy density permanent magnetic materials by different processing routes." In: *Journal of Physics D: Applied Physics* 33.17 (2000), R157–R172. ISSN: 0022-3727. DOI: 10.1088/0022-3727/33/17/201.

[20] M. R. Notis. "Deformation Mechanism Maps — A Review with Applications." In: *Deformation of Ceramic Materials*. Ed. by R. C. Bradt and R. E. Tressler. Boston, MA: Springer US, 1975, pp. 1–23. ISBN: 978-1-4613-4433-9. DOI: 10.1007/978-1-4613-4431-5_1.

[21] H. J. Frost and M. F. Ashby. "Deformation-Mechanism Maps for Pure Iron, Two Austenitic Stainless Steels, and a Low-Alloy Ferritic Steel." In: *Fundamental Aspects of Structural Alloy Design*. Ed. by R. I. Jaffee and B. A. Wilcox. Boston, MA: Springer US, 1977, pp. 27–65. ISBN: 978-1-4684-2423-2. DOI: 10.1007/978-1-4684-2421-8_2.

[22] W. D. Callister and D. G. Rethwisch. *Materials science and engineering: An introduction*. 10th edition. Hoboken, NJ: John Wiley & Sons, Inc, 2018. ISBN: 9781119321590.

[23] U. Messerschmidt. *Dislocation dynamics during plastic deformation*. 1st edition. Vol. 129. Springer series in materials science. Berlin and Heidelberg: Springer, 2010. ISBN: 978-3-642-03176-2. DOI: 10.1007/978-3-642-03177-9.

[24] S. C. Baik et al. "Modeling of Deformation Behavior and Texture Development in Aluminium under Equal Channel Angular Pressing." In: *Nanomaterials by Severe Plastic Deformation*. Ed. by M. J. Zehetbauer and R. Z. Valiev. Weinheim: WILEY-VCH Verlag GmbH & Co. KGaA, 2004, pp. 233–238. ISBN: 9783527602469. DOI: 10.1002/3527602461.ch4c.

[25] M. Cabibbo and E. Evangelista. "Deformation Mechanisms Inducing Microstructure Refinement in Commercially Pure Aluminium Processed via ECAP: Comparison to Cold-Rolling and Hot-Torsion." In: *Nanostructured materials by high-pressure severe plastic deformation*. Ed. by Yuntian T. Zhu and V. N. Varyukhin. Vol. 212. NATO science series 2, Mathematics, physics and chemistry. Dordrecht: Springer, 2006, pp. 193–198. ISBN: 978-1-4020-3923-2. DOI: 10.1007/1-4020-3923-9_27.

[26] A. A. Dubravina et al. "Deformation Behaviour of Copper Subjected to High Pressure Torsion." In: *Nanomaterials by Severe Plastic Deformation*. Ed. by M. J. Zehetbauer and R. Z. Valiev. Weinheim: WILEY-VCH Verlag GmbH & Co. KGaA, 2004, pp. 465–470. ISBN: 9783527602469. DOI: 10.1002/3527602461.ch8e.

[27] M. Kawasaki and T. G. Langdon. "The many facets of deformation mechanism mapping and the application to nanostructured materials." In: *Journal of Materials Research* 28.13 (2013), pp. 1827–1834. ISSN: 0884-2914. DOI: 10.1557/jmr.2013.55.

[28] A. A. Nazarov et al. "Modeling of Grain Subdivision during Severe Plastic Deformation by VPSC Method Combined with Disclination Analysis." In: *Nanostructured materials by high-pressure severe plastic deformation*. Ed. by Yuntian T. Zhu and V. N. Varyukhin. Vol. 212. NATO science series 2, Mathematics, physics and chemistry. Dordrecht: Springer, 2006, pp. 61–66. ISBN: 978-1-4020-3923-2. DOI: 10.1007/1-4020-3923-9_8.

[29] E. Macherauch and H. W. Zoch. *Praktikum in Werkstoffkunde*. Wiesbaden: Springer Fachmedien Wiesbaden, 2019. ISBN: 978-3-658-25373-8. DOI: 10.1007/978-3-658-25374-5.

[30] W. Bergmann. *Werkstofftechnik: Grundlagen und Anwendung*. 6., aktualisierte Aufl. München: Hanser, 2008. ISBN: 978-3-446-41338-2.

[31] E. Doege and B. A. Behrens. *Handbuch Umformtechnik: Grundlagen, Technologien, Maschinen*. 3. Aufl. 2016. VDI-Buch. Berlin, Heidelberg: Springer Berlin Heidelberg, 2016. ISBN: 978-3-662-43890-9. DOI: 10.1007/978-3-662-43891-6.

[32] H. Hoffmann, R. Neugebauer, and G. Spur. *Handbuch Umformen*. 2. Auflage. Handbuch der Fertigungstechnik. München: Hanser, 2011. ISBN: 978-3-446-43004-4.

[33] G. Y. Chin. "Slip and Twinning Systems in Ceramic Crystals." In: *Deformation of Ceramic Materials*. Ed. by R. C. Bradt and R. E. Tressler. Boston, MA: Springer US, 1975, pp. 25–59. ISBN: 978-1-4613-4433-9. DOI: 10.1007/978-1-4613-4431-5_2.

[34] A. G. Evans. "Thermally Activated Dislocation Motion in Ceramic Materials." In: *Deformation of Ceramic Materials*. Ed. by R. C. Bradt and R. E. Tressler. Boston, MA: Springer US, 1975, pp. 127–149. ISBN: 978-1-4613-4433-9. DOI: 10.1007/978-1-4613-4431-5_5.

[35] T. G. Langdon. "Grain Boundary Deformation Processes." In: *Deformation of Ceramic Materials*. Ed. by R. C. Bradt and R. E. Tressler. Boston, MA: Springer US, 1975, pp. 101–126. ISBN: 978-1-4613-4433-9. DOI: 10.1007/978-1-4613-4431-5_4.

[36] M. H. Hodge, W. R. Bitler, and R. C. Bradt. "Deformation Texture and Magnetic Properties of the Magnetoplumbite Ferrites." In: *Deformation of Ceramic Materials*. Ed. by R. C. Bradt and R. E. Tressler. Boston, MA: Springer US, 1975, pp. 483–496. ISBN: 978-1-4613-4433-9. DOI: 10.1007/978-1-4613-4431-5_27.

[37] G. W. Ehrenstein. *Polymer-Werkstoffe: Struktur - Eigenschaften - Anwendung*. 3. Auflage. München: Hanser, 2011. ISBN: 978-3-446-42967-3.

[38] A. S. Argon. "A theory for the low-temperature plastic deformation of glassy polymers." In: *Philosophical Magazine* 28.4 (1973), pp. 839–865. ISSN: 0031-8086. DOI: 10.1080/14786437308220987.

[39] A. S. Argon. *The physics of deformation and fracture of polymers*. Cambridge Solid State Science Series. Cambridge: Cambridge University Press, 2013. ISBN: 9781139033046. DOI: 10.1017/CBO9781139033046.

[40] L. Lin and A. S. Argon. "Structure and plastic deformation of polyethylene." In: *Journal of materials science* 29.2 (1994), pp. 294–323. ISSN: 0022-2461. DOI: 10.1007/BF01162485.

[41] M. C. Boyce, D. M. Parks, and A. S. Argon. "Large inelastic deformation of glassy polymers. part I: rate dependent constitutive model." In: *Mechanics of Materials* 7.1 (1988), pp. 15–33. ISSN: 01676636. DOI: 10.1016/0167-6636(88)90003-8.

[42] M. C. Boyce, D. M. Parks, and A. S. Argon. "Large inelastic deformation of glassy polymers. Part II: numerical simulation of hydrostatic extrusion." In: *Mechanics of Materials* 7.1 (1988), pp. 35–47. ISSN: 01676636. DOI: 10.1016/0167-6636(88)90004-X.

[43] Z. Bartczak. "Effect of Chain Entanglements on Plastic Deformation Behavior of Linear Polyethylene." In: *Macromolecules* 38.18 (2005), pp. 7702–7713. ISSN: 0024-9297. DOI: 10.1021/ma050815y.

[44] Z. Bartczak and M. Kozanecki. "Influence of molecular parameters on high-strain deformation of polyethylene in the plane-strain compression. Part I. Stress–strain behavior." In: *Polymer* 46.19 (2005), pp. 8210–8221. ISSN: 00323861. DOI: 10.1016/j.polymer.2005.06.100.

[45] Z. Bartczak. "Influence of molecular parameters on high-strain deformation of polyethylene in the plane-strain compression. Part II. Strain recovery." In: *Polymer* 46.23 (2005), pp. 10339–10354. ISSN: 00323861. DOI: 10.1016/j.polymer.2005.07.096.

[46] P. Nikaeen et al. "Effect of plastic deformation on the nanomechanical properties of glassy polymers: An experimental study." In: *Mechanics of Materials* 159 (2021), p. 103900. ISSN: 01676636. DOI: 10.1016/j.mechmat.2021.103900.

[47] M. L. Falk. "Materials science. The flow of glass." In: *Science (New York, N.Y.)* 318.5858 (2007), pp. 1880–1881. DOI: 10.1126/science.1150919.

[48] S. Jabbari-Farouji et al. "Role of the Intercrystalline Tie Chains Network in the Mechanical Response of Semicrystalline Polymers." In: *Physical review letters* 118.21 (2017), p. 217802. DOI: 10.1103/PhysRevLett.118.217802.

[49] P. B. Bowden and R. J. Young. "Deformation mechanisms in crystalline polymers." In: *Journal of materials science* 9.12 (1974), pp. 2034–2051. ISSN: 0022-2461. DOI: 10.1007/BF00540553.

[50] Z. Bartczak and A. Galeski. "Plasticity of Semicrystalline Polymers." In: *Macromolecular Symposia* 294.1 (2010), pp. 67–90. ISSN: 1022-1360. DOI: 10.1002/masy.201050807.

[51] O. A. Hasan and M. C. Boyce. "A constitutive model for the nonlinear viscoelastic viscoplastic behavior of glassy polymers." In: *Polymer Engineering and Science* 35.4 (1995), pp. 331–344. ISSN: 0032-3888. DOI: 10.1002/pen.760350407.

[52] F. Detrez, S. Cantournet, and R. Séguéla. "A constitutive model for semicrystalline polymer deformation involving lamellar fragmentation." In: *Comptes Rendus Mécanique* 338.12 (2010), pp. 681–687. ISSN: 1631-0721. DOI: 10.1016/j.crme.2010.10.008.

[53] M. I. Okereke and A. I. Akpoyomare. "Two-process constitutive model for semicrystalline polymers across a wide range of strain rates." In: *Polymer* 183 (2019), p. 121818. ISSN: 00323861. DOI: 10.1016/j.polymer.2019.121818.

[54] K. Momma and F. Izumi. "VESTA 3 for three-dimensional visualization of crystal, volumetric and morphology data." In: *Journal of Applied Crystallography* 44.6 (2011), pp. 1272–1276. ISSN: 0021-8898. DOI: 10.1107/S0021889811038970.

[55] S. Geier et al. "Synthetische Kunststoffe." In: *Kunststoffe.* Ed. by P. Elsner, P. Eyerer, and T. Hirth. VDI-Buch. Dordrecht: Springer, 2011, pp. 115–1201. ISBN: 978-3-642-16172-8. DOI: 10.1007/978-3-642-16173-5_2.

[56] T. A. Osswald and G. Menges. *Material science of polymers for engineers.* 3d edition. Munich: Hanser, 2012. ISBN: 978-1-56990-524-1.

[57] W. Hellerich, G. Harsch, and E. Baur. *Werkstoff-Führer Kunststoffe: Eigenschaften, Prüfungen, Kennwerte.* 10. Auflage. München: Hanser, 2010. ISBN: 978-3-446-42436-4.

[58] H. Eitel. "Datenbanken." In: *Kunststoffe.* Ed. by P. Elsner, P. Eyerer, and T. Hirth. VDI-Buch. Dordrecht: Springer, 2011, pp. 1401–1405. ISBN: 978-3-642-16172-8. DOI: 10.1007/978-3-642-16173-5_6.

[59] W. Brostow. "Mechanical Properties." In: *Physical properties of polymers handbook.* Ed. by J. E. Mark. New York, NY: Springer Science+Business Media LLC, 2007, pp. 423–445. ISBN: 978-0-387-31235-4. DOI: 10.1007/978-0-387-69002-5_24.

[60] B. Sixou et al. "Mechanism of sintering of polyoxymethylene powders investigated by small-angle X-ray scattering." In: *e-Polymers* 7.1 (2007). ISSN: 2197-4586. DOI: 10.1515/epoly.2007.7.1.610.

[61] D. J. Kemmish and J. N. Hay. "The effect of physical ageing on the properties of amorphous PEEK." In: *Polymer* 26.6 (1985), pp. 905–912. ISSN: 00323861. DOI: 10.1016/0032-3861(85)90136-3.

[62] E. Papia, S. A. C. Brodde, and J. P. Becktor. "Deformation of polyetheretherketone, PEEK, with different thicknesses." In: *Journal of the mechanical behavior of biomedical materials* 125 (2022), p. 104928. DOI: 10.1016/j.jmbbm.2021.104928.

[63] E. S. Clark. "The molecular conformations of polytetrafluoroethylene: forms II and IV." In: *Polymer* 40.16 (1999), pp. 4659–4665. ISSN: 00323861. DOI: 10.1016/S0032-3861(99)00109-3.

[64] E. S. Clark. "The Crystal Structure of Polytetrafluoroethylene, Forms I and IV." In: *Journal of Macromolecular Science, Part B* 45.2 (2006), pp. 201–213. ISSN: 0022-2348. DOI: 10.1080/00222340500522265.

[65] G. Fatti et al. "First-Principles Insights into the Structural and Electronic Properties of Polytetrafluoroethylene in Its High-Pressure Phase (Form III)." In: *The Journal of Physical Chemistry C* 123.10 (2019), pp. 6250–6255. ISSN: 1932-7447. DOI: 10.1021/acs.jpcc.8b11631.

[66] E. N. Brown et al. "A new strain path to inducing phase transitions in semi-crystalline polymers." In: *Polymer* 48.9 (2007), pp. 2531–2536. ISSN: 00323861. DOI: 10.1016/j.polymer.2007.03.031.

[67] G. Gottstein. *Physikalische Grundlagen der Materialkunde: Mit 28 Tabellen*. 3. Aufl. Springer-Lehrbuch. Berlin and Heidelberg: Springer, 2007. ISBN: 978-3-540-71104-9.

[68] N. Lugo et al. "Microstructures and mechanical properties of pure copper deformed severely by equal-channel angular pressing and high pressure torsion." In: *Materials Science and Engineering: A* 477.1-2 (2008), pp. 366–371. ISSN: 09215093. DOI: 10.1016/j.msea.2007.05.083.

[69] M. Li and S. J. Zinkle. "Physical and Mechanical Properties of Copper and Copper Alloys." In: *Comprehensive nuclear materials*. Ed. by R. J. M. Konings et al. Elsevier, 2012, pp. 667–690. ISBN: 9780080560335. DOI: 10.1016/B978-0-08-056033-5.00122-1.

[70] U. Holzwarth and H. Stamm. "Mechanical and thermomechanical properties of commercially pure chromium and chromium alloys." In: *Journal of Nuclear Materials* 300.2-3 (2002), pp. 161–177. ISSN: 00223115. DOI: 10.1016/S0022-3115(01)00745-0.

[71] R. J. Meyer. *Chrom: Teil A - Lieferung 1. Geschichtliches · Vorkommen · Technologie · Element bis Physikalische Eigenschaften*. 8. Auflage. Vol. C-r / A / 1. Cr. Chrom. Chromium (System-Nr. 52). Berlin, Heidelberg and s.l.: Springer Berlin Heidelberg, 1962. ISBN: 978-3-662-11865-8. DOI: 10.1007/978-3-662-11864-1.

[72] E. S. Gorkunov et al. "The effects of deformations by rolling and uniaxial tension on the structure and the magnetic and mechanical properties of armco iron, steel 12X18H10T, and a steel 12X18H10T-Armco Iron-Steel 12X18H10T composite material." In: *Russian Journal of Nondestructive Testing* 47.6 (2011), pp. 369–380. ISSN: 1061-8309. DOI: 10.1134/S1061830911060076.

[73] J. A. Benito et al. "Change of Young's modulus of cold-deformed pure iron in a tensile test." In: *Metallurgical and Materials Transactions A* 36.12 (2005), pp. 3317–3324. ISSN: 1073-5623. DOI: 10.1007/s11661-005-0006-6.

[74] R. W. McCallum et al. "Practical Aspects of Modern and Future Permanent Magnets." In: *Annual Review of Materials Research* 44.1 (2014), pp. 451–477. ISSN: 1531-7331. DOI: 10.1146/annurev-matsci-070813-113457.

[75] G. D. Soria et al. "Strontium hexaferrite platelets: a comprehensive soft X-ray absorption and Mössbauer spectroscopy study." In: *Scientific reports* 9.1 (2019), p. 11777. DOI: 10.1038/s41598-019-48010-w.

[76] X. Obradors et al. "Crystal structure of strontium hexaferrite SrFe12O19." In: *Journal of Solid State Chemistry* 72.2 (1988), pp. 218–224. ISSN: 00224596. DOI: 10.1016/0022-4596(88)90025-4.

[77] L. Wang et al. "Effects of Al and Ca ions co-doping on magnetic properties of M-type strontium ferrites." In: *Journal of Materials Science: Materials in Electronics* 31.24 (2020), pp. 22375–22384. ISSN: 0957-4522. DOI: 10.1007/s10854-020-04739-z.

[78] D. Chen et al. "Morphology control of hexagonal strontium ferrite micro/nano-crystals." In: *AIP Advances* 7.5 (2017). DOI: 10.1063/1.4974283.

[79] R. C. Pullar. "Hexagonal ferrites: A review of the synthesis, properties and applications of hexaferrite ceramics." In: *Progress in Materials Science* 57.7 (2012), pp. 1191–1334. ISSN: 0079-6425. DOI: 10.1016/j.pmatsci.2012.04.001.

[80] G. A. Alna'washi et al. "Magnetic Study of M-type Co-Ti Doped Strontium Hexaferrite Nanocrystalline Particles." In: *Journal of Superconductivity and Novel Magnetism* 33.5 (2020), pp. 1423–1432. ISSN: 1557-1939. DOI: 10.1007/s10948-019-05334-y.

[81] R. A. McCurrie. "Chapter 3 The structure and properties of alnico permanent magnet alloys." In: *Handbook of Ferromagnetic Materials*. Ed. by E. P. Wohlfarth. Vol. 3. Handbook of Ferromagnetic Materials. Elsevier, 1982, pp. 107–188. ISBN: 9780444863782. DOI: 10.1016/S1574-9304(05)80089-6.

[82] L. Zhou et al. "Architecture and magnetism of alnico." In: *Acta Materialia* 74 (2014), pp. 224–233. ISSN: 13596454. DOI: 10.1016/j.actamat.2014.04.044.

[83] K. J. de Vos. "The relationship between microstructure and magnetic properties of alnico alloys." PhD thesis. 1966. DOI: 10.6100/IR287613.

[84] S. U. Rehman et al. "Microstructures and magnetic properties of cast alnico 8 permanent magnets under various heat treatment conditions." In: *Physica B: Condensed Matter* 552 (2019), pp. 136–141. ISSN: 09214526. DOI: 10.1016/j.physb.2018.10.007.

[85] Magnetic Materials Producers Association. *MMPA No. 0100-00, Standard Specifications for Permanent Magnet Materials.* Illinois, 2000.

[86] K. Edalati et al. "Nanomaterials by severe plastic deformation: review of historical developments and recent advances." In: *Materials Research Letters* 10.4 (2022), pp. 163–256. DOI: 10.1080/21663831.2022.2029779.

[87] V. N. Varyukhin et al. "Twist Extrusion: Fundamentals and Applications." In: *Materials Science Forum* 667-669 (2010), pp. 31–37. DOI: 10.4028/www.scientific.net/MSF.667-669.31.

[88]   M. Borodachenkova, W. Wen, and A. M. de Bastos Pereira. "High-Pressure Torsion: Experiments and Modeling." In: *Severe Plastic Deformation Techniques*. Ed. by M. Cabibbo. InTech, 2017. ISBN: 978-953-51-3425-1. DOI: 10.5772/intechopen.69173.

[89]   A. Hohenwarter et al. "Technical parameters affecting grain refinement by high pressure torsion." In: *International Journal of Materials Research* 100.12 (2009), pp. 1653–1661. ISSN: 1862-5282. DOI: 10.3139/146.110224.

[90]   B. A. Greenberg et al. "Microstructural Evolution in Ceramics and Glasses during High Pressure Torsion." In: *Russian Metallurgy (Metally)* 2018.10 (2018), pp. 935–940. ISSN: 0036-0295. DOI: 10.1134/S0036029518100087.

[91]   M. Shahzamanian et al. "Numerical Study about the Influence of Superimposed Hydrostatic Pressure on Shear Damage Mechanism in Sheet Metals." In: *Metals* 11.8 (2021), p. 1193. DOI: 10.3390/met11081193.

[92]   R. Pippan and A. Hohenwarter. "High pressure torsion (HPT): Chapter 4." In: *Severe plastic deformation technology*. Ed. by A. Rosochowski. Dunbeath, Scotland: Whittles Publishing, 2017, pp. 135–164. ISBN: 9781849950916.

[93]   V. A. Beloshenko et al. "Severe Plastic Deformation of Polymers." In: *Materials Transactions* 60.7 (2019), pp. 1192–1202. ISSN: 1345-9678. DOI: 10.2320/matertrans.MF201912.

[94]   A. Bachmaier and R. Pippan. "Generation of metallic nanocomposites by severe plastic deformation." In: *International Materials Reviews* 58.1 (2013), pp. 41–62. ISSN: 0950-6608. DOI: 10.1179/1743280412Y.0000000003.

[95]   Y. Qi et al. "Plastic flow and microstructural instabilities during high-pressure torsion of Cu/ZnO composites." In: *Materials characterization* 145 (2018), pp. 389–401. ISSN: 1044-5803. DOI: 10.1016/j.matchar.2018.09.001.

[96]   Y. Bai, G. Wagner, and Ch. B. Williams. "Effect of Particle Size Distribution on Powder Packing and Sintering in Binder Jetting Additive Manufacturing of Metals." In: *Journal of Manufacturing Science and Engineering* 139.8 (2017). ISSN: 1087-1357. DOI: 10.1115/1.4036640.

[97]   N. A. Mara et al. "Interface-Driven Plasticity in Metal–Ceramic Nanolayered Composites: Direct Validation of Multiscale Deformation Modeling via In Situ Indentation in TEM." In: *JOM* 68.1 (2016), pp. 143–150. ISSN: 1047-4838. DOI: 10.1007/s11837-015-1542-1.

[98]   S. Chen et al. "The effect of polytetrafluoroethylene particle size on the properties of biodegradable poly(butylene succinate)-based composites." In: *Scientific Reports* 11.1 (2021), p. 6802. ISSN: 2045-2322. DOI: 10.1038/s41598-021-86307-x.

[99]   P. M. Pohl et al. "Quantifying Co-Deformation Effects in Metallic Laminates by Loading–Unloading–Reloading Tensile Tests." In: *Metals* 13.6 (2023), p. 1049. DOI: 10.3390/met13061049.

[100]   A. Vorhauer and R. Pippan. "On the Onset of a Steady State in Body-Centered Cubic Iron during Severe Plastic Deformation at Low Homologous Temperatures." In: *Metallurgical and Materials Transactions A* 39.2 (2008), pp. 417–429. ISSN: 1073-5623. DOI: 10.1007/s11661-007-9413-1.

[101] A. Bachmaier et al. "On the process of co-deformation and phase dissolution in a hard-soft immiscible Cu Co alloy system during high-pressure torsion deformation." In: *Acta Materialia* 115 (2016), pp. 333–346. ISSN: 13596454. DOI: 10.1016/j.actamat.2016.06.010.

[102] E. S. Clark. "Unit Cell Information on Some Important Polymers." In: *Physical properties of polymers handbook*. Ed. by J. E. Mark. New York, NY: Springer Science+Business Media LLC, 2007, pp. 619–624. ISBN: 978-0-387-31235-4. DOI: 10.1007/978-0-387-69002-5_38.

[103] C. de Rosa et al. "Crystal structure of the trigonal form of isotactic polypropylene as an example of density-driven polymer structure." In: *Journal of the American Chemical Society* 128.1 (2006), pp. 80–81. ISSN: 0002-7863. DOI: 10.1021/ja0572957.

[104] A. V. Fratini et al. "Refinement of the structure of PEEK fibre in an orthorhombic unit cell." In: *Polymer* 27.6 (1986), pp. 861–865. ISSN: 00323861. DOI: 10.1016/0032-3861(86)90295-8.

[105] Md. L. Rahman et al. "Investigation of structural, morphological and magnetic properties of nanostructured strontium hexaferrite through co-precipitation technique: Impacts of annealing temperature and Fe/Sr ratio." In: *Heliyon* 9.3 (2023), e14532. ISSN: 2405-8440. DOI: 10.1016/j.heliyon.2023.e14532.

[106] S. Szymura. "The effect of manganese on the modification of non-metallic inclusions and magnetic properties of columnar alnico 5 permanent magnets." In: *Journal of Magnetism and Magnetic Materials* 30.3 (1983), pp. 389–394. ISSN: 03048853. DOI: 10.1016/0304-8853(83)90081-1.

[107] S. M. Hao, K. Ishida, and T. Nishizawa. "Role of alloying elements in phase decomposition in alnico magnet alloys." In: *Metallurgical and Materials Transactions A* 16.2 (1985), pp. 179–185. ISSN: 1073-5623. DOI: 10.1007/BF02816044.

[108] Zhi-Ying Zhang et al. "Deformation mechanism of highly textured Alnico magnets." In: *Journal of Alloys and Compounds* 945 (2023), p. 169334. ISSN: 09258388. DOI: 10.1016/j.jallcom.2023.169334.

[109] T. M. Liu, T. D. Juska, and I. R. Harrison. "Plastic deformation of polypropylene." In: *Polymer* 27.2 (1986), pp. 247–249. ISSN: 00323861. DOI: 10.1016/0032-3861(86)90333-2.

[110] E. Farotti et al. "Effect of temperature and strain rate on the formation of shear bands in polymers under quasi-static and dynamic compressive loadings: Proposed constitutive model and numerical validation." In: *Polymer* 245 (2022), p. 124690. ISSN: 00323861. DOI: 10.1016/j.polymer.2022.124690.

[111] J. C. Habumugisha et al. "Stretch-induced structural evolution of pre-oriented isotactic polypropylene films: An in-situ synchrotron radiation SAXS/WAXS study." In: *Polymer* 214 (2021), p. 123234. ISSN: 00323861. DOI: 10.1016/j.polymer.2020.123234.

[112] D. Grommes et al. "Investigation of Crystallization and Relaxation Effects in Coarse-Grained Polyethylene Systems after Uniaxial Stretching." In: *Polymers* 13.24 (2021). DOI: 10.3390/polym13244466.

[113] X. Chen et al. "Deformation mechanism of iPP under uniaxial stretching over a wide temperature range: An in-situ synchrotron radiation SAXS/WAXS study." In: *Polymer* 118 (2017), pp. 12–21. ISSN: 00323861. DOI: 10.1016/j.polymer.2017.04.054.

[114] J. Eichelter et al. "Influence of the α-relaxation on the high-velocity stretchability of isotactic polypropylene." In: *Polymer* 200 (2020), p. 122593. ISSN: 00323861. DOI: 10.1016/j.polymer.2020.122593.

[115] J. Yuan, A. Hiltner, and E. Baer. "The mechanical properties of PVC under high pressure." In: *Journal of materials science* 18.10 (1983), pp. 3063–3071. ISSN: 0022-2461. DOI: 10.1007/BF00700789.

[116] C. Buckley. "Glass-rubber constitutive model for amorphous polymers near the glass transition." In: *Polymer* 36.17 (1995), pp. 3301–3312. ISSN: 00323861. DOI: 10.1016/0032-3861(95)99429-X.

[117] D. M. Gezovich and P. H. Geil. "Deformation of polyoxymethylene by rolling." In: *Journal of materials science* 6.6 (1971), pp. 509–530. ISSN: 0022-2461. DOI: 10.1007/BF00550306.

[118] Y. Filanova et al. "Inelastic Behavior of Polyoxymethylene for Wide Strain Rate and Temperature Ranges: Constitutive Modeling and Identification." In: *Materials* 14.13 (2021). DOI: 10.3390/ma14133667.

[119] D. Garcia-Gonzalez et al. "Thermo-mechanics of Polymers at Extreme and Failure Conditions: Influence of Strain Rate and Temperature." In: *Handbook of Damage Mechanics*. Ed. by G. Z. Voyiadjis. Cham: Springer International Publishing and Imprint Springer, 2022, pp. 249–276. ISBN: 978-3-030-60241-3. DOI: 10.1007/978-3-030-60242-0_67.

[120] M. Lei et al. "Thermomechanical behaviors of polyether ether ketone (PEEK) with stretch-induced anisotropy." In: *Journal of the Mechanics and Physics of Solids* 148 (2021), p. 104271. ISSN: 0022-5096. DOI: 10.1016/j.jmps.2020.104271.

[121] D. Barba, A. Arias, and D. Garcia-Gonzalez. "Temperature and strain rate dependences on hardening and softening behaviours in semi-crystalline polymers: Application to PEEK." In: *International Journal of Solids and Structures* 182-183 (2020), pp. 205–217. ISSN: 0020-7683. DOI: 10.1016/j.ijsolstr.2019.08.021.

[122] S. Hamdan and G. M. Swallowe. "Crystallinity in PEEK and PEK after mechanical testing and its dependence on strain rate and temperature." In: *Journal of Polymer Science Part B: Polymer Physics* 34.4 (1996), pp. 699–705. ISSN: 0887-6266. DOI: 10.1002/(SICI)1099-0488(199603)34:4<699::AID-POLB10>3.0.CO;2-C.

[123] F. Chen et al. "A constitutive model of polyether-ether-ketone (PEEK)." In: *Journal of the mechanical behavior of biomedical materials* 53 (2016), pp. 427–433. DOI: 10.1016/j.jmbbm.2015.08.037.

[124] A. Pawlak, A. Galeski, and A. Rozanski. "Cavitation during deformation of semicrystalline polymers." In: *Progress in Polymer Science* 39.5 (2014), pp. 921–958. ISSN: 00796700. DOI: 10.1016/j.progpolymsci.2013.10.007.

[125] S. Fischer and N. Brown. "Deformation of polytetrafluoroethylene from 78 to 298 °K and the effects of environmental crazing." In: *Journal of Applied Physics* 44.10 (1973), pp. 4322–4327. ISSN: 0021-8979. DOI: 10.1063/1.1661959.

[126] K. Sato et al. "Deformation capability of poly(tetrafluoroethylene) materials: Estimation with X-ray diffraction measurements." In: *Polymer Testing* 113 (2022), p. 107690. ISSN: 01429418. DOI: 10.1016/j.polymertesting.2022.107690.

[127] J. A. Sauer, D. R. Mears, and K. D. Pae. "Effects of hydrostatic pressure on the mechanical behaviour of polytetrafluoroethylene and polycarbonate." In: *European Polymer Journal* 6.7 (1970), pp. 1015–1032. ISSN: 0014-3057. DOI: 10.1016/0014-3057(70)90034-0.

[128] L. A. Davis and C. A. Pampillo. "Kinetics of deformation of PTFE at high pressure." In: *Journal of Applied Physics* 43.11 (1972), pp. 4285–4293. ISSN: 0021-8979. DOI: 10.1063/1.1660918.

[129] C. L. Wang et al. "Effects of deformation on the microstructure of PTFE polymer studied by positron annihilation." In: *Journal of Physics: Condensed Matter* 5.40 (1993), pp. 7515–7520. ISSN: 0953-8984. DOI: 10.1088/0953-8984/5/40/025.

[130] A. Rozanski and A. Galeski. "Plastic yielding of semicrystalline polymers affected by amorphous phase." In: *International Journal of Plasticity* 41 (2013), pp. 14–29. ISSN: 07496419. DOI: 10.1016/j.ijplas.2012.07.008.

[131] R. van Tijum, W. P. Vellinga, and J. Th. M. de Hosson. "Adhesion along metal-polymer interfaces during plastic deformation." In: *Journal of materials science* 42.10 (2007), pp. 3529–3536. ISSN: 0022-2461. DOI: 10.1007/s10853-006-1374-z.

[132] F. Hirsch, E. Natkowski, and M. Kästner. "Modeling and simulation of interface failure in metal-composite hybrids." In: *Composites Science and Technology* 214 (2021), p. 108965. ISSN: 02663538. DOI: 10.1016/j.compscitech.2021.108965.

[133] A. Carradò et al. "Metal/polymer/metal hybrid systems: Towards potential formability applications." In: *Composite Structures* 93.2 (2011), pp. 715–721. ISSN: 02638223. DOI: 10.1016/j.compstruct.2010.07.016.

[134] I. Kuehnert et al. "Prefinished Metal Polymer Hybrid Parts." In: *Technologies for Lightweight Structures (TLS)* 1.2 (2018). DOI: 10.21935/tls.v1i2.86.

[135] A. A. Kündig et al. "Metallic glass/polymer composites by co-processing at similar viscosities." In: *Scripta Materialia* 56.4 (2007), pp. 289–292. ISSN: 13596462. DOI: 10.1016/j.scriptamat.2006.10.019.

[136] C. Granados-Miralles and P. Jenuš. "On the potential of hard ferrite ceramics for permanent magnet technology–a review on sintering strategies." In: *Journal of Physics D: Applied Physics* 54.30 (2021), p. 303001. ISSN: 0022-3727. DOI: 10.1088/1361-6463/abfad4.

[137] Zhi-Rui Wang et al. "A Review of Ultrafine-Grained Magnetic Materials Prepared by Using High-Pressure Torsion Method." In: *Materials (Basel, Switzerland)* 15.6 (2022). ISSN: 1996-1944. DOI: 10.3390/ma15062129.

[138] N. Kumar et al. "Impact of Particle Size on Room Temperature Ferrimagnetism of SrFe12O19." In: *Journal of Superconductivity and Novel Magnetism* 23.4 (2010), pp. 423–427. ISSN: 1557-1939. DOI: 10.1007/s10948-010-0766-0.

[139] R. Kumar and M. Kar. "Correlation between lattice strain and magnetic behavior in non-magnetic Ca substituted nano-crystalline cobalt ferrite." In: *Ceramics International* 42.6 (2016), pp. 6640–6647. ISSN: 0272-8842. DOI: 10.1016/j.ceramint.2016.01.007.

[140] M. K. Manglam et al. "Lattice strain caused magnetism and magnetocrystalline anisotropy in Zn modified barium hexaferrite." In: *Physica B: Condensed Matter* 588 (2020), p. 412200. ISSN: 09214526. DOI: 10.1016/j.physb.2020.412200.

[141] A. Atkinson. "Diffusion in Ceramics." In: *Materials science and technology*. Ed. by R. W. Cahn. Weinheim: Wiley-VCH, 2005. ISBN: 9783527313952. DOI: 10.1002/9783527603978.mst0122.

[142] V.M Zhukovsky et al. "Diffusion transport in hexagonal ferrites with magnetoplumbite structure." In: *Solid State Ionics* 119.1-4 (1999), pp. 15–17. ISSN: 0167-2738. DOI: 10.1016/S0167-2738(98)00476-7.

[143] A. Benediktovich. *Theoretical Concepts of X-Ray Nanoscale Analysis: Theory and Applications*. 1st edition. Vol. v.183. Springer Series in Materials Science Ser. Berlin, Heidelberg: Springer Berlin / Heidelberg, 2014. ISBN: 978-3-642-38176-8. DOI: 10.1007/978-3-642-38177-5.

[144] Y. Waseda, E. Matsubara, and K. Shinoda. *X-ray diffraction crystallography: Introduction, examples and solved problems*. Material Science Chemistry. Berlin and Heidelberg: Springer, 2011. ISBN: 978-3-642-16634-1. DOI: 10.1007/978-3-642-16635-8.

[145] C. L. Kolbe and D. L. Martin. "Hot Working of Alnico 5 Alloys." In: *Journal of Applied Physics* 31.5 (1960), S84–S85. ISSN: 0021-8979. DOI: 10.1063/1.1984614.

[146] T. Imoto and H. Hosokawa. "Effects of pressure to adhesion." In: *Kolloid-Zeitschrift & Zeitschrift für Polymere* 208.2 (1966), pp. 153–156. ISSN: 0303-402X. DOI: 10.1007/BF01500983.

[147] M. Didi and P. Mitschang. "Induction Welding of Metal/Composite Hybrid Structures." In: *Joining of Polymer-Metal Hybrid Structures*. Ed. by S. Amancio and L. A. Blaga. Hoboken: John Wiley & Sons, Ltd, 2018, pp. 101–125. ISBN: 9781118177631. DOI: 10.1002/9781119429807.ch4.

[148] J. Bridgwater. "Fundamental powder mixing mechanisms." In: *Powder Technology* 15.2 (1976), pp. 215–236. ISSN: 0032-5910. DOI: 10.1016/0032-5910(76)80051-4.

[149] M. J. Starink, X. Cheng, and S. Yang. "Hardening of pure metals by high-pressure torsion: A physically based model employing volume-averaged defect evolutions." In: *Acta Materialia* 61.1 (2013), pp. 183–192. ISSN: 13596454. DOI: 10.1016/j.actamat.2012.09.048.

[150] M. F. Ashby and D. R. H. Jones. *Engineering materials*. 4. ed. Oxford: Butterworth-Heinemann, 2012. ISBN: 9780080966656. DOI: 10.1016/C2009-0-64288-4.

[151] D. Tabor. *The Hardness of metals*. (Monographs on the physics and chemistry of materials). Oxford: Clarendon Pr, 1951.

[152] P. Zhang, S. X. Li, and Z. F. Zhang. "General relationship between strength and hardness." In: *Materials Science and Engineering: A* 529 (2011), pp. 62–73. ISSN: 09215093. DOI: 10.1016/j.msea.2011.08.061.

[153] S. G. Sandomirskii. "Estimation of the Ultimate Tensile Strength of Steel from Its HB and HV Hardness Numbers and Coercive Force." In: *Russian Metallurgy (Metally)* 2017.11 (2017), pp. 989–993. ISSN: 0036-0295. DOI: 10.1134/S003602951711012X.

[154] S. Tamimi, M. Ketabchi, and N. Parvin. "Microstructural evolution and mechanical properties of accumulative roll bonded interstitial free steel." In: *Materials & Design* 30.7 (2009), pp. 2556–2562. ISSN: 02641275. DOI: 10.1016/j.matdes.2008.09.039.

[155] C. de Julian Fernandez et al. "Topical Review: Progress and Prospects of Hard Hexaferrites for Permanent Magnet Applications." In: *Journal of Physics D: Applied Physics* (2020). ISSN: 0022-3727. DOI: 10.1088/1361-6463/abd272.

[156] A. D. Volodchenkov, Y. Kodera, and J. E. Garay. "Nanoscale integration of oxides and metals in bulk 3D composites: leveraging SrFe12O19/Co interfaces for magnetic exchange coupling." In: *Journal of materials science* 54.11 (2019), pp. 8276–8288. ISSN: 0022-2461. DOI: 10.1007/s10853-019-03323-z.

[157] D. Wang et al. "Cold sintering of microwave dielectric ceramics and devices." In: *Journal of Materials Research* 36.2 (2021), pp. 333–349. ISSN: 0884-2914. DOI: 10.1557/s43578-020-00029-w.

[158] J. Guo et al. "Recent Progress in Applications of the Cold Sintering Process for Ceramic–Polymer Composites." In: *Advanced Functional Materials* 28.39 (2018). ISSN: 1616-301X. DOI: 10.1002/adfm.201801724.

[159] Y. Li et al. "Cold sintering co-firing of (Ca,Bi)(Mo,V)O 4 –PTFE composites in a single step." In: *Journal of the American Ceramic Society* 105.10 (2022), pp. 6262–6270. ISSN: 0002-7820. DOI: 10.1111/jace.18595.

[160] G. Subodh et al. "PTFE/Sr2Ce2Ti5O16 polymer ceramic composites for electronic packaging applications." In: *Journal of the European Ceramic Society* 27.8-9 (2007), pp. 3039–3044. ISSN: 09552219. DOI: 10.1016/j.jeurceramsoc.2006.11.049.

[161] R. Fischer et al. "Grain-size dependence of remanence and coercive field of isotropic nanocrystalline composite permanent magnets." In: *Journal of Magnetism and Magnetic Materials* 153.1-2 (1996), pp. 35–49. ISSN: 03048853. DOI: 10.1016/0304-8853(95)00494-7.

[162] E. A. Périgo et al. "Past, present, and future of soft magnetic composites." In: *Applied Physics Reviews* 5.3 (2018), p. 031301. DOI: 10.1063/1.5027045.

[163] S. Lucarini, M. Hossain, and D. Garcia-Gonzalez. "Recent advances in hard-magnetic soft composites: Synthesis, characterisation, computational modelling, and applications." In: *Composite Structures* 279 (2022), p. 114800. ISSN: 02638223. DOI: 10.1016/j.compstruct.2021.114800.

[164] M. Ghidini et al. "Hard–soft composite magnets." In: *Journal of Magnetism and Magnetic Materials* 316.2 (2007), pp. 159–165. ISSN: 03048853. DOI: 10.1016/j.jmmm.2007.02.040.

[165] P. Jenuš et al. "Ferrite-Based Exchange-Coupled Hard–Soft Magnets Fabricated by Spark Plasma Sintering." In: *Journal of the American Ceramic Society* 99.6 (2016), pp. 1927–1934. ISSN: 0002-7820. DOI: 10.1111/jace.14193.

[166] P. Maltoni et al. "Tuning the Magnetic Properties of Hard–Soft SrFe 12 O 19 /CoFe 2 O 4 Nanostructures via Composition/Interphase Coupling." In: *The Journal of Physical Chemistry C* 125.10 (2021), pp. 5927–5936. ISSN: 1932-7447. DOI: 10.1021/acs.jpcc.1c00355.

[167] S. A. Sam et al. "Nanocomposite Permanent Magnets Based on SrFe12O19-Fe3O4 Hard-Soft Ferrites." In: *Journal of Superconductivity and Novel Magnetism* 34.12 (2021), pp. 3333–3344. ISSN: 1557-1939. DOI: 10.1007/s10948-021-06070-y.

[168] P. Maltoni et al. "Exploring the magnetic properties and magnetic coupling in SrFe12O19/Co1-xZnxFe2O4 nanocomposites." In: *Journal of Magnetism and Magnetic Materials* 535 (2021), p. 168095. ISSN: 03048853. DOI: 10.1016/j.jmmm.2021.168095.

[169] S. Erokhin and D. Berkov. "Optimization of Nanocomposite Materials for Permanent Magnets: Micromagnetic Simulations of the Effects of Intergrain Exchange and the Shapes of Hard Grains." In: *Physical Review Applied* 7.1 (2017). DOI: 10.1103/PhysRevApplied.7.014011.

[170] Y. L. Ma et al. "Preparation and magnetic properties of MnBi-based hard/soft composite magnets." In: *Journal of Applied Physics* 115.17 (2014). ISSN: 0021-8979. DOI: 10.1063/1.4868078.

[171] J. Kruzelak. "Magnetic Composites Based on Butadiene Rubber and Strontium Ferrites." In: *MOJ Polymer Science* 1.5 (2017). DOI: 10.15406/mojps.2017.01.00025.

[172] H. Naceur, A. Megriche, and M. El Maaoui. "Effect of sintering temperature on microstructure and electrical properties of Sr1−x(Na0.5Bi0.5) x Bi2Nb2O9 solid solutions." In: *Journal of Advanced Ceramics* 3.1 (2014), pp. 17–30. ISSN: 2226-4108. DOI: 10.1007/s40145-014-0089-x.

[173] V. P. Singh et al. "A Current Review on the Synthesis and Magnetic Properties of M-Type Hexaferrites Material." In: *World Journal of Condensed Matter Physics* 08.02 (2018), pp. 36–61. ISSN: 2160-6919. DOI: 10.4236/wjcmp.2018.82004.

[174] J. Du et al. "Two-step sintering of M-type strontium ferrite with high coercivity." In: *Ceramics International* 45.6 (2019), pp. 6978–6984. ISSN: 0272-8842. DOI: 10.1016/j.ceramint.2018.12.197.

[175] Kyoung-Seok Moon, E. S. Lim, and Y. M. Kang. "Effect of Ca and La substitution on the structure and magnetic properties of M-type Sr-hexaferrites." In: *Journal of Alloys and Compounds* 771 (2019), pp. 350–355. ISSN: 09258388. DOI: 10.1016/j.jallcom.2018.08.306.

[176] J. Lee et al. "Anisotropic characteristics and improved magnetic performance of Ca-La-Co-substituted strontium hexaferrite nanomagnets." In: *Scientific reports* 10.1 (2020), p. 15929. DOI: 10.1038/s41598-020-72608-0.

[177] C. G. Kontoyannis and N. V. Vagenas. "Calcium carbonate phase analysis using XRD and FT-Raman spectroscopy." In: *The Analyst* 125.2 (2000), pp. 251–255. ISSN: 00032654. DOI: 10.1039/a908609i.

[178] A. J. Bradley and A. Taylor. "An X-ray analysis of the nickel-aluminium system." In: *Proceedings of the Royal Society of London. Series A - Mathematical and Physical Sciences* 159.896 (1937), pp. 56–72. ISSN: 0080-4630. DOI: 10.1098/rspa.1937.0056.

[179] A. Díaz-Ortiz et al. "Structure and magnetism in bcc-based iron-cobalt alloys." In: *Physical Review B* 73.22 (2006). ISSN: 1098-0121. DOI: 10.1103/PhysRevB.73.224208.

[180]   K. H. J. Buschow and P. G. van Engen. "Magnetic and magneto-optical proper-
         ties of heusler alloys based on aluminium and gallium." In: *Journal of Magnetism
         and Magnetic Materials* 25.1 (1981), pp. 90–96. ISSN: 03048853. DOI: 10.1016/0304-
         8853(81)90151-7.

[181]   R. W. G. Wyckoff. *Crystal Structures: Vol. 1*. 2nd ed. New York: Interscience,
         1963.

[182]   J. T. Zhao et al. "Correlations of phase structure and thermal stability for Alnico
         8 alloys." In: *Journal of Magnetism and Magnetic Materials* 442 (2017), pp. 208–211.
         ISSN: 03048853. DOI: 10.1016/j.jmmm.2017.06.118.

[183]   S. U. Rehman et al. "Synthesis, microstructures, magnetic properties and ther-
         mal stabilities of isotropic alnico ribbons." In: *Journal of Magnetism and Magnetic
         Materials* 466 (2018), pp. 277–282. ISSN: 03048853. DOI: 10.1016/j.jmmm.2018.
         07.020.

[184]   K. Kimura et al. "Study of the bipyramidal site in magnetoplumbite-like com-
         pounds, SrM12O19 (M = Al, Fe, Ga)." In: *Journal of Solid State Chemistry* 87.1
         (1990), pp. 186–194. ISSN: 00224596. DOI: 10.1016/0022-4596(90)90081-8.

[185]   W. L. Bragg. "XLII. The crystalline structure of copper." In: *The London, Ed-
         inburgh, and Dublin Philosophical Magazine and Journal of Science* 28.165 (1914),
         pp. 355–360. ISSN: 1941-5982. DOI: 10.1080/14786440908635219.

[186]   A. Hooda et al. "Crystal structure refinement, dielectric and magnetic properties
         of Ca/Pb substituted SrFe 12 O 19 hexaferrites." In: *Journal of Magnetism and
         Magnetic Materials* 387 (2015), pp. 46–52. ISSN: 03048853. DOI: 10.1016/j.jmmm.
         2015.03.078.